

New Modeling of Compact, High-efficiency, and Widely-tunable Gas-phase Terahertz Lasers

by

Fan Wang

Submitted to the Department of Mechanical Engineering
in partial fulfillment of the requirements for the degree of

Doctor of Philosophy

at the

MASSACHUSETTS INSTITUTE OF TECHNOLOGY

September 2019

© Massachusetts Institute of Technology 2019. All rights reserved.

Author
Department of Mechanical Engineering
August 26, 2019

Certified by.....
Steven G. Johnson
Professor of Applied Mathematics and Physics
Thesis Supervisor

Certified by.....
Nicholas X. Fang
Professor of Mechanical Engineering
Thesis Supervisor

Accepted by
Nicolas Hadjiconstantinou
Chairman, Department Committee on Graduate Theses

New Modeling of Compact, High-efficiency, and Widely-tunable Gas-phase Terahertz Lasers

by

Fan Wang

Submitted to the Department of Mechanical Engineering
on August 26, 2019, in partial fulfillment of the
requirements for the degree of
Doctor of Philosophy

Abstract

The terahertz region, in the heart of the electromagnetic spectrum, has been the least utilized, in part due to inadequacies of available sources. Optically pumped far-infrared (OPFIR) lasers were one of the most powerful continuous-wave terahertz sources. However, such lasers have long been thought to have intrinsically low efficiency, not tunable in frequency, and large sizes. In this thesis, we introduce a compact, frequency-tunable source of terahertz radiation with high efficiency.

We first present both an innovative theoretical model and experimental validation of a Methyl Fluoride OPFIR laser at 0.25 THz that exhibits $10\times$ greater efficiency and $1,000\times$ smaller volume than the best commercial lasers. Unlike previous OPFIR-laser models involving only a few energy levels that failed even qualitatively to match experiments at high pressures, our *ab-initio* theory matches experiments quantitatively, within experimental uncertainties with no free parameters, by accurately capturing the interplay of millions of degrees of freedom in the laser.

Moreover, we demonstrate a widely frequency-tunable compact terahertz radiation with laughing gas (nitrous oxide N_2O) pumped by a quantum cascade laser (QCL). In experiments, broad tunability is achieved over 31 lines spanning 0.25–0.80 THz, each with kilohertz linewidths. Our comprehensive theoretical model is able to constrain the key molecular parameters and predict the optimal performance of the laser. The concept of QCL-pumped molecular laser (QPML) is a universal while revolutionary concept characterized by unprecedented frequency tunability over a wide range of rotational transitions using a single molecular gas as the gain medium. An analytical theory for QPML is presented to study the key factors for improving the laser performance. We believe that these developments will revive interest in optically pumped molecular laser as a powerful, tunable, and compact source of terahertz radiation.

Thesis Supervisor: Steven G. Johnson

Title: Professor of Applied Mathematics and Physics

Thesis Supervisor: Nicholas X. Fang
Title: Professor of Mechanical Engineering

To Zhitian and Ethan.

Acknowledgments

In the past six years, I owe Prof. Steven G. Johnson many debts of gratitude for all the mentorship, support, and encouragement he has given to me. From Steven, I have learnt plentiful knowledge in mathematics, physics, computer science, and even music theory. A mere “thank you” is far from enough to express my gratitude. I’m lucky to have Steven as my PhD supervisor, and working with him for all the post-graduate years is no doubt the most precious experience in my life.

My appreciation also goes to Prof. Henry O. Everitt from Duke University and the US Army Research Lab. We collaborated extensively on modeling the terahertz laser during the past 4 years. I learnt every bit of knowledge on the collisional physics and molecular transition from Henry, who has extraordinary physical intuition, great patience to a young novice, and enormous encouragement and optimism for all the time.

I would like to thank Prof. Nicholas X. Fang who serves as my co-advisor and thesis committee chair. Nick gives me many valuable advices and mentorship on thesis writing and how to present research ideas. In addition, I thank Prof George Barbastathis for providing helpful feedbacks on my thesis. I particularly want to thank Prof. John Joannopoulos for his inspiring discussion. I thank Prof J.C. Nave from McGill University for his kind help on numerical simulations on fluid dynamics.

My deep appreciation also goes to all members of the JDJ group for their productive discussions and friendship. In particular, I would like to thank Dr. Xiangdong Liang who is a great teacher on fluid dynamics and numerical algorithms, as well as a close friend, Dr. David Liu who was my officemate and taught me plenty of coding skills, Dr. Bo Zhen from whom I learnt a lot of physics, Dr. Ling Lu who inspired me on how to compute the laser output power during a random chat, and many many others. I would also like to express my gratitude to collaborators Dr. Paul Chevalier, Dr. Marco Piccardo, and Arman Amirzhan from Harvard University for their valuable discussion on the terahertz laser project. I appreciate the tremendous help on both conducting research and setting down the new life in Cambridge from Dr. Dafei

Jin, during my first year in Nick's group and the following years.

It is impossible to finish this thesis without the endless love and unconditioned support from my family throughout these years, especially my beloved wife Zhitian. This thesis is dedicated to her and our coming boy Ethan.

Contents

1	Introduction	23
1.1	Background	23
1.2	Failure of theory: vibrational bottleneck	26
1.3	Frequency tunability of OPFIR lasers	29
2	An <i>ab-initio</i> Modeling Framework for OPFIR Lasers	31
2.1	Review of molecular structure of CH ₃ F	33
2.1.1	Energy levels of CH ₃ F	33
2.2	Experimental measurements and artificial pressure bottlenecking . . .	37
2.3	Numerical modeling: Population inversion	39
2.3.1	Rate equations	40
2.3.2	Line shape function, IR pump absorption, and effective pump intensity	43
2.3.3	Molecule–wall collisions and boundary conditions	47
2.3.4	Numerical solver: fixed point iteration and Anderson acceleration	48
2.4	Numerical modeling: terahertz output power	53
2.5	Effective temperature model	55
2.5.1	Experiment-theory comparison	57
2.6	More theoretical results and discussion	61
2.7	Cavity optimization	67
3	Quantum Cascade Laser Pumped Molecular Lasers	69
3.1	Introduction	69

3.1.1	QCL-pumped molecular laser (QPML)	70
3.2	QCL-pumped N ₂ O laser	72
3.3	Theoretical modeling of N ₂ O QPML	77
3.3.1	Determination of σ_{DD} and other parameters	79
3.3.2	More predictions and discussion	81
3.4	Universal theory of QPML	85
3.5	Analytical derivation of QPML theory	89
3.5.1	Pump threshold	89
3.5.2	THz output power	90
4	Capillary Instability with Thermal Gradients	93
4.1	Introduction	93
4.2	Numerical modeling of capillary breakup with thermal gradient	96
4.3	Results and discussion	99
4.3.1	Example 1	99
4.3.2	Example 2	100
4.3.3	Capillary breakup with a thermal gradient	100
4.4	Summary	105
5	Concluding Remarks	107
A	Parameters of Methyl Fluoride	109
B	Average velocity of the population flux into the wall	111
C	Transmission through the output pinhole	113
D	Spontaneous emission time	115
E	Conservation of population	117
F	V-swap	119
G	Dipole matrix element	121

List of Figures

1-1	Average power vs (a) THz frequency, and (b) device volume of different terahertz sources. In (a), $Pf^2 = \text{constant}$ line is the typical power-frequency slope in a RF device, while the $P\lambda = \text{constant}$ line is the Manley–Rowe slope for gas-phase lasers. In (b), both commercial and our compact OPFIR lasers are shown. In this thesis, we will demonstrate an OPFIR laser that is $1000\times$ more compact while exhibits $10\times$ greater efficiency than the commercial OPFIR lasers.	24
2-1	Molecular structure of CH_3F	33
2-2	Schematics of (a) the laser cavity and (b) molecular energy levels of $^{13}\text{CH}_3\text{F}$. The energy levels consist of vibrational levels v_ℓ , with A and E symmetries, composed of rotational levels with quantum numbers J and K. The IR pump excites a transition between levels L and U, and lasing occurs for both the “direct” inversion between U and U–1 and the “refilling” inversion between L+1 and L.	36
2-3	IR absorption spectrum at 100 mTorr and 400 mTorr with various input pump powers. $\nu_0 = 31.0427$ THz is the frequency of the L–U transition, while the CO_2 pump laser is incident at a frequency $25 \text{ MHz} > \nu_0$	46
2-4	Convergence rate with (orange) and without (blue) Anderson acceleration. In this example, the gas pressure is 800 mTorr and the pump power is 5.0 Watt. The solver converges within 30 iterations without Anderson acceleration, while the same problem converges within 12 Anderson iterations.	52

2-5	Reproduction of the artificial high-pressure bottlenecking: Prediction of the THz output powers by a 6-level model, for various input pump powers (3.3W, 6.6W, and 10W), and for both the direct (solid lines) and refilling (dashed lines) transitions. It is clearly observed that no gain is obtained above 700 mTorr by the 6-level model, known as high-pressure unphysical bottlenecking.	57
2-6	(a) Experimental and (b) theoretical THz laser output power as a function of gas pressure, for various input pump powers (3.3W, 6.6W, and 10W), and for both the direct (solid lines) and refilling (dashed lines) transitions. Excellent agreement is obtained even though the theoretical model has no adjustable parameters; in contrast to previous work, our theory captures the fact that higher powers allow operation at higher pressures, in part because of a novel technique to model a large number of high-energy vibrational levels. The dotted parts of the direct lasing curves represent an inefficient regime in which the pump intensity is nearly zero in the back of the cavity. In this case our model's approximation of an effective z -uniform pump strength is inaccurate, but it is not desirable to operate in this regime.	58
2-7	The effective temperature T_v (in Kelvin) of type-A vibrational thermal pools as a function of radial position and molecular pressure, for an input pump power of 10W, with (a) cavity geometry in experiments, and (b) optimal cavity length as discussed in Section 2.7.	60
2-8	Radial distribution of population inversion for direct transition at 100 mTorr, 200 mTorr, 400 mTorr, and 1 Torr, with 10W input pump power.	61
2-9	THz gain spectrum at 100 mTorr and 400 mTorr with the input pump power equal to 3W and 10W. The width of spectrum is proportional to the gas pressure due to pressure broadening.	62

2-10	Significance of different collisional terms: Comparison between the full model, the 6-level model, the full model without the V-swap collision, the SPT process, and the dipole–dipole collision. The comparison shows that the SPT, DD collisions, as well as the effective temperature model are the most important to obtain accurate results, while the V-swap process with small collisional cross section doesn’t affect the output power too much.	63
2-11	The input pump power at lasing threshold (blue) and the differential quantum efficiency (DQE) (yellow) normalized by the Manley–Rowe (MR) limit at threshold vs. pressure for both inversions. The refilling inversion is both higher power and higher efficiency, with a modeled DQE that can reach 64%.	64
2-12	Total quantum efficiency (QE = THz power out / IR power in) of commercial OPFIR lasers and our compact OPFIR laser, normalized by the Manley–Rowe (MR) limit on QE. Our experimentally demonstrated laser achieves a QE that is 29% of the MR limit (29% of 0.8%) which improves to 39% after cavity optimization. Both are 10× better than the best commercial laser at the same frequency (0.25THz, or 1.2mm wavelength), while being 1000× smaller—in fact, we show theoretically that this efficiency boost is mainly due to the fact that our cavity is so much smaller.	66
2-13	Theoretical predictions of (a) the roughly optimal cavity length for various radii and (b) the optimized laser power, both as a function of pressure for an input pump power of 10W. The cavity length is optimized to equal half the decay length of the pump beam. The output power (b) is shown for the optimal cavity length at each pressure and radius so that each data point is a separate cavity design. The peak efficiency is increased from 29% of Manley–Rowe in the experimental cavity to 39%, but more importantly this optimization allows efficient operation at a wider range of high pressures and hence in smaller cavities.	67

- 3-1 Universality of the QCL pumped terahertz gas laser: Diagram showing the different rotational levels of a molecule for both the ground and excited vibrational states. The red arrows show various R-branch transitions between rotational levels J_L and J_U responsible for the rovibrational absorption spectrum of the molecule as an illustration. The population of each rotational level of the ground vibrational state determines the magnitude of the IR pump absorption. The blue arrows indicate that the gas can lase at frequencies corresponding to an inversion between two rotational states in the excited (“direct”) or ground (“refilling”) vibrational level. The frequency of the laser emission is approximately $\nu = 2BJ_U$ for the R-branch transitions. 71
- 3-2 Experimental setup: light from a tunable QCL is tuned to pump a vibrational transition and create a rotational population inversion, thus realizing a QCL pumped molecular laser (QPML). Light from the QCL is deflected by a 90%–10% beam splitter (BS) and transmitted through a gas cell so that the QCL may be tuned into coincidence with the vibrational transition by minimizing the transmitted intensity measured using a photodiode (PD). Light is coupled into the laser cavity through a hole in an off-axis parabolic mirror (OAP), through a ZnSe window at Brewster’s angle, and through a pinhole coupler in the cavity. A vacuum pump, pressure sensor, and gas reservoir are used to set the pressure in both the laser cavity and the gas cell. The radiation emitted from the pinhole of the QPML is collected with the OAP, sent through a Teflon lens, and measured by a power meter, detector, or receiver, the latter of which uses a frequency-multiplied local oscillator (LO) mixed with the signal to produce the intermediate frequency (IF) measured by a spectrum analyzer. The pump power from the QCL is varied using a wire grid polarizer on a calcium fluoride substrate. The laser cavity is tuned into resonance with the lasing frequency by moving a copper mirror on a translation stage. 73

3-3	Tunability of the optically pumped N ₂ O laser: Emission spectra of the laser were measured as the QCL pump laser was tuned to different infrared transitions of N ₂ O. The top x-axis shows the measured emission frequency while the bottom x-axis shows the quantum number of the lower state of the pumped R-branch transition. The QCL power was maximal (up to 250 mW coupled in the cavity), and the pressure was 40 mTorr for direct transitions and 20 mTorr for refilling transitions. A: Measured spectra of direct transitions with J_L from 11 to 30. B: Measured spectra of refilling transitions with J_L from 11 to 17.	75
3-4	Experimental measurements: A: The output power of the N ₂ O QPML is plotted as a function of the IR pump power from the QCL, for which $P_{\text{THz}} = 70$ mW and $\eta = 0.05$ mW/W at 40 mTorr for the $J_U = 15 \rightarrow 14$ transition at 374 GHz. B: Emission spectra recorded for various mirror positions (broad grey feature) indicate the full tuning range of the QPML operating at this same transition. The central line is plotted (blue line) and shows a recovered linewidth of ≤ 5 kHz at 374 GHz.	76
3-5	(A) Predicted and (B) measured QPML laser power as a function of gas pressure and QCL pump power for the same direct transition with $J_L = 14$	76
3-6	Threshold power for direct lasing as a function of pressure for both experimental measurements (blue circles) and theoretical modeling (dashed lines) with different values of $\sigma_{\text{DD}} = 25^2, 35^2, 45^2$. $J_L = 14$ is pumped rotational level. In the model, cavity loss is 0.3m^{-1} . The results indicate the dipole-dipole cross section of N ₂ O is 35^2	80
3-7	Contour plot of the THz output power from direct lasing transition as a function of pressure and pump power for $J_L = 31$. The theoretical prediction (left) matches the experimental measurement (right) very well with previously obtained dipole-dipole collisional cross section $\sigma_{\text{DD}} = 35 \text{ \AA}^2$, and QCL linewidth as 2 MHz. The cavity loss is fitted as 0.46 m^{-1}	81

3-8	THz output power vs pressure with $J_L = 6$ to $J_L = 41$ for both direct and refilling lasing.	82
3-9	THz output power vs pressure with $J_L = 6$ to $J_L = 41$ for both direct and refilling lasing.	83
3-10	Pump threshold power as a function of pressure for $J = 10, 20, 30, 40$. The cavity loss is assumed to be 0.3m^{-1} for all cases.	84
3-11	Plot showing the QPML tuning range and estimated power from direct transitions for 10 mTorr of various molecular gases in a compact cylindrical cavity pumped by a 250 mW QCL: Carbonyl sulfide (OCS), Nitrous oxide (N_2O), Methyl fluoride (CH_3F), Hydrogen cyanide (HCN), and Carbon monoxide (CO). The arrows indicate the J_L for which the rotational population is largest, illustrating how the Manley–Rowe effect skews the peak power to higher frequency. Also listed is the QCL tuning range required to pump the associated R-branch transitions.	86
3-12	Schematics of a simplified three-level model for analytical derivations.	89
4-1	Experimental setup of the fiber-drawing process: A macroscopic preform is thermally drawn into a fibre. Subsequent thermal processing of the fibre induces the capillary instability, resulting in the fiber core breakup and spherical particles.	94
4-2	(a) Break-up periods and (b) corresponding sphere diameters (squares) as a function of the feed speed for a 4 mm Si-core fibre shown together with the magnified graphs of standard deviation values (bars) as they appear within each one of the samples. The s.d. values in (a) are shown 10-fold magnified and 1,000-fold magnified in (b).	95
4-3	An example of level-set function: a signed distance function discretized on a Cartesian grid.	97

4-4	Numerical Stokes-flow simulations for a three-layer system with different surface tension values for the outer interface. Radius of inner and outer interfaces are 1.0 and 5.0, respectively. All three layers have viscosity equal to 0.91, 1.0, and 0.91. Surface tension of inner interface for both cases is 1.5, while the surface tension of the outer interface is 1.5 in (a) and 25.0 in (b).	99
4-5	Snapshots of Si/SiO ₂ fiber interface in experiment (left) and numerical simulations (right) with two different values of interfacial tension. 5.0 J/m ² gives results that match better with experimental observation quantitatively. (The experimental figure is provided by Prof. Fink group at MIT)	101
4-6	Breakup period predicted by both numerical simulation (dashed) and experimental measurements (diamond) as a function of feed speed. Temperature profiles of the flame varies linearly between 1400 °C to 1850 °C, with different transition width from 1.18mm to 2.0mm.	102
4-7	Schematics of the capillary breakup process with feed speed v_f	103
4-8	Breakup period predicted by both numerical simulation (dashed) and 1d analytical approximation (solid) as a function of feed speed. Temperature profiles of the flame varies linearly between 1400 °C to 1850 °C, with different transition width from 1.18mm to 2.0mm. Fitting parameter α is 0.45 for the fitting.	104
D-1	Numerical output power of both direct (solid lines) and refilling (dashed lines) lasing versus pressure with the input pump power equal to 10W, and with three different spontaneous emission lifetimes t_{sp} : 1sec, 10sec, and 100sec. t_{sp} has little effect on the peak output power far above threshold for both lasing transitions.	116
H-1	Discretization grid of pressure p , velocities in r direction u , and in z direction w	125

List of Tables

3.1	Predicted QPML power and QCL threshold pump power for the strongest IR ro-vibrational transition of eight candidate laser molecules. Assumes a 0.25W QCL pumping through a 1 mm diameter pinhole output coupler into a 5 mm diameter cylindrical laser cavity (loss = 0.06 m^{-1}) containing 10 mTorr of the molecular gas.	87
A.1	Parameters of Methyl Fluoride	109

Chapter 1

Introduction

1.1 Background

The problem of generating radiation in the terahertz (THz) or far-infrared range (0.3-3.0 THz) has challenged researchers for decades. Found in “the middle” of the electromagnetic spectrum, this region represents the high-frequency end of the radio/microwave region and the low-frequency end of the infrared (IR) region, which support widely used technologies such as radio, radar, night-vision cameras, high-bandwidth communications, and spectrometers. If these same technologies could operate in the terahertz region, many of them would benefit from appealing characteristics such as high bandwidth, high spatial resolution, compact size, and/or adjustable atmospheric propagation [1]. Among the many techniques developed to generate terahertz radiation as shown in Fig. 1-1, the most widely used [2] include harmonic multipliers of tunable microwave sources [3], vacuum electronics (backward-wave oscillators, gyrotrons, and carcinotrons)[4], supercontinua generated by ultrafast lasers and photoconductive switches [5], and difference-frequency mixing of tunable continuous-wave lasers [6, 7]. Commercial versions of each of these terahertz sources are available, but their cost and idiosyncrasies have prevented widespread adoption.

Often overlooked is an early method of terahertz generation, optically pumped far-infrared (OPFIR) gas lasers. These lasers were one of the most powerful sources to generate continuous-wave (CW) terahertz radiation [9–21]. They employ popu-

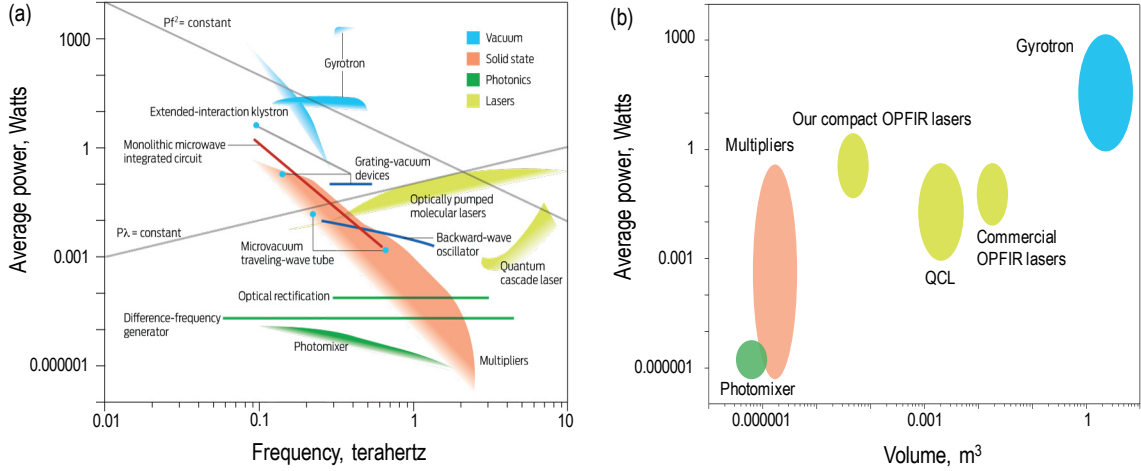


Figure 1-1: Average power vs (a) THz frequency [8], and (b) device volume of different terahertz sources. In (a), $Pf^2 = \text{constant}$ line is the typical power-frequency slope in a RF device, while the $P\lambda = \text{constant}$ line is the Manley–Rowe slope for gas-phase lasers. In (b), both commercial and our compact OPFIR lasers are shown. In this thesis, we will demonstrate an OPFIR laser that is $1000\times$ more compact while exhibits $10\times$ greater efficiency than the commercial OPFIR lasers.

lation inversions excited in molecule-specific rotational–vibrational transitions by a line-tunable CO_2 laser. By changing the gas, isotope, and CO_2 laser line, different transition frequencies could be made to lase, typically in meter-long cavities operated at low pressures (< 0.1 Torr). These lasers can generate significant power (e.g. > 150 mW near $\nu_{\text{THz}} = 2.5$ THz for the CH_3OH laser) and exhibit a narrow linewidth ($\Delta\nu \approx 1$ kHz); a combination of features that is not available with most other terahertz sources.

Initially, it was thought that low pressures and large cavities were required, but this produced a “vibrational bottleneck”: diffusion-limited relaxation by molecule–wall collisions that filled the vibrational level and quenched any inversion above a maximum pressure, regardless of the pump intensity [10, 13, 15]. It was subsequently discovered that OPFIR lasers could operate at pressures higher than this in smaller cavities, a result of collisional processes that excited high-energy vibrational levels and removed the bottleneck [16, 18]. This breakthrough was never fully investigated or exploited, however, as it came at a time when new sources of terahertz radiation were emerging [22–24]. Additionally, OPFIR lasers required an equally large CO_2

laser and high-voltage power supply. Moreover, they were poorly tunable, requiring the laser gas and CO₂ laser line to be changed each time a new frequency is needed. Consequently, OPFIR lasers fell from widespread use when these other sources became available.

This thesis addresses all the supposed design difficulties and previous theoretical misunderstandings mentioned above. We will first present an innovative theoretical model of OPFIR lasers that not only fully matches experiments, but also exhibits a superior laser regime with unprecedented conversion efficiencies and device compactness. We solve deficiencies of earlier models by developing a far more complete theory for a compact OPFIR laser, using the prototypical molecular gas ¹³CH₃F pumped by a line-tunable CO₂ laser. Using no adjustable parameters, our model matches our experimental measurements with excellent accuracy, especially considering its sensitivity to many experimental variables. Moreover, it shows that our compact OPFIR laser is 1000× smaller in volume while delivering more than 10× greater efficiency than the best commercial OPFIR lasers.

Furthermore, we bring up a revolutionary OPFIR laser concept characterized by enormous frequency-tunability over a wide range of rotational transitions using a single molecular gas as the gain medium. This concept is realized and demonstrated both theoretically and experimentally. Broad terahertz tunability is made possible by the use of a continuously tunable mid-infrared pump source, the quantum cascade laser (QCL) [25–27]. This single IR source may excite almost any ro-vibrational transition of almost any molecule, not just a rare coincidence afforded by a specific CO₂ laser line with a specific transition in a specific molecule. The combination of a compact QCL and a compact OPFIR laser can thereby produce a broadly tunable laser source that can easily fit in a shoebox.

1.2 Failure of theory: vibrational bottleneck

OPFIR lasers operate by creating rotational population inversion in the molecules, formed by the pump excitation. The infrared pump laser populates molecules from a rotational level L in the ground vibrational state to a rotational level U in excited state. From Boltzmann distribution, L is heavily populated while U is almost empty. When the pump is on, a series of collisions occur between rotational and vibrational levels, and between molecules and the cavity wall, creating two types of population inversion in steady state: “direct” inversion between U and $U-1$, and “refilling” inversion between $L+1$ and L .

In the diffusion-limited OPFIR lasers, the primary pathway for relaxation is molecule–wall collisions through diffusion. This makes the OPFIR laser operation sensitive to gas pressure. As pressure increases, the diffusion rate decreases while the collisional rate increases, causing pump saturation easily with population stuck in the excited state. Eventually, thermal vibrational population accumulated in the excited state overwhelms the nonthermal rotational population and quenches the lasing performance. This is known as “vibrational bottleneck”. The cutoff pressure can be derived as [28]

$$P_{\text{cutoff}} = \frac{7.1}{R} \sqrt{\frac{g_u}{g_{u-1}} \frac{T^{2.5}}{\nu \Delta\nu_p f_u \sigma_{\text{GK}} \sqrt{m}}} \quad (1.1)$$

where f_u is the population fraction of rotational level U , g_i is the degeneracy of level i , R is the cell radius in cm, T is the temperature in K, σ_{GK} is the gas kinetic collisional cross section in \AA^2 , $\Delta\nu_p$ is the pressure broadening half width in MHz/Torr, m is the mass of the molecule (AMU), and ν is the lasing frequency in GHz. For example, the cutoff pressure for $J = 5 \rightarrow 4, K = 3, \nu_3$ direct transition for $^{13}\text{CH}_3\text{F}$ OPFIR laser at room temperature is $110/R$ mTorr. For a cavity with radius 0.25cm, the cutoff pressure is 440 mTorr, regardless of the pump power.

However, it was subsequently discovered that OPFIR lasers could operate at pressures higher than this cutoff value in small cavities that removed the bottleneck [16]. It

turns out that the high-pressure bottleneck is only a theoretical artifact. The derivation in (1.1) included only two vibrational states associated with the pump process but excluded all the other high-lying vibrational states, which become heavily populated as the pressure increases and may significantly reduce the thermal population of the excited state U belongs to. It implies the OPFIR lasers can operate above the cutoff pressure with increasing pump power.

In order to include these vibrational levels, the critical innovation of this thesis is an effective vibrational temperature model that involves all accessible high-lying vibrational levels without having to describe the complicated relaxation processes among them explicitly. Although a related effective-temperature idea had been proposed previously [16], our model is the first to incorporate such an approach into a comprehensive *ab-initio* theory with no free parameters in which the effective temperature is determined self-consistently. Specifically, we make the ansatz that vibrational transitions are rapid enough to “thermalize” those high-lying levels with a Boltzmann distribution described by an effective temperature, so they may be grouped together into a separate population “pool”. The main justification of this ansatz is that thermalization among vibrational states is through bimolecular collisions, meaning the rates increase with pressure, while vibrational-state relaxation occurs through diffusion to the walls, which goes as the inverse of pressure. Therefore, the higher the pressure, the more vibrational thermalizing collisions occur before diffusion to the walls relaxes the excitation, and so the model becomes more accurate in the high-pressure regime where these extra vibrational levels are relevant to the inversion. More details are discussed in Section 2.5.

Moreover, we have developed a complete *ab-initio* theory that accurately captures the interplay of millions of degrees of freedom in the laser, including many collisional processes that people neglected or approximated, such as inhomogeneous broadening, dipole–dipole collisions, symmetry-preserving thermalization, V-swap processes, molecule–wall collisions, velocity subclasses, and spatial diffusion. An efficient numerical solver is developed to find the steady state directly, without time evolution, as a system of millions of coupled nonlinear rate equations. Not only does the model

match experiments; it also unexpectedly shows that our laser exhibits remarkable conversion efficiency, up to 39% of the Manley–Rowe limit which is $10\times$ greater than the best commercial OPFIR laser, while the cavity volume is $1,000\times$ smaller.

1.3 Frequency tunability of OPFIR lasers

Though we have realized a high-efficiency OPFIR laser with compact cavity size, the whole OPFIR laser system still requires a large-size CO₂ laser as the pump source. CO₂ pump laser also prevents the frequency tunability. It requires the molecular gas and pump laser line to be changed each time a new frequency is needed. Therefore, the huge size and lack of frequency tunability still limit OPFIR lasers from widespread use.

In this thesis, we will introduce a revolutionary OPFIR laser by replacing CO₂ laser with a continuously tunable mid-infrared pump source, the quantum cascade laser (QCL) [25–27]. A single QCL may excite almost any ro-vibrational transition of almost any molecule, which easily realizes the broad terahertz tunability.

We will use nitrous oxide (N₂O, laughing gas) as the gain medium to demonstrate broad frequency-tunability over 31 lines spanning 0.25–0.80 THz, each with kilohertz linewidths. The comprehensive OPFIR laser model equips us with the ability to study the QCL-pumped molecular laser extensively. We will show laser lines spanning more than 1 THz with powers greater than one milliwatt are possible from many molecular gases pumped by commercially-available QCLs.

Chapter 2

An *ab-initio* Modeling Framework for OPFIR Lasers¹

In this chapter, we'll present both an innovative theoretical model and an experimental validation of OPFIR lasers. In particular, we develop the *ab-initio* model based on the prototypical molecular gas Methyl Fluoride (CH_3F), which is widely used as gain medium in many OPFIR lasers [9]. An effective temperature model is developed to include high-lying vibrational levels to overcome the vibrational bottleneck at high pressures. Our theory matches experiments quantitatively, within experimental uncertainties with no free parameters, by accurately capturing the interplay of millions of degrees of freedom in the laser. It also shows that our compact laser with $1,000 \times$ smaller in volume exhibits more than $10 \times$ greater efficiency than the best commercial laser, pointing out a new high-efficiency regime for terahertz gas-phase lasers. We believe that these results will revive interest in OPFIR laser as a powerful and compact source of terahertz radiation.

Here, we will review the energy structure of the molecule CH_3F in Section 2.1, following which the experimental results are presented in Section 2.2. A series of nonlinear rate equations is developed in Section 2.3 to describe the pump transition

¹This chapter is based on: Fan Wang, Jeongwon Lee, Dane J. Phillips, Samuel G. Holliday, Song-Liang Chua, Jorge Bravo-Abad, John D. Joannopoulos, Marin Soljačić, Steven G. Johnson, and Henry O. Everitt. A high-efficiency regime for gas-phase terahertz lasers. *Proceedings of the National Academy of Sciences, USA*, 115(26):6614–6619, 2018.

and the complex nonlinear interactions between many vibrational and rotational levels, and between the molecules and the cavity wall. An efficient numerical solver by fixed point iteration with Anderson acceleration is developed to obtain the steady-state population for all rotational and vibrational levels. In section 2.4, we'll present how the THz output power is then self-consistently computed with the calculated population inversion. Section 2.5 describes in detail the implementation of effective temperature model (EVM) and shows that pressure bottleneck can be reproduced without EVM, while a full match with experiments is obtained with EVM. More theoretical results and discussions on the population inversion, gain coefficients, and laser efficiency are presented in Section 2.6, following which the optimization of the cavity geometry is shown in Section 2.7 to maximize the conversion efficiency and the THz output power.

2.1 Review of molecular structure of CH₃F

2.1.1 Energy levels of CH₃F

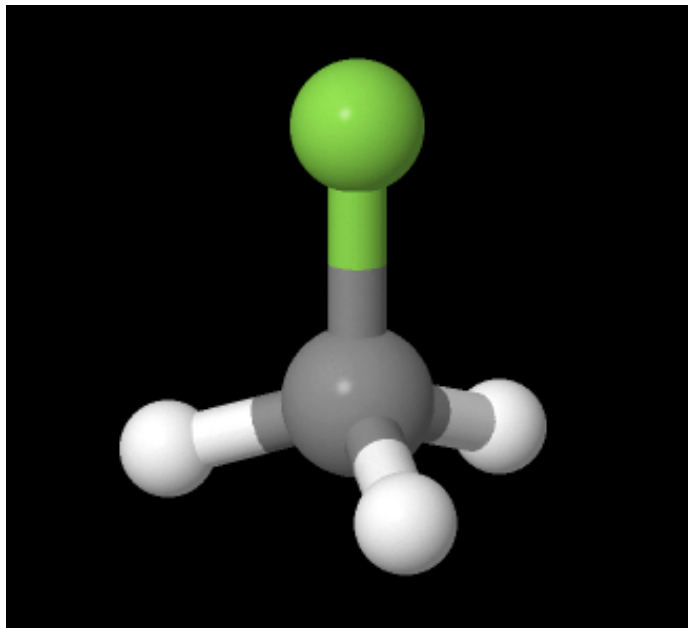


Figure 2-1: Molecular structure of CH₃F.

Vibrational energy levels of symmetric top molecules

A schematic diagram of CH₃F is shown in Fig. 2-1. In CH₃F, there are $N = 5$ atoms, so its total degrees of freedom are $3N - 6 = 9$. Three vibrational modes are doubly degenerate, therefore CH₃F has 6 distinct vibrational modes. Animations of all the vibrational modes can be found online (https://people.chem.ucsb.edu/laverman/leroy/GaucheSpace/CH3F_vib.html). The energy of vibrational mode k is

$$E_{k,n} = \left(n + \frac{1}{2} \right) \hbar\omega_k \quad (2.1)$$

where $\hbar\omega_k$ is the characteristic energy for mode k , and $n = 0, 1, \dots$ is the level of excitation. Then the vibrational energy difference between adjacent excitations of mode k is simply $\hbar\omega_k$. For methyl fluoride, $\hbar\omega_k$ of the six vibrational modes are listed in Appendix A. In particular, the excitation frequency of ν_3 mode for ¹³CH₃F

is 1027.49 cm^{-1} . Figure 2-2(b) shows the vibrational energy levels of $^{13}\text{CH}_3\text{F}$ up to 3000cm^{-1} .

Rotational energy levels

Each vibrational state is split into many rotational levels. CH_3F has three-fold rotational symmetry along the C–F bond and belongs to the symmetry group C_{3v} . It is also categorized as a prolate symmetric top molecule [29] in which two moments of inertia are equal and greater than the third, i.e., $I_x = I_y > I_z$. The Hamiltonian of CH_3F as a rigid rotor can be written as

$$H = \frac{\hat{P}^2}{2I_y} + \left(\frac{1}{2I_z} - \frac{1}{2I_y} \right) \hat{P}_z^2. \quad (2.2)$$

From quantum mechanics, the rotational energy levels are

$$E_r = \langle J, K, M | H | J, K, M \rangle = BJ(J+1) + (A-B)K^2, \quad (2.3)$$

in which $|J, K, M\rangle$ is the eigenstate. J is the angular momentum quantum number. K and M are the projections of J satisfying $-J \leq K, M \leq J$. States with $+K$ and $-K$ are degenerate, as are all values of M . So each rotational level can be labeled by $|J, K\rangle$ with $0 \leq K \leq J$. In (2.3),

$$A = \hbar^2/2I_z, \quad B = \hbar^2/2I_y \quad (2.4)$$

are the rotational constants. For CH_3F , $A \approx 150 \text{ GHz}$, and $B \approx 25 \text{ GHz}$ (the Planck constant h is neglected here for convenience.). The rotational transition energy of $|J+1, K\rangle \rightarrow |J, K\rangle$ is

$$E_{J+1 \rightarrow J} = 2B(J+1), \quad (2.5)$$

which is approximately $50(J+1) \text{ GHz}$ for CH_3F .

Note that (2.3) assumes body fixed symmetric top molecules. With centrifugal

stretching, a more accurate expression of the rotational energy levels is

$$E_r = BJ(J+1) + (A-B)K^2 - D_J J^2(J+1)^2 - D_{JK} J(J+1)K^2 - D_K K^4 \quad (2.6)$$

Values of all the rotational constants A, B, D_J, D_{JK} , and D_K for both $^{12}\text{CH}_3\text{F}$ and $^{13}\text{CH}_3\text{F}$ are listed in Appendix A. Schematics of the rotational energy levels of $^{13}\text{CH}_3\text{F}$ are shown in Fig. 2-2(b).

Due to the orientation of hydrogen nuclei spin, molecules of symmetric top molecules like CH_3F are categorized into two symmetry species, labeled by A and E. The categorization is related to K quantum number. Molecules with $K = 3n$ where n is an integer are categorized as A type, and molecules with $K \neq 3n$ are categorized as E type [28].

The degeneracy of state $|J, K\rangle$ is obtained by

$$g = g_M g_K g_I, \quad (2.7)$$

where g_M and g_K are the degeneracies of quantum number M and K , respectively. g_I describes the degeneracy of exchange of identical hydrogen nuclei spin. So

$$g_M = (2J+1), \quad g_K = \begin{cases} 1, & \text{if } K = 0 \\ 2, & \text{if } K > 0 \end{cases}, \quad g_I = \begin{cases} 2, & \text{if } K = 3n \\ 1, & \text{if } K \neq 3n \end{cases} \quad (2.8)$$

where n is nonnegative integers.

When the pump laser frequency matches the ro-vibrational transition frequency between rotational level J_L in the ground vibrational state and rotational level J_U in the excited vibrational state, it can create population inversion and produces a THz laser. For polar molecules with permanent dipole moments, the selection rule for allowed ro-vibrational transitions is $J_U = J_L + 1, J_L$, and $J_L - 1$, which are called R-, Q-, and P-branch transitions, respectively. In this thesis, we mainly focus on the R-branch transition.

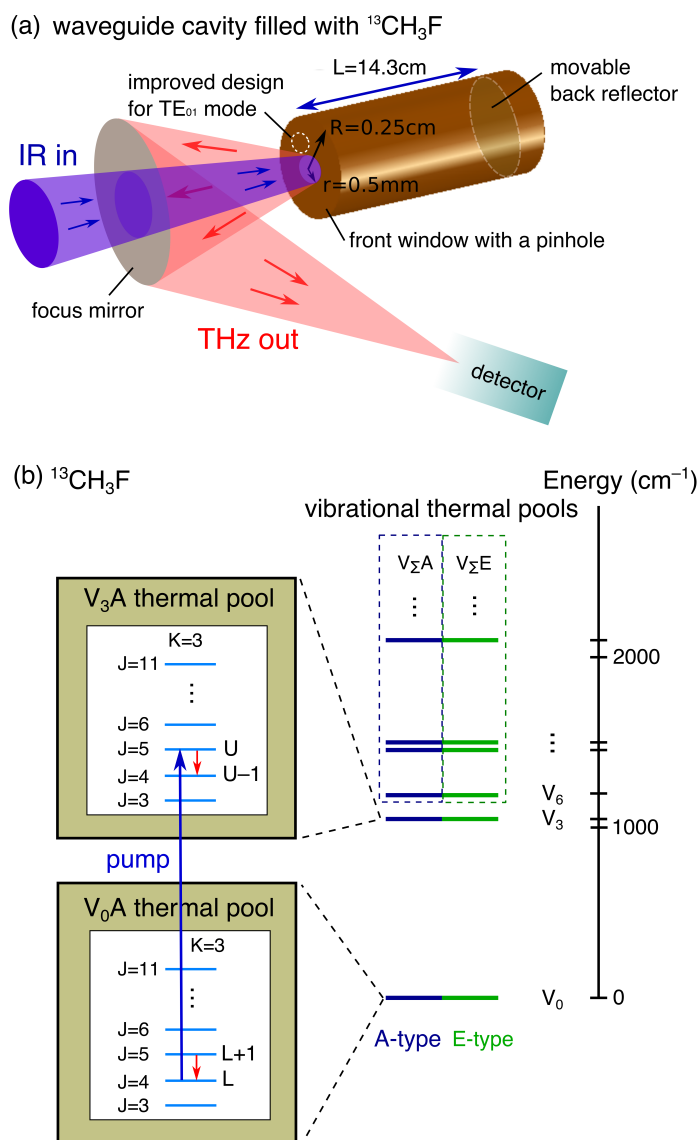


Figure 2-2: Schematics of (a) the laser cavity and (b) molecular energy levels of $^{13}\text{CH}_3\text{F}$. The energy levels consist of vibrational levels v_ℓ , with A and E symmetries [19], composed of rotational levels with quantum numbers J and K. The IR pump excites a transition between levels L and U, and lasing occurs for both the “direct” inversion between U and U-1 and the “refilling” inversion between L+1 and L.

2.2 Experimental measurements and artificial pressure bottlenecking

Fig. 2-2(a) depicts our OPFIR laser system: a line-tunable CO₂ pump laser ($\lambda = 9.7\mu\text{m}$) is focused through a pinhole in the front copper mirror into a $5\text{mm} \times 14.3\text{cm}$ copper tube filled with ¹³CH₃F gas. The lasing transition is brought into resonance with the cavity by a copper-plunger rear mirror that adjusts the cavity length, and the resulting laser power emerges from the same pinhole, after which it is detected by a heterodyne receiver.

In ¹³CH₃F, the coincidence between the 9P(32) line of the pump laser and the R₃(4) ro-vibrational transition in ¹³CH₃F produces two rotational population inversions, the “direct” $J = 5 \rightarrow 4$ (with $K = 3$, type A) inversion in v_3 with frequency 245.351 GHz and a corresponding “refilling” rotational transition in the type A ground vibrational level v_0 with frequency 248.559 GHz [30]. The heterodyne receiver distinguishes the lasing transitions and measures their intensity as a function of pressure and the input pump power.

In experiments, the pump beam from a grating-tuned Apollo CO₂ laser (Model 570), producing as much as 15W on the 9P(32) line at $9.657\mu\text{m}$, was focused through a 1mm diameter pinhole in a gold-coated copper plate by a 10cm focal length ZnSe lens into the 0.5cm diameter, 14.3cm long OPFIR laser cavity with a base pressure of $< 10^{-4}$ Torr and a transmitted laser power 2/3 of the incident power (e.g. 10W input pump power at maximum output). The cavity was composed of copper tubing with a gold-coated cylindrical copper plunger inserted into the rear of the cavity to adjust the cavity length while using a bellows to maintain a vacuum seal. In each measurement for a given pressure and pump power, the plunger was adjusted to tune the cavity resonance either to the direct or refilling transition, then the detuning of the CO₂ laser was adjusted with a piezoelectric transducer mounted on a pump cavity mirror to maximize the OPFIR laser output intensity. The 1.2mm wavelength laser radiation strongly diffracted from the 1mm diameter pinhole, so only a fraction was captured for detection through a series of copper pipes, copper mirrors, and

Teflon lenses. Attenuators with unknown absorbance were used to limit the power reaching the detector to ensure it remained in the linear-response regime. A Virginia Diodes heterodyne receiver operating in the 220–330GHz band was used to measure the frequency and strength of the OPFIR laser emission. The width of the measured emission lines was less than 3MHz, determined not by the laser but by the detection bandwidth of the spectrum analyzer used to display the intermediate frequency.

Figure 2-6(a) shows the measured output power as a function of gas pressure, for various input pump powers (3.3 W, 6.6 W, and 10 W) and for both the direct (solid lines) and refilling (dashed lines) transitions. In contrast with previous theoretical models that predicted a pump power-independent vibrational bottleneck, the experimental results show no vibrational bottleneck on either transition. In fact, increasing pump power produces higher-pressure operation, indicating even stronger emission and higher pressures are achievable. This confirms the failure of all previous theory with only a few vibrational levels that creates artificial high-pressure bottlenecks. In the following sections, a far more comprehensive theoretical model is developed to fully describe the high-pressure operation in the compact OPFIR lasers.

2.3 Numerical modeling: Population inversion

To understand the lack of vibrational bottlenecking, a thorough model of OPFIR laser operation must capture many different physical processes. Gas-phase molecules typically have hundreds to thousands of thermally populated rotational energy levels in the same vibrational modes as the pumped states (L→U).

It has previously been shown that rapid collisional thermalization maintains a Boltzmann distribution of population across most rotational states within a given vibrational level v_ℓ and symmetry type (A or E); consequently, they may be modeled as a **thermal pool** [18]. This thermal-pool approximation dramatically simplifies models of the collision physics by reducing the number of levels that must be individually included and collision cross-sections that must be known to those few most closely connected to L and U.

Nevertheless, after the pump excites molecules from L to U, a complicated set of collisional relaxation processes ensues, both bimolecular rotational energy transfer and molecular diffusion to the walls for ro-vibrational thermalization, so that population inversions between L+1 and L (refilling) and U and U−1 (direct) occur in a manner that depends sensitively on the input pump power, pressure, radial population distribution, cavity length, and cavity mode. All these collisional processes will be discussed term by term in the following section of rate equations. In particular, molecule–wall collisions are the primary pathway for vibrational relaxation in OPFIR lasers. Since the diffusion rate goes as $1/pR^2$ for pressure p and cell radius R , typical large-diameter glass OPFIR lasers require operation at low pressure, while small-diameter metallic cells are favored for high-pressure operation (with the tradeoff of increased ohmic losses at the lasing frequency).

The infrared pump creates non-thermal rotational populations N_ℓ^r and non-equilibrium populations of vibrational thermal pools N_p^v , and the goal is to predict these differences N from the equilibrium (unpumped) populations and their consequences for THz gain. Our semiclassical theoretical model consists of a set of rate equations giving $\dot{N} = \partial N/\partial t$ for both N_ℓ^r and N_p^v . Below, we begin by describing these rate

equations (which include various transitions, coupling to the pump, and an effective-temperature model discussed later for unknown vibrational levels), then explain how the $\dot{N} = 0$ steady state is found, and finally how the output power is extracted self-consistently from the populations.

2.3.1 Rate equations

The **rotational-level rate equations** for symmetry type A are given by:

$$\begin{aligned} \frac{dN_{\ell}^{\text{r}}(v, \mathbf{r}, t)}{dt} = & \sum_{\ell'} -\gamma_{\ell\ell'} N_{\ell}^{\text{r}}(v, \mathbf{r}, t) + \gamma_{\ell'\ell} N_{\ell'}^{\text{r}}(v, \mathbf{r}, t) \\ & - (\gamma_{\ell p}^{\text{SPT}} + \gamma_{\ell p}^{\text{VS}}) N_{\ell}^{\text{r}}(v, \mathbf{r}, t) \\ & + R_{\text{pump}}(v, \mathbf{r}, t) \\ & + D\nabla^2 N_{\ell}^{\text{r}}(v, \mathbf{r}, t). \end{aligned} \quad (2.9)$$

Here, population density of energy level ℓ $N_{\ell}^{\text{r}}(v, \mathbf{r}, t)$ depends on molecular axial (the direction of the pump beam) velocity v , position \mathbf{r} , time t . Because the problem is axisymmetric, we simplify \mathbf{r} to only the radial position r and eliminate the axial (z -) dependence by an averaging procedure described in Section 2.3.2.

The first two terms in equation (2.9) describe the dipole–dipole collisions. $^{13}\text{CH}_3\text{F}$ is a polar molecule with permanent dipole moment $\mu_0 = 1.86$ Debye. Dipole–dipole collision is one of the most dominant collisional processes. From quantum mechanics, rotational selection rule for interaction of an external field with an electric dipole is $\Delta J = 0, \pm 1$, and $\Delta K = 0$. So the dipole–dipole collision introduces rotational transition between adjacent rotational levels, i.e., $\ell' = \ell \pm 1$. $\gamma_{\ell\ell'}$ denotes the transition rate from $\ell \rightarrow \ell'$ and is obtained by multiplying the dipole–dipole transition rate γ_{DD} with the branching ratio with a Boltzmann factor $\rho_{\ell\ell'}$,

$$\gamma_{\ell\ell'} = \gamma_{\text{DD}} \rho_{\ell\ell'} \quad (2.10)$$

with

$$\gamma_{\text{DD}} = n_{\text{tot}} \langle v_{\text{rel}} \rangle \sigma_{\text{DD}} \quad (2.11)$$

where n_{tot} is the total population density, $\langle v_{\text{rel}} \rangle$ is the average relative velocity between colliding molecules,

$$\langle v_{\text{rel}} \rangle = \sqrt{\frac{16k_B T}{\pi m}} \quad (2.12)$$

in which m is the molecular mass in atomic mass unit. In (2.11), σ_{DD} is the dipole-dipole collision cross section. For methyl fluoride, σ_{DD} is measured to be 320 \AA^2 [21]. $\rho_{ll'}$ in (2.10) is written as

$$\rho_{J \rightarrow J+1} = \frac{(J+1)^2 - K^2}{(J+1)(2J+1)} e^{-\frac{\Delta E}{k_B T}}, \quad \text{and} \quad \rho_{J \rightarrow J-1} = \frac{J^2 - K^2}{J(2J+1)}, \quad (2.13)$$

in which J and K are the rotational quantum numbers, and ΔE is the energy difference between the two rotational levels [28].

In the second line in equation (2.9), $-\gamma_{\ell p}^{\text{SPT}} N_{\ell}^r$ describes a symmetry-preserving thermalization (SPT) process that moves non-thermal population in rotational level ℓ to its associated vibrational thermal pool p with the same A or E symmetry type [19]. The collisional cross section for SPT process is $\sigma^{\text{SPT}} = 137 \text{ \AA}^2$.

$-\gamma_{\ell p}^{\text{VS}} N_{\ell}^r$ describes a slower ‘‘V-swap’’ (VS) process that moves non-thermal rotational population to both A and E thermal pools with an equal probability [19]. Its cross section for CH_3F is $\sigma^{\text{VS}} = 21 \text{ \AA}^2$ at room temperature.

The pump rate term $R_{\text{pump}}(v, \mathbf{r}, t)$ in (2.9) involves only levels L and U associated with the infrared pump transition [28]:

$$R_{\text{pump}}(v, \mathbf{r}, t) = \left[N_{\text{L}}^{\text{tot}}(v, \mathbf{r}, t) - \frac{g_{\text{L}}}{g_{\text{U}}} N_{\text{U}}^{\text{tot}}(v, \mathbf{r}, t) \right] p_{\text{L} \rightarrow \text{U}} \cdot (\delta_{l, \text{U}} - \delta_{l, \text{L}}), \quad (2.14)$$

in which $N_{\text{L}}^{\text{tot}}(v, \mathbf{r}, t)$ and $N_{\text{U}}^{\text{tot}}(v, \mathbf{r}, t)$ are the total population for levels L and U, respectively. The total population is the sum of non-thermal and thermal population.

g_L and g_U are the degeneracies of L and U. And the transition probability $p_{L \rightarrow U}$ is given by

$$p_{L \rightarrow U} = \frac{8\pi^3}{3h^2c} \frac{|\langle J', K, V + 1 | \mu | J, K, V \rangle|^2}{\pi R^2} [P_{\text{pump}}^{\text{forw}} f_b^{\text{forw}}(\nu, \nu_p) + P_{\text{pump}}^{\text{back}} f_b^{\text{back}}(\nu, \nu_p)]. \quad (2.15)$$

Here, R is the cell radius, $|\langle J', K, V + 1 | \mu | J, K, V \rangle|^2$ is the dipole matrix element for the pump transition. For methyl fluoride, the dipole derivative square is obtained by experimental measurement as 0.027 Debye². A more detailed discussion of the dipole matrix element is found in Appendix G. $P_{\text{pump}}^{\text{forw}}$ and $P_{\text{pump}}^{\text{back}}$ are the effective pump intensities in both forward (incident direction of pump beam, or $+z$) and backward ($-z$) propagation directions by a z -average procedure over the self-consistent IR absorption coefficients. Detailed discussion on how to compute the absorption coefficients and effective pump intensities are present in the following section. In (2.15), $f_b(\nu, \nu_p)$ is the area-normalized lineshape function for the pump absorption. Here, it is a Lorentzian including pressure [31] and AC-Stark [32] broadening. Both forward and backward directions are included due to the reflection of the back mirror. In $f_b(\nu, \nu_p)$, ν_p denotes the pump frequency, and

$$\nu = \nu_0 \left(1 + \frac{v}{c}\right) \quad (2.16)$$

is the Doppler-shifted transition frequency for velocity v . So The following section provides the exact formulae and further discussions for $f_b(\nu, \nu_p)$.

The final term in equation (2.9) describes the spatial diffusion with a diffusion coefficient $D = \frac{1}{3} \langle v_{\text{abs}} \rangle \ell_{\text{mf}}$ where $\langle v_{\text{abs}} \rangle$ is the averaged absolute velocity and ℓ_{mf} is the mean free path [11] determined by temperature T , pressure p in mTorr, and gas-kinetic cross section σ_{GKC} :

$$\ell_{\text{mf}} = 0.732 \frac{T}{p \sigma_{\text{GKC}}}. \quad (2.17)$$

with $\sigma_{\text{GKC}} = 44 \text{ \AA}^2$ for CH_3F .

Similarly, the **rate equations for the vibrational thermal pools** for a symmetry type S ($= A$ or E) are written as:

$$\begin{aligned}
\dot{N}_{p,S}^v(\mathbf{r}, t) = & \sum_{p'} -\gamma_{pp'} N_{p,S}^v(\mathbf{r}, t) + \gamma_{p'p} N_{p',S}^v(\mathbf{r}, t) \\
& + \dot{N}_{p,S}^{VS}(\mathbf{r}, t) \\
& + \sum_{\ell} \left[\delta_{S,A} \gamma_{\ell p}^{\text{SPT}} + \frac{\gamma_{\ell p}^{\text{VS}}}{2} \right] \int dv N_{\ell}^r(v, \mathbf{r}, t) \\
& + D \nabla^2 N_{p,S}^v(\mathbf{r}, t).
\end{aligned} \tag{2.18}$$

Unlike the rotational population, we do not distinguish the vibrational-pool population $N_{p,S}^v$ by axial velocity since they do not directly absorb the pump. The first two terms describe the intermolecular collision between vibrational level $p \rightarrow p'$ and vice versa, for instance between v_3 and v_6 with a cross section $\sigma_{v_6 \rightarrow v_3} = 3.21 \text{\AA}^2$ [19]. V-swap transitions also occur among vibrational states, described by the second line in equation (2.18). We consider the most common form of this collision between a V_3A and a V_0E molecule: $V_3A + V_0E \leftrightarrow V_0A + V_3E$ [19]. This is a nonlinear process because the collisional rate depends on the unknown population of colliding molecules. A detailed description of the V-swap process is discussed in Appendix F. The third line in equation (2.18) describes the SPT and VS processes that move non-thermal rotational level ℓ to the associated vibrational thermal pool p , as described previously. The final term describes the diffusion as discussed above.

2.3.2 Line shape function, IR pump absorption, and effective pump intensity

As explained above, $f_b(\nu, \nu_p)$ is the area-normalized lineshape function including pressure [31] and AC-Stark [32] broadening. ν_p is the pump frequency, and ν is the transition frequency of molecules with axial velocity v . By the relativistic Doppler effect, $\nu^{\pm} = \nu_0(1 \pm v/c)$ for the forward (+) and backward (−) directions, where $\nu_0 = 31.04 \text{THz}$ is the intrinsic transition frequency between L and U for $^{13}\text{CH}_3\text{F}$. The

lineshape function $f_b^\pm(\nu^\pm, \nu_p)$ is a convolution of pressure and AC-Stark broadening effects:

$$f_b^\pm(\nu^\pm, \nu_p) = f_p(\nu^\pm, \nu_p) * f_S^\pm(\nu^\pm, \nu_p)$$

where

$$f_p(\nu^\pm, \nu_p) = \frac{1}{\pi} \frac{\Delta\nu_p}{(\nu^\pm - \nu_p)^2 + \Delta\nu_p^2}$$

is the pressure broadening line shape function with linewidth proportional to gas pressure:

$$\Delta\nu_p = \frac{1}{2\pi\Delta\tau} \approx 15 \text{ MHz/Torr} \quad (2.19)$$

in which $\Delta\tau$ is the mean collision time [28]). The AC-Stark broadening line shape function $f_S^\pm(\nu^\pm, \nu_p)$ can also be approximated by a Lorentzian with linewidth [32]

$$\Delta\nu_S^\pm = \frac{|\langle J', K, V + 1 | \mu | J, K, V \rangle|}{2\pi\hbar} \sqrt{\frac{2P_{\text{pump}}^\pm}{\pi\epsilon_0 c R}} = 0.38 \frac{\sqrt{P_{\text{pump}}^\pm/\text{Watt}}}{R/\text{cm}}.$$

Note that the average pump power P_{pump}^\pm is different for the $+z$ direction and the reflected power in the $-z$ direction, as described below. The convolution of two Lorentzians is also a Lorentzian with the sum of the linewidths, so we obtain

$$f_b^\pm(\nu^\pm, \nu_p) = \frac{1}{\pi} \frac{\Delta\nu^\pm}{(\nu^\pm - \nu_p)^2 + (\Delta\nu^\pm)^2} \quad (2.20)$$

with

$$\Delta\nu^\pm = \Delta\nu_p + \Delta\nu_S^\pm. \quad (2.21)$$

Infrared pump absorption coefficient as a function of radial position r is integrated over all velocity subclasses [28]

$$\alpha^\pm(r) = \frac{8\pi^3\nu_p}{3hc} |\langle J', K, V + 1 | \mu | J, K, V \rangle|^2 \int g^\pm(v) \left[N_L^{\text{tot}}(v, r) - \frac{g_L}{g_U} N_U^{\text{tot}}(v, r) \right] dv \quad (2.22)$$

in which h is the Planck constant, c is the speed of light, R is the cavity radius, ν_p is the pump frequency, and $|\langle J', K, V + 1 | \mu | J, K, V \rangle|^2$ is the dipole matrix element for the pump transition. For methyl fluoride, the dipole derivative square is 0.027 Debye^2 [28]. $g^\pm(v) = f_b^\pm(\nu^\pm(v), \nu_p)$ is the pump absorption line shape function for molecules with axial speed v . $g^\pm(v)$ peaks when the pump frequency ν_p is equal to the Doppler-shifted transition frequency for v . Note that $\alpha^\pm(r)$ is different in the forward (+) and backward (−) directions since they have different Doppler shifts and different population distributions.

The spatially averaged pump absorption coefficient is obtained by:

$$\alpha^\pm = \frac{\int_0^R \alpha^\pm(r) r dr}{\int_0^R r dr}.$$

Figure Fig. 2-3 shows the IR absorption spectrum α^+ in the forward direction at 100 mTorr and 400 mTorr with various input pump powers. $\nu_0 = 31.0427 \text{ THz}$ is the center frequency for the L–U transition, while the CO_2 pump laser is incident at a frequency 25 MHz greater than ν_0 , i.e., $\nu_p = \nu_0 + 25 \text{ MHz}$. The figure shows a dip at the pump frequency because of reduced population in the L level. This is also called inhomogeneous broadening. The width of the dip increases with pressure and pump power, as described in (2.21). The width becomes so broad at 400 mTorr that its effect is hard to see. There is an extra dip at -25 MHz from the reflection at the back mirror of the cavity, with a relatively weaker strength due to weaker effective intensity of the reflected pump.

Insider the cavity, the pump photon travels back and forth, reflects off of the front and back gold-coated copper mirrors, and transmits through the pinhole in the front

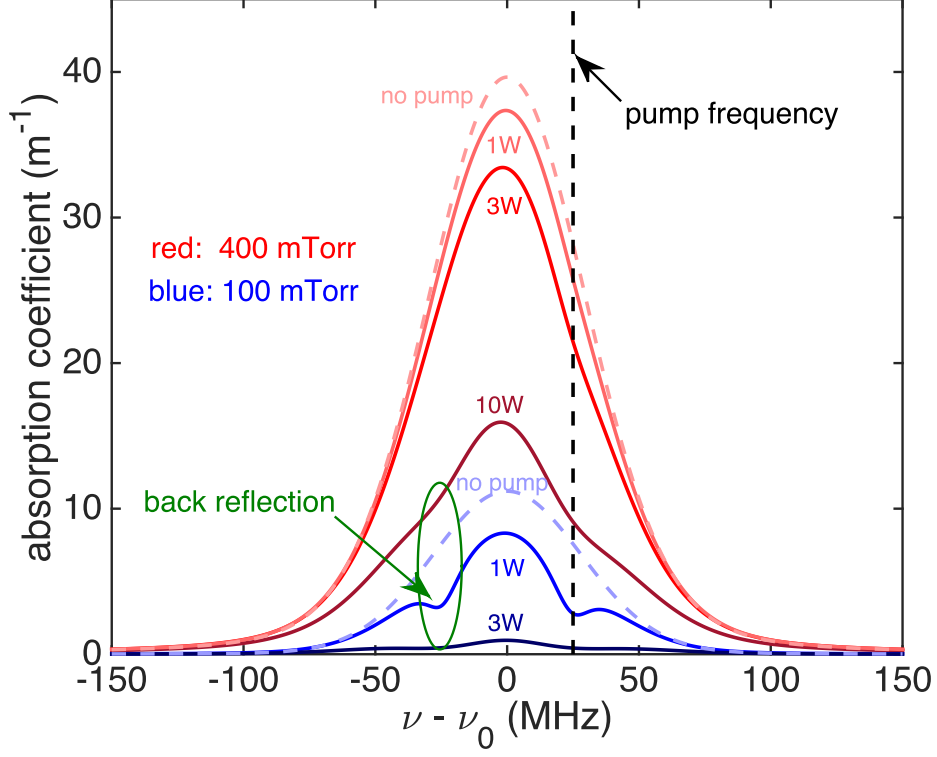


Figure 2-3: IR absorption spectrum at 100 mTorr and 400 mTorr with various input pump powers. $\nu_0 = 31.0427$ THz is the frequency of the L-U transition, while the CO₂ pump laser is incident at a frequency 25 MHz $> \nu_0$.

mirror. We sum all the trips to obtain an effective z -averaged pump power in each direction. The loss for one round trip is $(1 - \beta)$ with

$$\beta = R_1 R_2 e^{-(\alpha^+ + \alpha^-)L} \quad (2.23)$$

where R_2 is the reflection on the back mirror at the pump frequency. Here, we have $R_2 = 0.95$. $R_1 = 0.96 \times 0.95 = 0.912$ is the reflection of the front mirror considering an extra 4% leakage from the pinhole. Then the z -averaged effective pump power is computed by:

$$P_{\text{pump}}^+ = \frac{P_0}{1 - \beta} \frac{\int_0^L \exp(-\alpha^+ z) dz}{L} = \frac{1}{1 - \beta} \frac{1 - \exp(-\alpha^+ L)}{\alpha^+ L} P_0 \quad (2.24)$$

$$P_{\text{pump}}^- = \frac{R_2 \exp(-\alpha^+ L)}{1 - \beta} \cdot \frac{1 - \exp(-\alpha^- L)}{\alpha^- L} P_0 \quad (2.25)$$

where P_0 is the input pump power. If the round trip loss and the absorption coefficient are small enough, the effective pump intensity can be greater than the incident pump power due to pump-photon accumulation inside the cavity. While if the absorption coefficient is big enough, the effective pump intensity can be much smaller than the incident power due to fast decaying.

Note that the lineshape functions, pump absorption coefficients, and the effective pump intensities introduce nonlinearities to the rate equations. We will discuss how to numerically solve the nonlinear rate equations self-consistently in later sections.

2.3.3 Molecule–wall collisions and boundary conditions

Molecule–wall collision is the primary vibrational relaxation pathways of molecules. The wall collision process in a cylindrical cell depends on molecular diffusion, which acts to produce a radial spatial variation in the molecular population. Furthermore, the wall collision produces a Boltzmann distribution of the population based on the wall temperature (300K). Therefore, the majority of vibrationally excited molecules are de-excited to v_0 after wall collision, and are distributed thermally in the two thermal pools (A and E types) of v_0 while preserving symmetry type.

Traditionally, a wall-collision rate k_w was introduced in the rate equations. For example in Ref. [11], k_w at a radial position r ($0 < r < R$) was approximated as

$$k_w = \begin{cases} v_{\text{avg}}\ell_{\text{mf}}/(R-r)^2 & \text{if } r \in [0, \max(0, R - \ell_{\text{mf}})] \\ v_{\text{abs}}/(R-r) & \text{if } r \in [\max(0, R - \ell_{\text{mf}}), R]. \end{cases}$$

Here, ℓ_{mf} is the pressure-dependent mean free path, v_{avg} is the average relative velocity between molecules, and v_{abs} is the average absolute velocity of molecules. Even though k_w is qualitatively correct in that it increases as r approaches the wall, this simplified treatment of the wall collision rate was increasingly inadequate at high operating pressures above 1 Torr. Though we can re-derive k_w more rigorously by integrating the molecule–wall colliding angle, k_w as a function of position r per se is an approximation since wall collision occurs just at the wall. The diffusion term $D\nabla^2 N$ already captures

the motion of molecules to/from the wall, so a purely local boundary condition is more correct than the nonlocal collision rate used previously [11].

We use a standard Neumann boundary condition ($\partial N/\partial r = 0$) for rotational population to represent impermeable walls, but with a different vibrational-level boundary condition that expresses the wall relaxation. As discussed above, wall collisions thermalize the vibrational levels and redistribute molecules into all possible vibrational levels of the same symmetry S according to a Boltzmann distribution characterized by T_{wall} . Note that the population flux in \hat{r} (or \hat{n}) direction is

$$-D\nabla N = -D\frac{\partial N}{\partial r}\hat{n}.$$

A Robin boundary condition similar to “surface-reaction” boundary conditions used in chemistry [33] is applied for vibrational thermal pool p :

$$-D\frac{\partial N_p}{\partial r} = \bar{v}(1 - q_p)N_p/2 - \bar{v}q_p\sum_{p'\neq p}N_{p'}/2, \quad \text{at } r = R \quad (2.26)$$

in which q_p is the population fraction of vibrational level p for a Boltzmann distribution at the wall temperature ($T_{\text{wall}} = 300\text{K}$) and \bar{v} is the average velocity of the population flux perpendicular to the wall. Appendix B shows $\bar{v} = \langle v_{\text{abs}} \rangle/2$. The factor of $1/2$ in (2.26) comes from the consideration that only half of the population move towards the wall.

2.3.4 Numerical solver: fixed point iteration and Anderson acceleration

In this section, we will discuss how to build a numerical solver with enormous computational improvement that allows us to include not only millions of population degrees of freedom but also many physical processes that other authors neglected or approximated. In particular as discussed in previous sections, we include dipole–dipole collisions between rotational states, SPT between nonthermal rotational states and vibrational thermal pools, the V-swap process, molecule–wall collisions, and spatial

diffusion. For the inhomogeneously broadened pump absorption, we include Doppler, AC-Stark, and pressure broadening of all velocity subclasses, and we determine the z -average pump intensity self-consistently, including spectral hole burning and pump saturation, with the absorption coefficient calculated from the populations.

Given a set of nonlinear rate equations, most authors evolve them in time until the steady state is obtained [11], but this approach is severely inefficient, especially at high pressures where timescales for different relaxation processes diverge widely. Instead, we solve for the steady state directly, without time evolution, by setting

$$\dot{N}_\ell = 0, \quad \dot{N}_p = 0 \quad (2.27)$$

in Eqs. (2.9, 2.18). The nonlinearity of the rate equations arises from the pump term, V-swap collision between vibrational levels, and the EVT model discussed in the following section.

Our nonlinear solver is based on the fixed-point iteration with Anderson acceleration (AA) [34].

Fixed point iteration is a convenient numerical method for solving nonlinear equations. We can write the problem in a general form of

$$\mathcal{A}(\mathbf{p}, \mathbf{x})\mathbf{x} = \mathbf{b}(\mathbf{p}), \quad (2.28)$$

where \mathbf{x} is the unknown population density, \mathbf{p} denotes parameters of molecular properties, collisional cross sections, and pump parameters, $\mathcal{A}(\mathbf{p}, \mathbf{x})$ is the matrix describing the collisional transitions, pump process, and diffusion. $\mathcal{A}(\mathbf{p}, \mathbf{x})$ nonlinearly depends on both the population density \mathbf{x} and parameters \mathbf{p} . \mathbf{b} is related to the pump. The solution

$$\mathbf{x} = \mathcal{A}[\mathbf{p}, \mathbf{x}]^{-1}\mathbf{b} \equiv \mathbf{g}(\mathbf{x}), \quad (2.29)$$

can be numerically computed by the fixed-point iteration:

$$\begin{aligned}
& \text{initial guess: } \mathbf{x}_0, \\
& \text{do: } \mathbf{x}_1 = \mathbf{g}(\mathbf{x}_0), \\
& \quad \mathbf{x}_2 = \mathbf{g}(\mathbf{x}_1), \\
& \quad \dots \\
& \quad \mathbf{x}_n = \mathbf{g}(\mathbf{x}_{n-1}), \\
& \text{until convergence: } \frac{\|\mathbf{x}_n - \mathbf{x}_{n-1}\|}{\|\mathbf{x}_n\|} < \epsilon
\end{aligned}$$

where ϵ is the convergence criterion for the relative error.

The fixed-point iteration doesn't require the computation of Jacobian matrix as required in other popular nonlinear solvers such as Newton's method. This makes it extremely convenient to add and modify the collisional terms straightforwardly without deriving the derivatives. It also allows us to easily turn on and off each physical collisional process, and efficiently helps to explore the importance of all the collisional processes.

One practical problem of the fixed-point iteration is that the algorithm doesn't converge when the nonlinearity increases with increasing pump power. The solution is to use a different fixed-point form based on the convergent solution with smaller pump power. In particular, assume the solution \mathbf{x}_0 with parameter \mathbf{p}_0 based on the above simple algorithm is obtained. For parameter \mathbf{p} with higher pump power, the fixed-point problem is modified as

$$\mathcal{A}[\mathbf{p}, \mathbf{x}] = \mathcal{A}[\mathbf{p}_0, \mathbf{x}_0] + \mathcal{B}[\mathbf{p}, \mathbf{x}], \quad (2.30)$$

$$\mathbf{g}(\mathbf{x}) = \mathcal{A}[\mathbf{p}_0, \mathbf{x}_0] \setminus (\mathbf{b} - (\mathcal{A}[\mathbf{p}, \mathbf{x}] - \mathcal{A}_0[\mathbf{p}_0, \mathbf{x}_0])\mathbf{x}) \quad (2.31)$$

This new fixed-point formula not only overcomes the divergence issue for $\mathbf{p} \approx \mathbf{p}_0$, but also dramatically saves the computational time because the matrix $\mathcal{A}[\mathbf{p}_0, \mathbf{x}_0]$ needs only one factorization for all iterations.

Another way to improve the convergence rate of the fixed-point iteration is to use

the Anderson Acceleration (AA) scheme [34]. Instead of updating the solution by $\mathbf{x}_{k+1} = \mathbf{g}(\mathbf{x}_k)$, AA updates the solution as a linear combination of multiple previous steps:

$$\mathbf{x}_{k+1} = \sum_{i=0}^{m_k} \alpha_i^{(k)} \mathbf{g}(\mathbf{x}_{k-m_k+i}) \quad (2.32)$$

$$\text{subject to} \quad (2.33)$$

$$\min_{\alpha_i^{(k)}} \left\| \sum_{i=0}^{m_k} \alpha_i^{(k)} \mathbf{f}_i \right\|_2, \quad \text{s.t.} \quad \sum_{i=0}^{m_k} \alpha_i^{(k)} = 1. \quad (2.34)$$

where $m_k = \min(m, k)$ is the number of previously steps used to span the new solution space, subject to condition that linear coefficients $\alpha_i^{(k)}$ minimize the residuals, with $\mathbf{f}_i = \mathbf{g}(\mathbf{x}_i) - \mathbf{x}_i$ being the residual at step i . The solution to (2.34) gives the AA algorithm [34]

$$\mathbf{x}_{k+1} = \mathbf{g}(\mathbf{x}_k) - \sum_{i=0}^{m_k-1} \gamma_i^{(k)} [\mathbf{g}(\mathbf{x}_{k-m_k+i+1}) - \mathbf{g}(\mathbf{x}_{k-m_k+i})] \quad (2.35)$$

$$= \mathbf{x}_k + \mathbf{f}_k - (\mathcal{X}_k + \mathcal{F}_k) \boldsymbol{\gamma}^{(k)} \quad (2.36)$$

where $\mathcal{X}_k = (\Delta \mathbf{x}_{k-m_k}, \dots, \Delta \mathbf{x}_{k-1})$ with $\Delta \mathbf{x}_i = \mathbf{x}_{i+1} - \mathbf{x}_i$, $\mathcal{F}_k = (\Delta \mathbf{f}_{k-m_k}, \dots, \Delta \mathbf{f}_{k-1})$ with $\Delta \mathbf{f}_i = \mathbf{f}_{i+1} - \mathbf{f}_i$, and $\boldsymbol{\gamma}^{(k)} = (\mathcal{F}_k^T \mathcal{F}_k)^{-1} \mathcal{F}_k^T \mathbf{f}_k$ assuming \mathcal{F}_k is full ranked. The idea of updating the new solution based on multiple previous steps is similar to Krylov space. It can be proved that Anderson acceleration is “essentially equivalent” in a certain sense to the GMRES method for solving linear problems [34].

Figure 2-4 shows the convergence rate of the fixed-point iteration with and without AA. In the example, the gas pressure is 800 mTorr, and the pump power is 5.0 Watt. The solver converges within 30 iterations without AA, while the same problem converges within 12 Anderson iterations. Typically, AA improves the convergence rate by a factor of 2 or more.

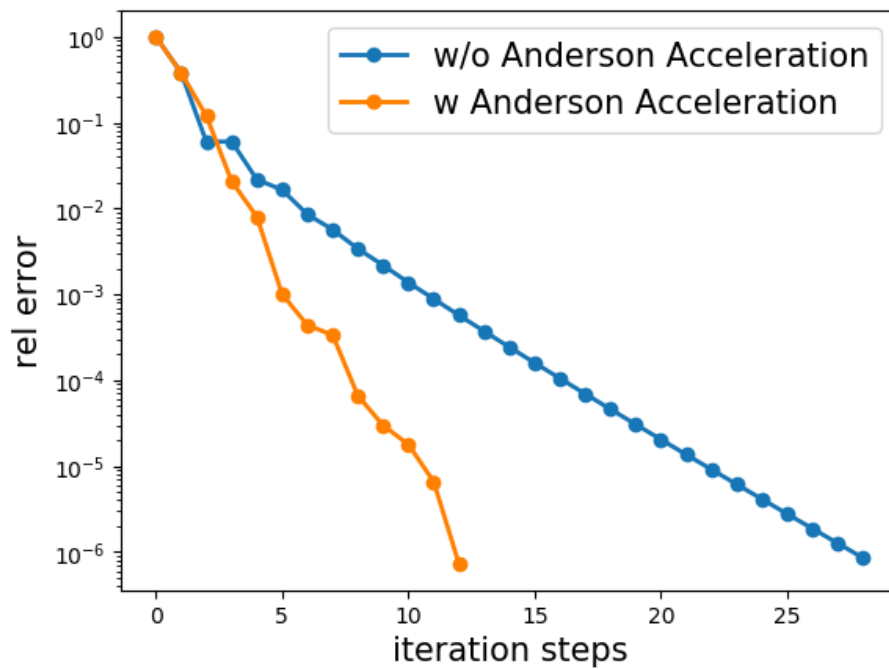


Figure 2-4: Convergence rate with (orange) and without (blue) Anderson acceleration. In this example, the gas pressure is 800 mTorr and the pump power is 5.0 Watt. The solver converges within 30 iterations without Anderson acceleration, while the same problem converges within 12 Anderson iterations.

2.4 Numerical modeling: terahertz output power

Up to now, we have presented how the population rate equations are developed and solved. In this section, we will discuss how to compute the terahertz output power based on the population inversion obtained from the rate equations.

The lasing output power is obtained by matching terahertz cavity loss α_{THz} with the gain coefficient $\langle\gamma\rangle$:

$$\alpha_{\text{THz}} = \langle\gamma\rangle = \frac{\int_V \gamma(\nu, r) |\mathbf{E}(r)|^2 d\mathbf{r}}{\int_V |\mathbf{E}(r)|^2 d\mathbf{r}}. \quad (2.37)$$

Here, the gain coefficient $\gamma(\nu, r)$ is averaged over the mode profile. Cavity loss α_{THz} includes ohmic loss and leakage through the front window. Ohmic loss can be computed analytically for the modes of a hollow metal waveguide [35]. The lowest-loss mode is TE_{01} , but which mode lases will depend on the degree of radial and frequency overlap between the gain and mode profiles. We'll show later that we use the α_{THz} from TE_{01} for all calculations except for refilling lasing with input pump power 6.6W to match the experiments, indicating that the model could enable us to determine which mode is lasing without directly measuring the mode profile!

Since the gain is a small perturbation ($< 0.01\%$) to the permittivity, the electric field $\mathbf{E}(r)$ is accurately approximated by the passive waveguide mode. For convenience, we normalize the mode so that $\int_V |\mathbf{E}(r)|^2 d\mathbf{r} = \int_V d\mathbf{r} = V$. The gain coefficient $\gamma(\nu, r)$ at lasing frequency ν and radial position r is then expressed as [31]

$$\gamma(\nu, r) = \int dv \frac{\Delta N(v, r) \sigma(\nu)}{1 + \Phi |\mathbf{E}(r)|^2 / \Phi_s} \quad (2.38)$$

which includes contributions from all velocity subclasses. $\Delta N(v, r)$ is the population inversion obtained by solving the rate equations, and $\sigma(\nu)$ is the transition cross section:

$$\sigma(\nu) = \frac{\lambda^2 g(\nu)}{8\pi t_{\text{sp}}}, \quad (2.39)$$

where λ is the lasing wavelength, the spontaneous emission lifetime t_{sp} is taken to be 10 sec [11], much longer than all other transition lifetimes in the system (see Appendix D for a detailed discussion: t_{sp} has little effect on the peak efficiency), and

$$g(\nu) = \frac{1}{\pi} \frac{\Delta\nu_p}{(\nu - \nu_v)^2 + \Delta\nu_p^2} \quad (2.40)$$

is the pressure-broadened lineshape function (ν_v is the center frequency for molecules with velocity v) as discussed in Section (2.3.2). Φ_s in (2.38) is the saturated photon flux density:

$$\Phi_s = \frac{1}{\tau_s \sigma(\nu)}, \quad (2.41)$$

where τ_s is the characteristic time for the lasing transition. Unlike a three- or four-level system in which τ_s can be analytically derived [31], our system requires τ_s to be obtained numerically from the model. A stimulated emission rate w_{st} is introduced between the two lasing levels, and τ_s is obtained by fitting the population inversion as a function of w_{st} :

$$\Delta N(w_{\text{st}}) = \frac{\Delta N(w_{\text{st}} = 0)}{1 + \tau_s w_{\text{st}}}. \quad (2.42)$$

Once all ΔN , σ , Φ_s and cavity mode $\mathbf{E}(r)$ are known, we numerically solve equation (2.37) for the intensity of photon flux density Φ by a Newton method. Finally, the THz output power is obtained from

$$I_o = \frac{1}{2} (h\nu) \pi R^2 T \Phi \quad (2.43)$$

where R is the radius of the cavity and T is the transmission coefficient, computed by integrating the waveguide mode's Poynting flux over the output pinhole (since the pinhole is comparable to the wavelength; see Appendix C). The formula has a factor of 1/2 to count only photons flowing in the outward direction [31].

2.5 Effective temperature model

Even with including all the complicated physical collisions in the model, the steady-state computation efficiency, and an accurate way to compute the output power, the sheer complexity of the inversion process still makes it extremely challenging to model accurately.

As mentioned in Section 2.2, previous models needed to make many simplifying assumptions, and the reason they produced unphysical bottlenecks at high pressures was conjectured to be their inclusion of only two key vibrational levels, e.g., v_0 and v_3 for $^{13}\text{CH}_3\text{F}$. We confirmed this conjecture with our model by artificially “turning off” collisional processes one by one, as shown in Fig. 2-5. The only process that circumvented vibrational bottlenecks was the process by which higher-lying vibrational levels are populated. The difficulty of including these higher-lying vibrational levels seems almost insurmountable at first: Although the energies of hundreds of vibrational levels are known [28], the relaxation processes among them are not known quantitatively and are infeasible to measure.

To deal with that problem, a crucial theoretical innovation of our work is to describe those levels implicitly via an effective temperature (different from the ambient temperature!) that is determined self-consistently from the few collisional cross-sections whose values are known. Specifically, we make the ansatz that vibrational transitions are rapid enough to “thermalize” those levels with a Boltzmann distribution described by an effective temperature T_v , so they may be grouped together into separate population pools v_Σ for the A and E symmetries, as shown in Fig. 2-2(b). This expandable thermal pool contains all 120 vibrational levels higher than v_3 up to 6959 cm^{-1} ($\sim 35k_B T_{\text{wall}}$), taking into account the specific energies and degeneracies of each.

This is similar to the experimentally justified thermal-pool assumption [18] that maintains a constant temperature among rotational states within a given symmetry type and vibrational level. The main justification of this ansatz is that thermalization among vibrational states is through bimolecular collisions, meaning the rates increase

with pressure, while vibrational-state relaxation occurs through diffusion to the walls, which goes as the inverse of pressure. Therefore, the higher the pressure, the more vibrational thermalizing collisions occur before diffusion to the walls relaxes the excitation, and so our model becomes more accurate precisely in the high-pressure regime where these extra vibrational levels are relevant to the inversion.

To implement this thermalization ansatz, the populations of v_0 and v_3 are calculated explicitly, and we then assign the effective temperature of the remaining vibrational levels to be

$$T_v^S = -\frac{\Delta E}{k_B} \frac{1}{\log(N_{3,S}^{\text{tot}}/N_{0,S}^{\text{tot}})} \quad (2.44)$$

where $\Delta E = E_3 - E_0$ is the energy difference between v_3 and v_0 . In order to maintain the Boltzmann distribution for v_Σ , transition rates between v_3 and v_Σ are introduced and satisfy the Boltzmann relation:

$$\frac{\gamma_{3 \rightarrow \Sigma}}{\gamma_{\Sigma \rightarrow 3}} = \exp\left(\frac{E_3 - \sum_{k \in V_\Sigma} g_k E_k}{k_B T_v^S}\right), \quad (2.45)$$

By taking the limit $\gamma_{3 \rightarrow \Sigma}, \gamma_{\Sigma \rightarrow 3} \rightarrow \infty$ in the rate equations, we obtain

$$N_{\Sigma,S}(r) = \exp\left(\frac{E_3 - \sum_{k \in V_\Sigma} g_k E_k}{k_B T_v^S}\right) N_{3,S}(r). \quad (2.46)$$

There are three vibrational rate equations associated with v_0 , v_3 and v_Σ in (2.18). One of them can be replaced by (2.46). In fact, another equation can be replaced by the conservation of population (See Appendix E)

$$N_0(\mathbf{r}) + N_3(\mathbf{r}) + N_\Sigma(\mathbf{r}) = 0. \quad (2.47)$$

These simplifications decrease the nonlinearities of the rate equations and improve the convergence rate.

2.5.1 Experiment-theory comparison

Here, we first demonstrate the unphysical bottlenecking phenomena by including all the rotational levels as shown in Fig. 2-2, but only the 6 vibrational levels that are most directly connected to the lasing energy levels. In this 6-level model, we included all of the other processes discussed before. The *only* difference is that it has no effective temperature to model the “missing” higher-lying vibrational levels, and the population of all 6 vibrational levels is solved exactly. The output THz powers with different input pump powers (3.3 W, 6.6 W, and 10 W) are shown in Fig. 2-5. We find the return of the vibrational bottleneck as in previous work: The inversion disappears above 700 mTorr for all input pump powers, which is qualitatively different from the experimental observations in Fig. 2-6A.

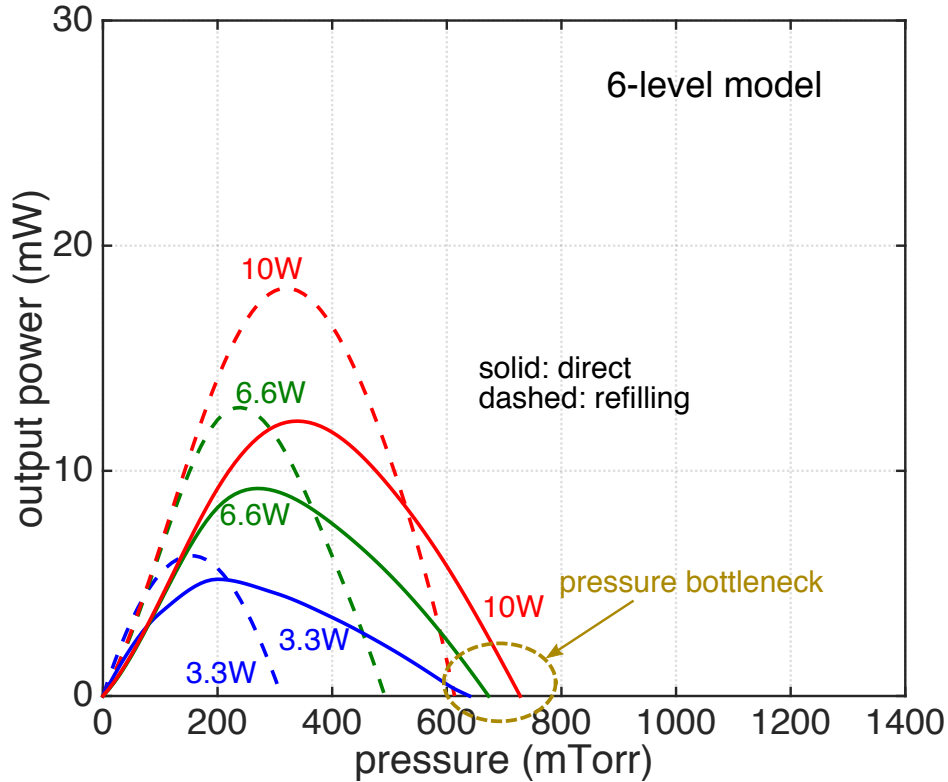


Figure 2-5: Reproduction of the artificial high-pressure bottlenecking: Prediction of the THz output powers by a 6-level model, for various input pump powers (3.3W, 6.6W, and 10W), and for both the direct (solid lines) and refilling (dashed lines) transitions. It is clearly observed that no gain is obtained above 700 mTorr by the 6-level model, known as high-pressure unphysical bottlenecking.

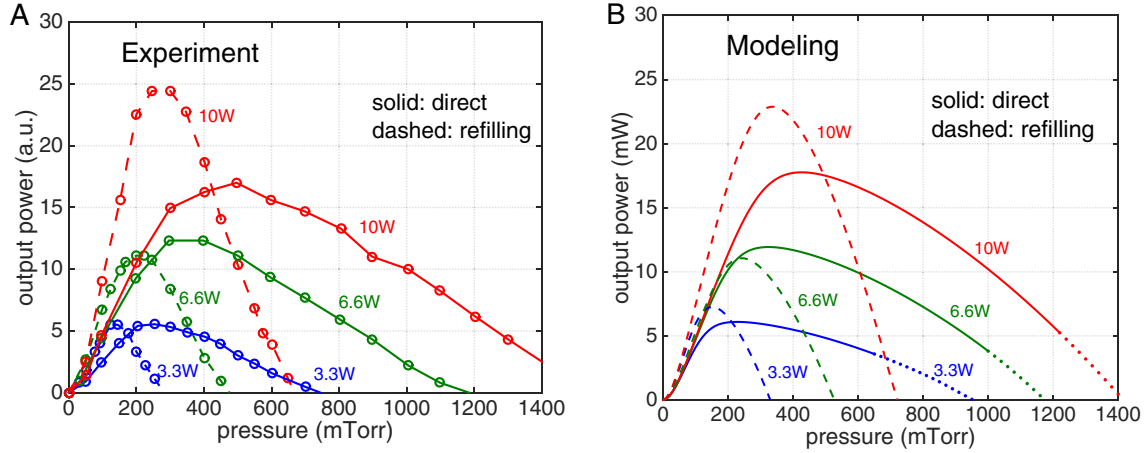


Figure 2-6: (a) Experimental and (b) theoretical THz laser output power as a function of gas pressure, for various input pump powers (3.3W, 6.6W, and 10W), and for both the direct (solid lines) and refilling (dashed lines) transitions. Excellent agreement is obtained even though the theoretical model has no adjustable parameters; in contrast to previous work [10–13], our theory captures the fact that higher powers allow operation at higher pressures, in part because of a novel technique to model a large number of high-energy vibrational levels. The dotted parts of the direct lasing curves represent an inefficient regime in which the pump intensity is nearly zero in the back of the cavity. In this case our model’s approximation of an effective z -uniform pump strength is inaccurate, but it is not desirable to operate in this regime.

On the other hand, with the effective temperature model, Fig. 2-12 shows excellent agreement between the experimentally measured power and the predictions of our *ab-initio* model, with no free parameters except for the overall scaling, even for pressures >1 Torr where all previous models exhibited bottlenecking. This confirms the long-held understanding that including only few vibrational levels in the model induces the unphysical high-pressure quenching of the inversion through vibrational bottlenecking.

In comparing the experimental results to the theoretical model, it is important to keep in mind that there are significant experimental variabilities that limit reproducibility. Among the largest sources of variability are $\sim \pm 10$ MHz drift in the pump frequency offset, $\sim \pm 2 \mu\text{m}$ drift in cavity length from the optimal for a given terahertz inversion, and $\sim 10\%$ rise in the cavity pressure over the course of a measurement. A final source of variability is that the optimal tuning for the refilling transition is different from that for the direct transition. Given these variabilities, the excellent,

roughly quantitative agreement with our model provides striking confirmation of its validity.

In the dotted parts of Fig. 2-6, the pump is highly focused in the front of the cavity and quickly decays to nearly zero ($<2\%$) by the back of the cavity, in which case our model's approximation of an effective z -uniform pump strength is inaccurate, and hence the slight mismatch with experiment is unsurprising. Accurately modeling this attenuated-pump regime is relatively unimportant because that regime "wastes" the end of the cavity, and it is preferable to use a shorter cavity.

Since the lasing-mode pattern could not be observed directly in the experiment, we compute the terahertz cavity loss from the lowest-loss TE_{01} mode for all curves except for the refilling lasing with input pump power 6.6 W. The 6.6-W experimental refilling curve exhibited a jump in amplitude compared with adjacent powers. We deduce that this is due to a different mode being excited by a mistuned cavity – using the cavity loss and mode profile from the TE_{22} mode produced the best fit to the data. In this way, the accuracy of the model enables us to determine which mode is lasing without directly measuring the mode profile!

The effective temperature T_v for the A-type vibrational thermal pools as a function of radial position and molecular pressure is shown in Fig. 2-7(a), which provides a deeper understanding of the system dynamics. The input pump power is 10W and the cavity length is 14.3 cm. From the figure, T_v is higher in the cell center, where the pump is more saturated and the gain is smaller. One would normally expect T_v to increase with pressure due to faster intermolecular collisions, but in this figure T_v actually *decreases* above 400 mTorr because the z -averaging of the pump power lowers the pump rate and brings the effective temperature down. T_v with optimal cavity length (which decreases with pressure so that the whole cavity remains pumped) as discussed in the following section, the result as shown in Fig. 2-7(b) exhibits effective temperatures that increase with pressure as expected.

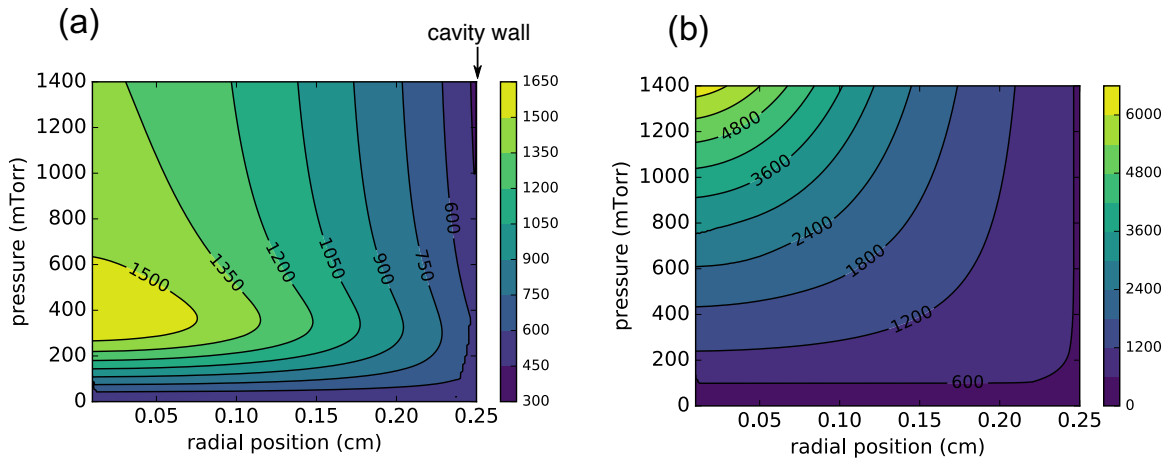


Figure 2-7: The effective temperature T_v (in Kelvin) of type-A vibrational thermal pools as a function of radial position and molecular pressure, for an input pump power of 10W, with (a) cavity geometry in experiments, and (b) optimal cavity length as discussed in Section 2.7.

2.6 More theoretical results and discussion

The agreement between theory and experiment allows us to use the theory to thoroughly study the OPFIR laser system dynamics.

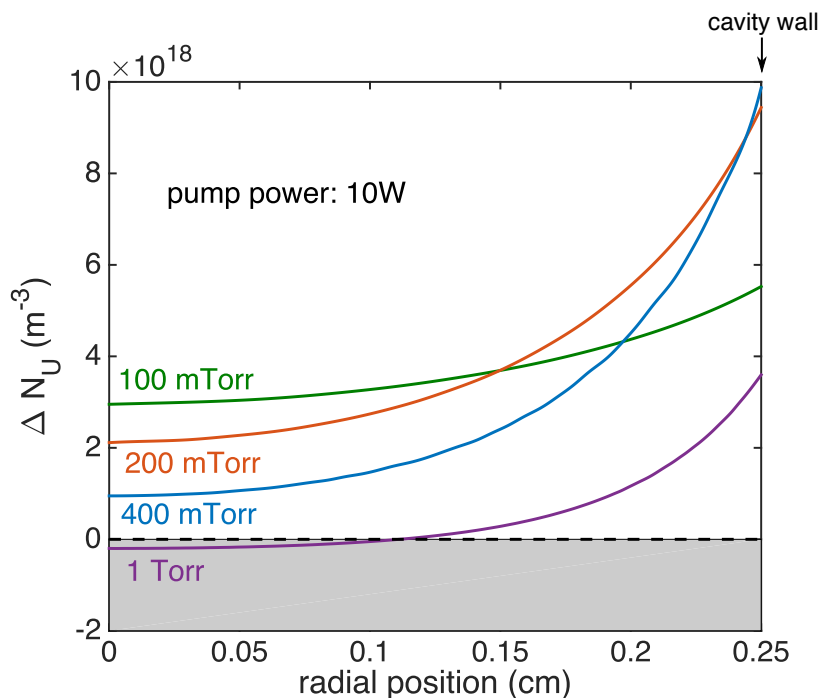


Figure 2-8: Radial distribution of population inversion for direct transition at 100 mTorr, 200 mTorr, 400 mTorr, and 1 Torr, with 10W input pump power.

The radial-direction modeling results show clear evidence of the spatial dependence of the gain: Gain is larger when it gets closer to the cavity wall, which is indicated in Fig. 2-7 of last section. Here, a more direct calculation of the population inversion for direct transition ΔN_U as a function of radial position at 100 mTorr, 200 mTorr, 400 mTorr, and 1 Torr with 10W input pump power is shown in Fig. 2-8. Population inversion, as well as the gain coefficient is larger at the cell wall. This insight is crucial for cavity design that adding transparent walls inside the cavity for both IR pump and THz radiation can potentially decrease the pump threshold and increase the gain and THz power.

Furthermore, operating OPFIR laser sources at high pressures leads to an unusually broad and flat gain profile. Gain spectrums at 100 mTorr and 400 mTorr with different pump powers are shown in Fig. 2-9. The width of this pressure-broadened

gain profile is proportional to the gas pressure, as shown in (2.40). Such flat gain profiles potentially allow the terahertz lasing frequency to be tuned over a correspondingly broad range ($\sim \pm 10$ MHz at a few hundred millitorrs) without sacrificing efficiency.

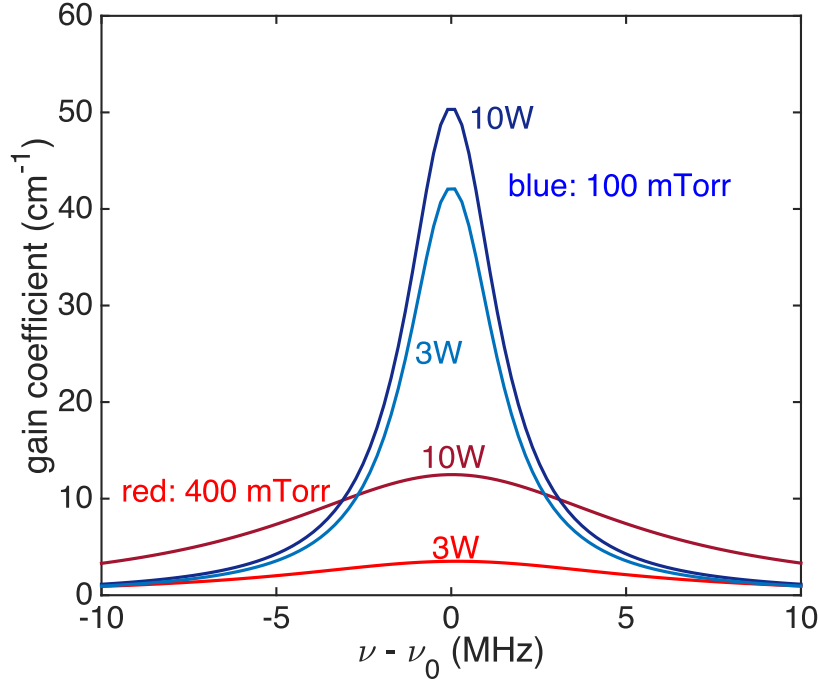


Figure 2-9: THz gain spectrum at 100 mTorr and 400 mTorr with the input pump power equal to 3W and 10W. The width of spectrum is proportional to the gas pressure due to pressure broadening.

Additionally, we can compare the significance of different collisions. Figure 2-10 plots the output power as a function of pressure for the full model, the 6-level model, the full model without the V-swap collision, the full model without the SPT collision, and the full model without the dipole-dipole collision. Pump power in the calculation is fixed as 6.6 W. As discussed before, the 6-level model excludes the high-lying vibrational modes and only introduces a low-pressure cutoff around 700 mTorr. The significance of different collisional terms is clearly seen through comparison between the results without the collisional term and the full model. The V-swap collision has smallest influence on the output power, due to its small collisional cross section 21\AA^2 . Both the SPT and the dipole-dipole collisions are important for the lasing behavior. The SPT process transfers nonthermal population to the

thermal pool, effectively enhancing the relaxation process, so that reducing the SPT process reduces the output power. While the dipole–dipole collision thermalizes the nonthermal population between rotational levels, and decreasing its cross section simply adds more population in the U level and produces larger output power.

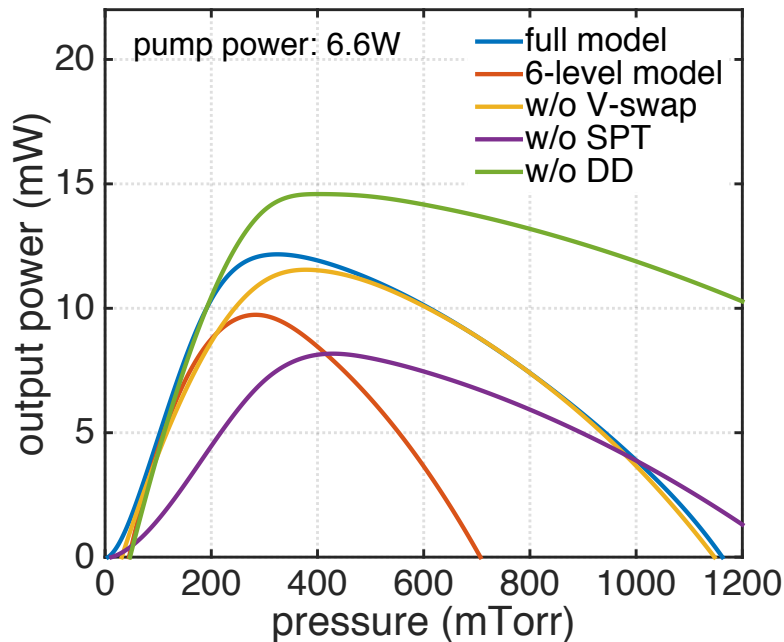


Figure 2-10: Significance of different collisional terms: Comparison between the full model, the 6-level model, the full model without the V-swap collision, the SPT process, and the dipole–dipole collision. The comparison shows that the SPT, DD collisions, as well as the effective temperature model are the most important to obtain accurate results, while the V-swap process with small collisional cross section doesn’t affect the output power too much.

With the accurate *ab-initio* modeling, we can easily assess the attainable quantum efficiency of the laser quantitatively, a parameter which was difficult to measure in our experiment because only a fraction of the emitted photons were detected by our heterodyne receiver. Figure 2-11 plots the predicted lasing threshold and differential quantum efficiency (DQE) at the threshold, defined as

$$\eta_d = \frac{dP_{\text{out}}}{dP_{\text{pump}}} / \frac{\nu_{\text{out}}}{\nu_{\text{pump}}}. \quad (2.48)$$

The figure shows that the direct transition has lower pump threshold, but its

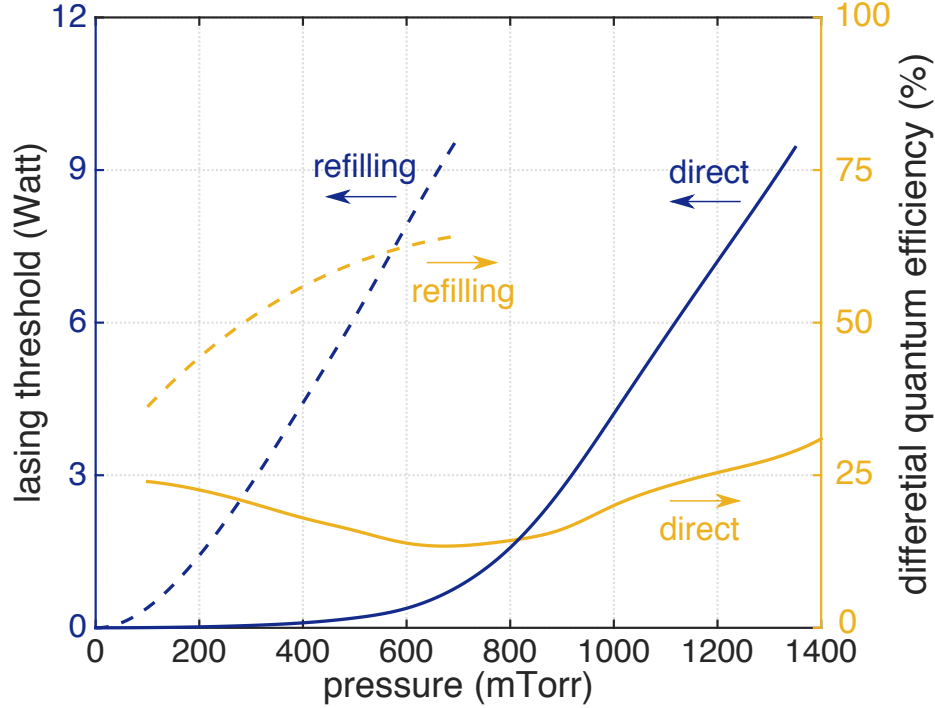


Figure 2-11: The input pump power at lasing threshold (blue) and the differential quantum efficiency (DQE) (yellow) normalized by the Manley–Rowe (MR) limit at threshold vs. pressure for both inversions. The refilling inversion is both higher power and higher efficiency, with a modeled DQE that can reach 64%.

DQE is smaller than the refilling transition (which can reach as high as 64%). We also obtain the total quantum efficiency (QE), defined as

$$\eta_t = \frac{P_{\text{out}}}{P_{\text{pump}}} / \frac{\nu_{\text{out}}}{\nu_{\text{pump}}} \quad (2.49)$$

which is theoretically bounded by 100% from the Manley–Rowe limit [31]: the highest achievable power conversion efficiency is the ratio of output and pump frequencies. Our computed QE can be as high as 29% at 350 mTorr for the refilling transition and, as explained in the following section, can increase to 39% in an optimized cavity. As shown in Fig. 2-12, both QE values are considerably larger than those attained in previous commercial OPFIR lasers.

The remarkably high QE and DQE are an unexpected benefit of high pressure operation, especially for the refilling transition. The model indicates that as pressure increases, T_v also increases as more of the pumped molecules are collisionally trans-

ferred from v_3 to v_Σ and are therefore removed from the v_0 and v_3 A-type thermal pools that quench the refilling and direct inversions, respectively. DQE measures the likelihood that each additional pump photon just above threshold produces an additional terahertz photon, and the high DQEs seen at the highest operational pressures mean that both inversions are increasingly efficient as bottlenecking traps molecules in higher vibrational levels. In other words, below threshold most pumped molecules are quickly lost from the levels associated with the inversions due to rapid collisional thermalization, but just above threshold for a given pressure, sufficient collisional redistribution and equilibration of population has been achieved that additional pump photons simply add to the strength of the inversions. This is particularly true for the refilling transition, where the inversion with $L+1$ is produced as the pump laser removes molecules from L . The efficiency of the direct transition is lower and less sensitive to pressure because the pumped molecules placed in U are quickly removed by collisional processes. Consequently, the model indicates that it is the refilling transitions, not the direct transitions typically used in traditional OPFIR lasers, that are most attractive for compact, high pressure, efficient OPFIR lasers.

We can also

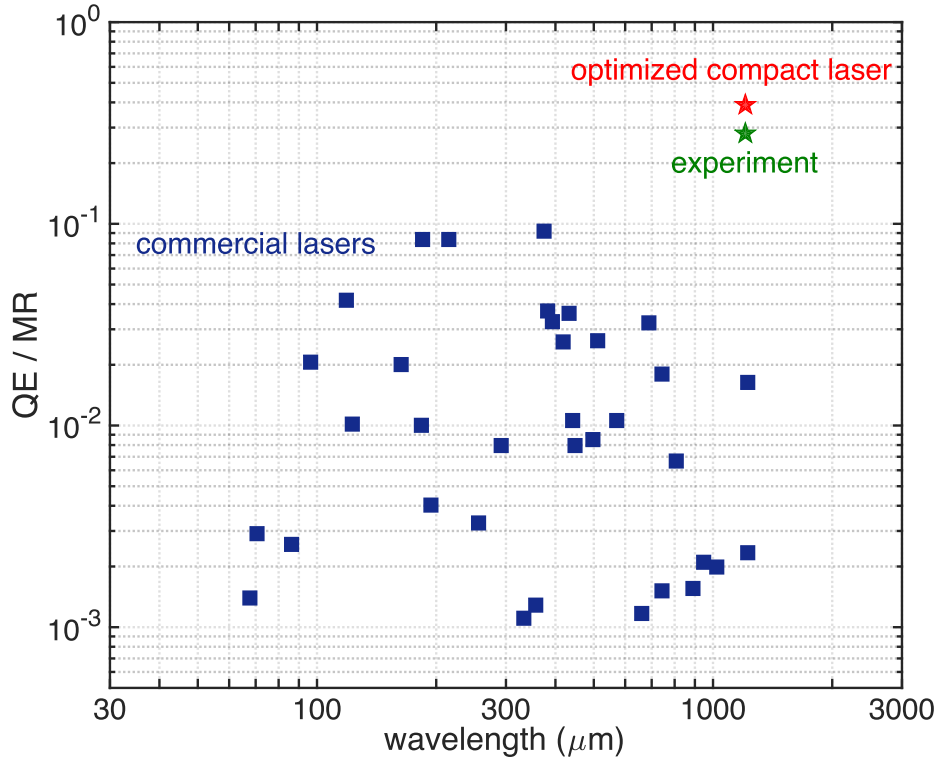


Figure 2-12: Total quantum efficiency [31] ($QE = \text{THz power out} / \text{IR power in}$) of commercial OPFIR lasers [36] and our compact OPFIR laser, normalized by the Manley–Rowe (MR) limit [31] on QE. Our experimentally demonstrated laser achieves a QE that is 29% of the MR limit (29% of 0.8%) which improves to 39% after cavity optimization. Both are $10\times$ better than the best commercial laser at the same frequency (0.25THz, or 1.2mm wavelength), while being $1000\times$ smaller—in fact, we show theoretically that this efficiency boost is mainly due to the fact that our cavity is so much smaller.

2.7 Cavity optimization

With the full understanding of the lasing physics at all pressures, we can finally explore and optimize the cavity geometry to maximize the THz power for compact OPFIR lasers. In particular, we consider the choice of cavity length and radius. Performing parameter variation with our model indicates that output power is maximized by a cavity length of roughly $1/2\alpha_p$, where α_p is the average pump absorption coefficient as discussed in Section 2.3.2, so here we define

$$L_o = \frac{1}{2\alpha_p} \quad (2.50)$$

to be the “optimal” cavity length. Fortunately, operating with this cavity length also ensures the validity of our z -averaged pump-intensity approximation, since L_o is several times smaller than the length where this approximation begins to fail due to nonuniform pump intensity. Calculating L_o is nontrivial because α_p itself depends on cavity length, so L_o must be obtained by a self-consistent nonlinear search.

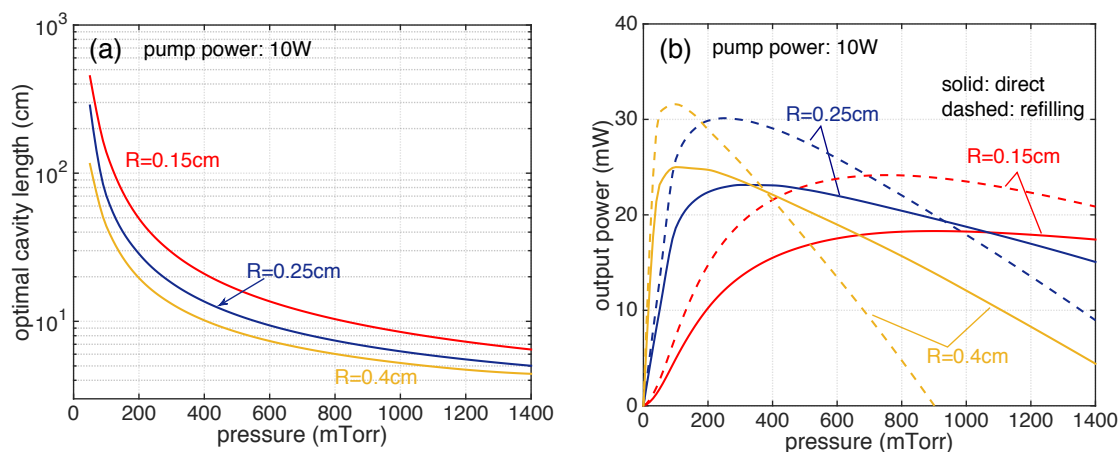


Figure 2-13: Theoretical predictions of (a) the roughly optimal cavity length for various radii and (b) the optimized laser power, both as a function of pressure for an input pump power of 10W. The cavity length is optimized to equal half the decay length of the pump beam. The output power (b) is shown for the optimal cavity length at each pressure and radius so that each data point is a separate cavity design. The peak efficiency is increased from 29% of Manley–Rowe in the experimental cavity to 39%, but more importantly this optimization allows efficient operation at a wider range of high pressures and hence in smaller cavities.

Figure 2-13(a) shows the optimal cavity length as a function of pressure with three different radii $R = 0.15\text{cm}$, 0.25cm , and 0.4cm , with pump power set at 10W . Because pump absorption increases with increasing pressure, we can see that higher pressures favor shorter cavities. The increase in optimal cavity length with decreasing cavity diameter derives from the increasing pump intensity, the associated increase in AC-Stark broadening and spectral-hole burning, and the increasing saturation of the pumped $L \rightarrow U$ transition for a given input pump power. Given that our cavity length was maintained at approximately 14.3 cm for all our measurements, the model indicates that the experimental drop in OPFIR power with increasing pressure is caused in part by excess cavity length and incomplete pumping of the entire volume.

Another design improvement can be achieved by placing the front pinhole at an optimized position: one chooses the pinhole location to increase the output flux of the lasing mode, which increases both the output power and the efficiency by decreasing the fraction of power lost to Ohmic absorption. For example, the TE_{01} mode [35] has a maximum flux intensity around $r = 0.48 R$, so an off-center pinhole will achieve larger lasing power, as shown schematically in Fig. 2-2(a). We compute the effect of the pinhole location by calculating the TE_{01} flux through the hole in the Appendix C.

With the input pump power set at 10W , the predicted output power for cavities of optimized length and pinhole position is shown in Fig. 2-13(b). Comparison with Fig. 2-6 indicates how severely the high-pressure lasing is hampered by excess cavity length. For optimized cavities, the maximum output power can reach 31mW , which is 39% of the Manley–Rowe limit. Cavities with a larger radius of $R = 0.4\text{cm}$ can achieve slightly higher output power at low pressures (around 100 mTorr). However, low pressure indicates longer cavity length (around 50cm) from Fig. 2-13(a). In contrast, 0.15cm diameter cavities shorter than 20cm can generate output power about 25% of the Manley–Rowe limit in a wide range of pressure above 400 mTorr . This requirement for widely adjustable cavity lengths is in stark contrast to traditional fixed geometry OPFIR lasers, typically 10cm in diameter and 1 meter in length [36]. Our analysis explains why these huge cavities are inefficient, can only operate at very low pressures, and may not be long enough!

Chapter 3

Quantum Cascade Laser Pumped Molecular Lasers¹

3.1 Introduction

Gas-phase OPFIR lasers historically used a line-tunable carbon-dioxide (CO_2) laser to excite a specific rotational-vibrational transition in a specific molecular gas to create a rotational population inversion within a tunable cavity. For example in Chapter 2, the coincidence between the 9P(32) line of the CO_2 laser excited the $R_3(4)$ ro-vibrational transition in $^{13}\text{CH}_3\text{F}$ and produced the terahertz rotational transition $J = 5 \rightarrow 4$. However, these lasers required a large CO_2 laser with high-voltage power supply. Moreover, they were not frequency-tunable, requiring the laser gas and CO_2 laser line to be changed each time a new frequency was needed.

In this chapter, we reintroduce the optically-pumped terahertz lasers (OPTLs) as compact, broadly tunable, and ultrabright sources of terahertz radiation. Compactness and frequency-tunability derive from three innovations: the advent of quantum cascade lasers (QCLs)[25–27] which allows a single IR source to excite any ro-vibrational transition of almost any molecule, the development of a comprehensive

¹This chapter is based on a manuscript submitted for publication, with co-authors Paul Chevalier (Harvard), Arman Armizhan (Harvard), Marco Piccardo (Harvard), Steven G. Johnson (MIT), Federico Capasso (Harvard), and Henry O. Everitt (U.S. Army CCDC Aviation & Missile Center, Duke University).

theory of OPTL operation as shown in Chapter 2, and our discovery that OPTLs are most efficient in small-volume cavities. The combination of the QCL and the compact OPTL can thereby produce a broadly tunable source that can easily fit in a shoebox. Moreover, these OPTLs are extremely bright sources defined by their brightness temperatures $T_b = Ic^2/(2k\nu_{\text{THz}}^2\Delta\nu) > 10^{14}$ K estimated by a typical laser radiance with Boltzmann constant k , intensity $I = 1 \text{ mW}\cdot\text{cm}^{-2}\cdot\text{sr}^{-1}$, and linewidth $\Delta\nu = 1 \text{ kHz}$.

3.1.1 QCL-pumped molecular laser (QPML)

The principle of the QCL-pumped molecular laser operation is shown in Fig. 3-11. The optical pumping of any molecular ro-vibrational transition $J_L \rightarrow J_U$ by a QCL tuned to the coincident frequency promotes molecules into a virtually empty excited vibrational level. Thus, sufficient pumping of J_U by the QCL can invert the rotational transition $J_U \rightarrow J_U - 1$ and induce the “direct” transition to lase. The frequency of the laser is approximately

$$\nu = 2BJ_U \quad (3.1)$$

where B is the rotational constant of the molecule. The rotational quantum number J_U is selected by the type of ro-vibrational transition excited by the QCL. As mentioned in previous chapters, for P -, Q -, and R -branch transitions, $J_U = J_L - 1$, J_L , and $J_L + 1$, respectively. With sufficient QCL power, it is even possible to induce the “refilling” transition $J_L + 1 \rightarrow J_L$ to lase as well, effectively doubling the number of laser lines for a given molecular gas.

In fact, QPML is a universal concept: any molecule with a permanent dipole moment and a vapor pressure can be made to lase if a QCL can be precisely tuned across the IR band of the molecule, and its tuning range is simply determined by the span of its rotational spectrum. In this chapter, we first study a QPML using N_2O as the gain molecule by both experiment and numerical modeling to demonstrate the compactness and broad frequency-tunability. Our model is able to constrain

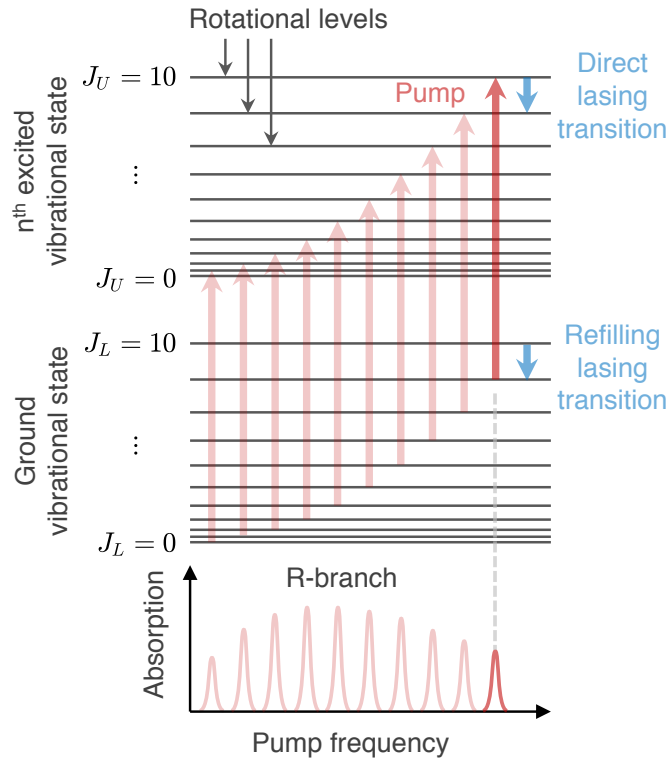


Figure 3-1: Universality of the QCL pumped terahertz gas laser: Diagram showing the different rotational levels of a molecule for both the ground and excited vibrational states. The red arrows show various R-branch transitions between rotational levels J_L and J_U responsible for the ro-vibrational absorption spectrum of the molecule as an illustration. The population of each rotational level of the ground vibrational state determines the magnitude of the IR pump absorption. The blue arrows indicate that the gas can lase at frequencies corresponding to an inversion between two rotational states in the excited (“direct”) or ground (“refilling”) vibrational level. The frequency of the laser emission is approximately $\nu = 2BJ_U$ for the R-branch transitions.

the unknown collisional cross sections, obtain excellent agreement with experimental measurements, and predict the optimal performance of the laser. Furthermore, a universal theory of QPML is developed to answer the general question of what molecular properties and cavity designs can improve the performance of QPMLs.

3.2 QCL-pumped N₂O laser

Figure 3-2 depicts the experimental setup of a QPML. The compact laser cavity is a 5 mm diameter, 15 cm long evacuated copper tube into which is inserted a copper rod rear reflector with a curved face that can be longitudinally scanned within the cavity until the cavity mode overlaps the gain profile. The output coupler is simply a pinhole in a flat front plate through which both the QCL and terahertz beams propagate. The IR beam is focused by a 15 cm focal length lens through a Brewster-angled ZnSe window to maximize power into the cavity (typically $\sim 85\%$), while the terahertz beam diffracts through the pinhole and is refocused by an off-axis parabolic mirror and a Teflon lens into a Schottky-diode detector or receiver operating in the frequency band of interest between 0.22 and 1.1 THz.

To illustrate the performance and tunability of a compact QPML, we chose nitrous oxide (N₂O), whose ν_3 vibrational band falls within the 2119–2342 cm⁻¹ tuning range of our 320-mW QCL (Daylight Solutions 41045-HHG). The spacings of the N₂O lasing transitions are $\sim 2B_{\text{N}_2\text{O}} = 25.1$ GHz. Frequency tuning was accomplished by monitoring the QCL signal transmitted through a 15 cm gas cell containing 50 mTorr of N₂O using a HgCdTe detector (Vigo PV-106). The QCL frequency was tuned by precise temperature control until molecular absorption minimized the transmitted IR power. To detect the QPML emission, we used various Virginia Diodes, Inc. room-temperature Schottky-diode detectors that operate between 0.22 and 1.1 THz.

We observed lasing for all 23 direct lasing transitions and 8 refilling transitions within 0.250–0.800 THz (J_L between 9 and 31) by exciting each R -branch ν_3 rovibrational transition over a QCL tuning range of 2231–2247 cm⁻¹ (see Fig. 3-3A for direct transitions and Fig. 3-3B for refilling transitions). Refilling transitions and direct transitions corresponding to the same J_L exhibited slightly different frequencies due to different rotational constants for the ground and excited states. Lower-frequency lasing could not be observed because it occurred too far below the cutoff frequency of the pinhole output coupler, suppressing radiation.

For most transitions, we measured the strength of the laser emission as a function

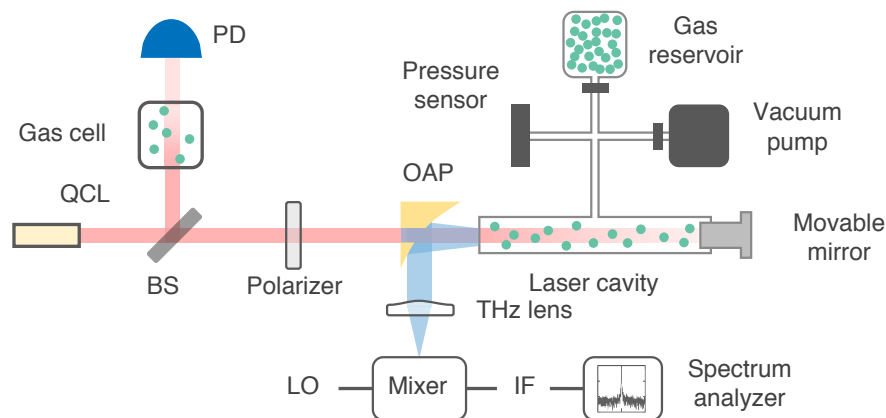


Figure 3-2: Experimental setup: light from a tunable QCL is tuned to pump a vibrational transition and create a rotational population inversion, thus realizing a QCL pumped molecular laser (QPML). Light from the QCL is deflected by a 90%–10% beam splitter (BS) and transmitted through a gas cell so that the QCL may be tuned into coincidence with the vibrational transition by minimizing the transmitted intensity measured using a photodiode (PD). Light is coupled into the laser cavity through a hole in an off-axis parabolic mirror (OAP), through a ZnSe window at Brewster’s angle, and through a pinhole coupler in the cavity. A vacuum pump, pressure sensor, and gas reservoir are used to set the pressure in both the laser cavity and the gas cell. The radiation emitted from the pinhole of the QPML is collected with the OAP, sent through a Teflon lens, and measured by a power meter, detector, or receiver, the latter of which uses a frequency-multiplied local oscillator (LO) mixed with the signal to produce the intermediate frequency (IF) measured by a spectrum analyzer. The pump power from the QCL is varied using a wire grid polarizer on a calcium fluoride substrate. The laser cavity is tuned into resonance with the lasing frequency by moving a copper mirror on a translation stage.

of pressure for maximum QCL pumping power, and in some cases we also measured the laser emission as a function of QCL pumping power as in Fig. 3-4A for $J_L = 14$. Figure 3-5B shows a more comprehensive measurement of the output THz power as a function of both gas pressure and QCL pump power for $J_L = 14$. By these measurements, we were able to obtain the threshold power and slope efficiency of many laser lines, providing critical information for ascertaining the molecular collisional cross sections needed in the theoretical model, particularly the dipole–dipole and gas kinetic thermalizing collisional cross sections.

We also used heterodyne receivers operating between 0.3 and 0.775 THz to measure the spectrum of these laser transitions (see Fig. 3-4B for the recovered line at

$\nu_{\text{THz}} = 373 \text{ GHz}$). The instantaneous linewidths were less than 1 kHz, but because of frequency jitter the effective linewidths were typically 3-6 kHz. Other measured lines are shown in Figs. 3-3 over a 200 kHz span. We were able to demonstrate frequency tuning of the laser across its full Doppler-broadened gain bandwidth by precisely adjusting the cavity length with a motorized micrometer, as witnessed by the broad feature (grey curve) in Fig. 3-4B showing the envelope of all the individual frequencies the laser was tuned to while keeping the pump laser at a constant power and frequency. Importantly, the QPML frequency was quite stable (routinely $< 10 \text{ kHz}$) while freely running, and it could be made even more stable through active frequency stabilization of the QCL[37] and the laser cavity [38].

Using these experimental measurements, our comprehensive theoretical model discussed in the following sections is able to fit the collisional cross sections and predict the optimal laser performance. Fig. 3-5A and Fig. 3-5B show an excellent agreement between the theoretical and measured output THz power for the case of $J_L=14$. The fit estimates the dipole–dipole collisional cross-section to be 35 \AA^2 , well within the expected range.

In the following, we start by a brief description of the modeling procedures adapted from Chapter 2. Then a comprehensive model is used to determine the most important while unknown collisional parameters, based on which more predictions on the laser performance are presented.

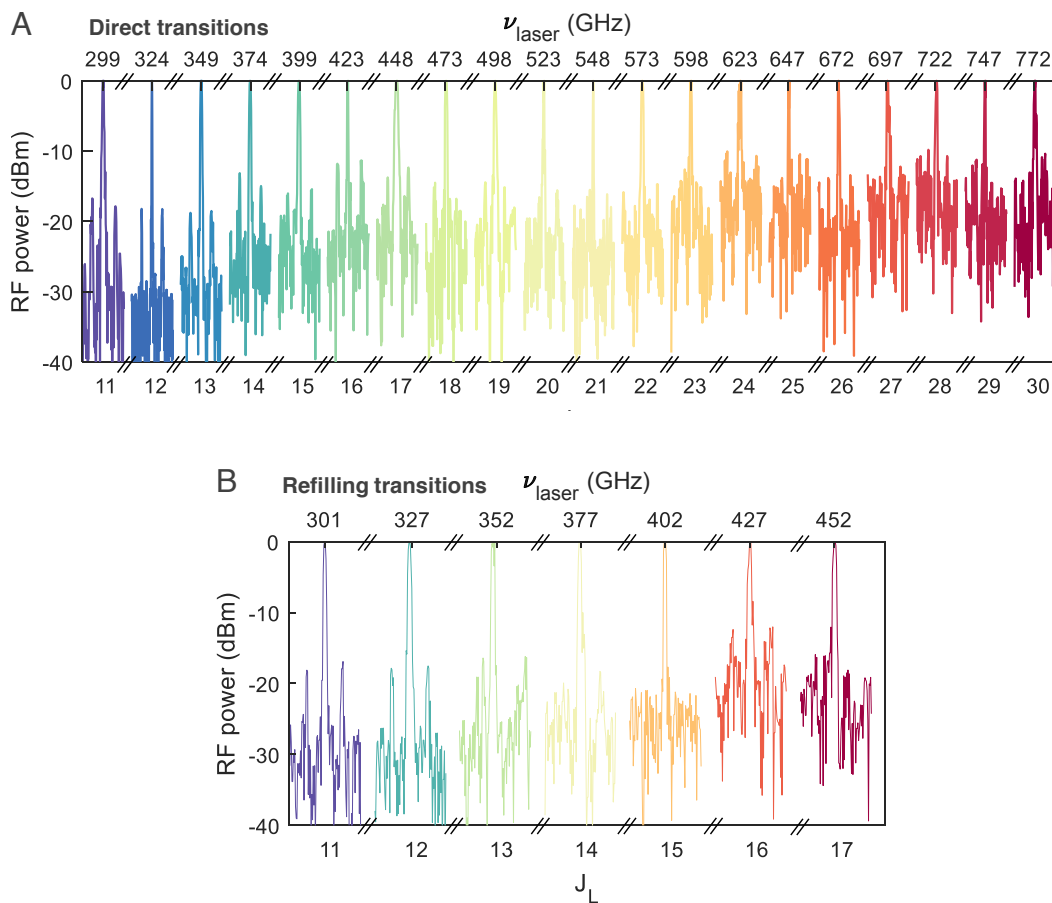


Figure 3-3: Tunability of the optically pumped N_2O laser: Emission spectra of the laser were measured as the QCL pump laser was tuned to different infrared transitions of N_2O . The top x-axis shows the measured emission frequency while the bottom x-axis shows the quantum number of the lower state of the pumped R-branch transition. The QCL power was maximal (up to 250 mW coupled in the cavity), and the pressure was 40 mTorr for direct transitions and 20 mTorr for refilling transitions. A: Measured spectra of direct transitions with J_L from 11 to 30. B: Measured spectra of refilling transitions with J_L from 11 to 17.

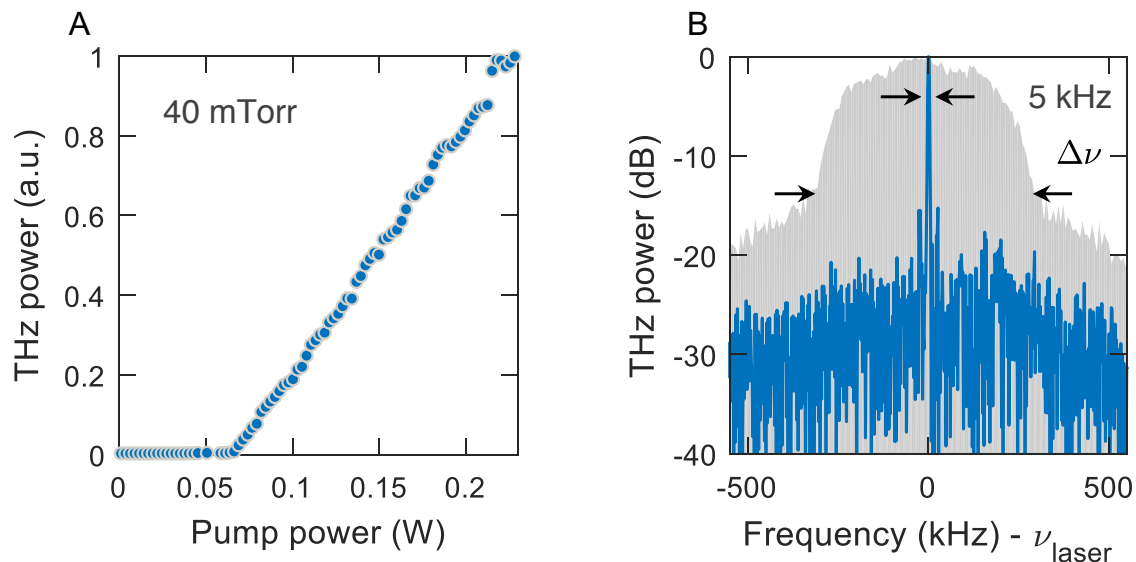


Figure 3-4: Experimental measurements: A: The output power of the N₂O QPML is plotted as a function of the IR pump power from the QCL, for which $P_{\text{THz}} = 70\text{ mW}$ and $\eta = 0.05\text{ mW/W}$ at 40 mTorr for the $J_U = 15 \rightarrow 14$ transition at 374 GHz. B: Emission spectra recorded for various mirror positions (broad grey feature) indicate the full tuning range of the QPML operating at this same transition. The central line is plotted (blue line) and shows a recovered linewidth of $\leq 5\text{ kHz}$ at 374 GHz.

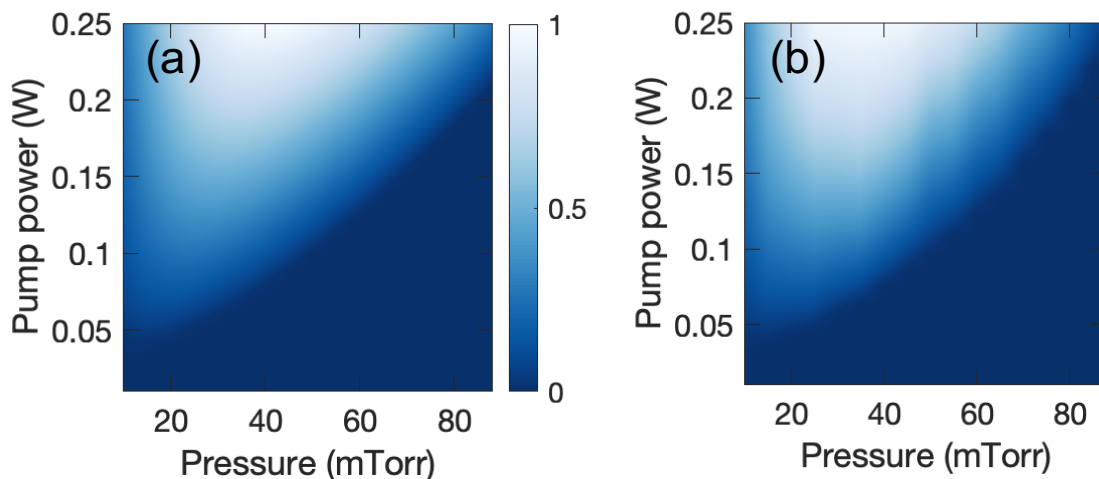


Figure 3-5: (A) Predicted and (B) measured QPML laser power as a function of gas pressure and QCL pump power for the same direct transition with $J_L = 14$.

3.3 Theoretical modeling of N₂O QPML

The theoretical model discussed in Chapter 2 is adapted to describe the lasing dynamics of the N₂O QPML. Different from the CH₃F molecule, N₂O is a linear molecule, making the modeling task much simpler. Its rotational levels are labeled by quantum number J with $2J + 1$ fold degeneracy. The QCL pumps population of J_L in the ground vibrational state v_0 into J_U in the excited state v_3 . Since N₂O doesn't have the K quantum number, the population fraction of level L is much larger than that of CH₃F. Therefore, the N₂O laser operates at much lower pressures typically under 100 mTorr. The low-pressure operation suppresses many collisional processes as well as the influence of high-lying vibrational levels. So the effective temperature model is unnecessary here. Additionally, there are no A/E-type degeneracy in N₂O, and neither are there V-swap collisional processes. The dominant collisional processes are the dipole–dipole collisions, SPT processes, and molecule–wall collisions. Note that in between v_0 and v_3 are sandwiched 5 vibrational states, which enhances the ro-vibrational relaxation process. In the following modeling, we only present examples of the R branch with $J_U = J_L + 1$ for consistency with the experiments.

To describe the pump process, the rate-equation model includes rotational levels $J = 0$ to $J_L + 7$ and the 10 lowest energy vibrational levels. For the *rotational* level, the rate equation is

$$\begin{aligned} \frac{dN_\ell(v, \mathbf{r}, t)}{dt} = & [\sum_{\ell'=\ell\pm 1} -\gamma_{\ell\ell'} N_\ell(v, \mathbf{r}, t) + \gamma_{\ell'\ell} N_{\ell'}(v, \mathbf{r}, t)] \\ & - \gamma_{\text{SPT}} N_\ell(v, \mathbf{r}, t) + R_{\text{pump}}(v, \mathbf{r}, t) + D\nabla^2 N_\ell(v, \mathbf{r}, t) \end{aligned} \quad (3.2)$$

where $N_\ell(v, \mathbf{r}, t)$ is the nonthermal population density for rotational level ℓ with axial velocity v along the pump beam direction, at position \mathbf{r} , and at time t . $\gamma_{\ell\ell'}$ is the dipole–dipole collisional transition rate. From the selection rules, ℓ' can only be $\ell \pm 1$. The transition rate is determined by $\gamma_{\ell\ell'} = n_{\text{tot}} \langle v_{\text{rel}} \rangle \sigma \rho_{\ell\ell'}$, where n_{tot} is the total molecular population density, $\langle v_{\text{rel}} \rangle$ is the thermally averaged relative velocity, $\rho_{\ell\ell'}$ is the appropriate branching ratio with a Boltzmann factor. These parameters can be evaluated following Chapter 2. σ is the collisional cross section for the transition.

As mentioned above, the dominant collision is the dipole–dipole collision, so that $\sigma \approx \sigma_{\text{DD}}$. In the second line of (3.2), $-\gamma_{\text{SPT}}N_\ell$ describes the thermalization transition of rotational level ℓ into its vibrational mode due to low energy collisions. The thermalization rate γ_{SPT} is computed with the collisional cross section σ_{SPT} . R_{pump} describes the pump transition thoroughly following the treatment discussed in the previous chapter. It includes inhomogeneous broadening from all velocity subclasses with Doppler effect, pressure broadening with HWHM equal to 4.0 MHz/Torr, and the multiple round-trips inside the cavity. The linewidth of the pump EC-QCL used in experiments is typically 1-10 MHz. At last, diffusion process is also included in (3.2).

Similarly, the rate equation for the *vibrational* level is

$$\begin{aligned} \frac{dN_p(v, \mathbf{r}, t)}{dt} = & [\sum_{p'=p\pm 1} -\gamma_{pp'}N_p(v, \mathbf{r}, t) + \gamma_{p'p}N_{p'}(v, \mathbf{r}, t)] \\ & + \sum_\ell \gamma_{\text{SPT}} \int dv N_\ell(v, \mathbf{r}, t) + D\nabla^2 N_p(v, \mathbf{r}, t) \end{aligned} \quad (3.3)$$

in which $\gamma_{pp'}$ is the transition rate between vibrational thermal pools $p \rightarrow p'$ and is assumed proportional to the gas kinetic cross section σ_{GK} and Boltzmann factor $\exp(-\Delta E_{pp'}/k_B T)$ where $\Delta E_{pp'}$ is the vibrational energy deficit between p and p' . The last two terms describe the thermalization from rotational levels to vibrational levels as well as diffusion.

Additionally, molecule–wall collision is modeled by a reaction boundary condition as discussed in Chapter 2, so that wall collision thermalizes the vibrational level and redistributes the molecules into all possible levels with a Boltzmann distribution at room temperature (300K). The ground vibrational state has the largest probability. Instead of time evolution, we obtain the steady state by setting $dN/dt = 0$. These nonlinear rate equations are discretized and solved numerically by fixed-point iteration with Anderson acceleration as discussed in Chapter 2. At each iteration step, the MUMPS direct solver is used for factorizing the sparse matrix [39].

Terahertz output power is obtained by matching the cavity loss α_{cell} with the THz gain. In particular, the cavity loss includes the ohmic loss α_{ohmic} and transmission loss α_{trans} through the front pinhole. Ohmic loss can be expressed analytically for

the modes of a hollow metal waveguide, which increases strongly with decreasing radius [35]. The transmission loss is estimated by $\alpha_{\text{trans}} = -\log(1 - T)/2L$ where T is the front window transmission coefficient. The gain coefficient is obtained by integrating contributions from all velocity subclasses.

3.3.1 Determination of σ_{DD} and other parameters

Unlike widely-studied CH_3F , whose collisional parameters are experimentally well known [16, 18], many collisional cross sections of N_2O are unknown, such as the most important σ_{DD} (dipole–dipole collisions). However, thanks to our full laser model, we can use the experimental results to extract the key unknowns by a fitting procedure. In particular, we use experimental fits to determine the dipole–dipole cross section σ_{DD} , the cavity loss (since the alignment and other geometric factors were imperfectly known for our cavity), and the QCL linewidth. We also considered whether to fit the SPT collisional cross section σ_{SPT} , but this parameter turned out to have little influence on the results within a reasonable range and so we simply set it to match the gas kinetic cross section. Once these parameters were obtained, we could then proceed to use the model to predict other lasing behaviors and to identify the optimal cavity and operating regime.

Fig. 3-6 shows the threshold power for direct lasing as a function of pressure for both experimental measurements (blue circles) and theoretical modeling (dashed lines) with different dipole–dipole cross sections $\sigma_{\text{DD}} = 25\text{\AA}^2$, 35\AA^2 , and 45\AA^2 . A reasonable range for σ_{DD} can be estimated by assuming $\sigma_{\text{DD}} \propto \mu$. Considering $\mu_{\text{N}_2\text{O}} = 0.17$ D, $\mu_{\text{CH}_3\text{F}} = 1.8$ D, and $\sigma_{\text{DD}}^{\text{CH}_3\text{F}} = 320\text{\AA}^2$, we can evaluate $\sigma_{\text{DD}}^{\text{N}_2\text{O}} \approx \sigma_{\text{DD}}^{\text{CH}_3\text{F}} \frac{\mu_{\text{N}_2\text{O}}}{\mu_{\text{CH}_3\text{F}}} = 30\text{\AA}^2$. Fig. 3-6 shows $\sigma_{\text{DD}} = 35\text{\AA}^2$ has the best agreement with experiments, which is within the reasonable range. The fitted cavity loss is 0.3 m^{-1} , which is about 5 times larger than an ideal cylindrical cavity with TE_{01} mode. In principle, cavity loss can be computed with the exact cavity geometry and cavity mode. However, our current cavity has poor alignment using a concave back mirror with focal length about 2-3 cm, which easily couples the lasing mode to other cavity modes, in particular with high frequencies. In addition, the front pinhole coupler is tapered from the 1 mm diameter

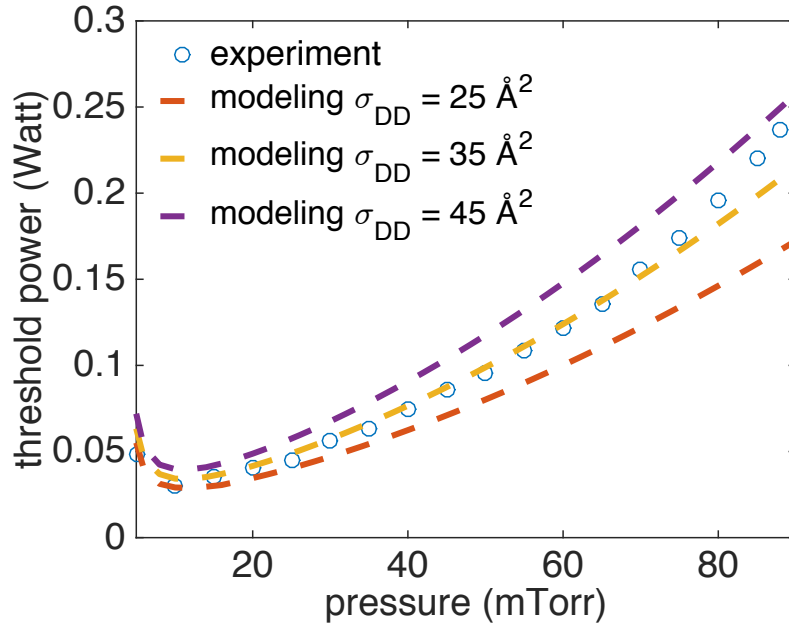


Figure 3-6: Threshold power for direct lasing as a function of pressure for both experimental measurements (blue circles) and theoretical modeling (dashed lines) with different values of $\sigma_{DD} = 25^2, 35^2, 45^2$. $J_L = 14$ is pumped rotational level. In the model, cavity loss is 0.3m^{-1} . The results indicate the dipole-dipole cross section of N_2O is 35^2 .

exit to the 5 mm diameter cavity, and this taper also contributes to mode mixing as well as suppression of long wavelength emission below cutoff. QCL linewidth is fitted as 2 MHz to match Fig. 3-5B, a value that is well within the range previously reported for EC-QCLs [40]. With these fitted parameters, full agreement between theory and experiments for the output THz power as a function of gas pressure and pump power is obtained for $J_L = 14$, as shown in Fig. 3-5.

Using the obtained collisional parameters, the theory-experiment match for $J_L = 31$ is also presented in Fig. 3-7. The agreement between theoretical modeling and experiments confirms the correctness of the deduced collisional cross sections. Only the cavity loss had to be adjusted, increased to 0.46 m^{-1} (due to the near doubling of the THz frequency) to obtain good agreement. A frequency-dependent cavity loss is expected because of the increasing number of modes above cutoff at higher frequencies, coupled more easily to the lasing mode by the concave back plunger in our cavity with increasing J_L and lasing frequency. There is potential for improving

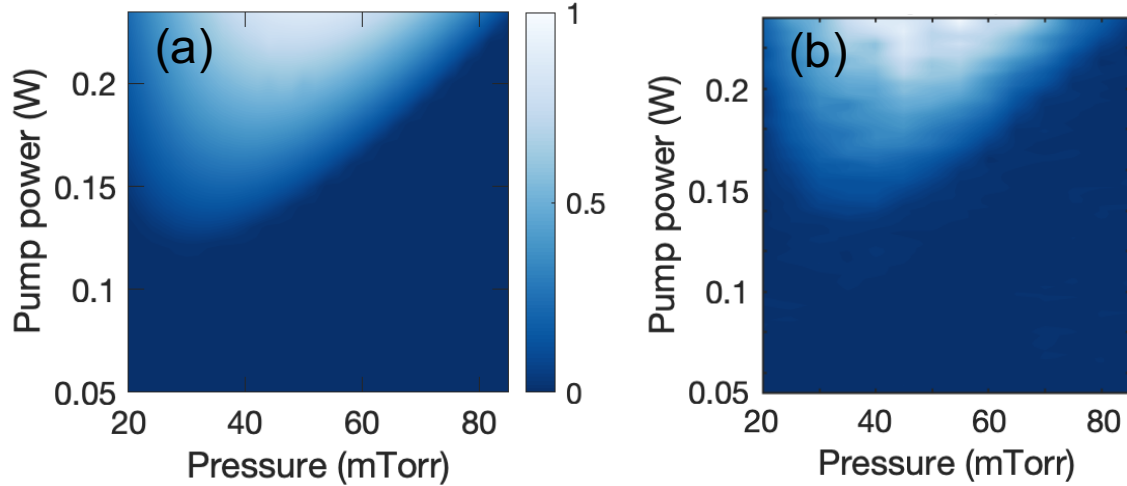


Figure 3-7: Contour plot of the THz output power from direct lasing transition as a function of pressure and pump power for $J_L = 31$. The theoretical prediction (left) matches the experimental measurement (right) very well with previously obtained dipole–dipole collisional cross section $\sigma_{DD} = 35 \text{ \AA}^2$, and QCL linewidth as 2 MHz. The cavity loss is fitted as 0.46 m^{-1} .

the cavity design with a different geometry mirror or metasurface.

3.3.2 More predictions and discussion

With the confidence in the fitted collisional parameters, we’ll use the model to make more predictions on the QPML performance for different pressures and different lines.

Figure 3-8 shows the predicted laser power for each transition at its optimal gas pressure. We find that the direct lasing transition with maximum power occurs not for $J_L = 15$, where n_{J_L} is largest, but for $J_L = 28$ because of the Manley–Rowe effect. Of course, the output power decreases for higher J_L due to the limited population. An emitted power of 0.07 mW was predicted for the $J_L = 14$, $\nu_{\text{THz}} = 374 \text{ GHz}$ transition in a perfectly aligned single mode cavity. Although we measured only 0.01 mW, our power measurements underestimate the emitted power for several reasons, including imperfect cavity alignment, competition among several cavity modes above the lasing threshold, severe diffraction and low transmission of the terahertz beam emitted through the 1 mm diameter output coupler, absorption and reflection by the ZnSe Brewster window and Teflon lens, and use of the power meter at the edge of its

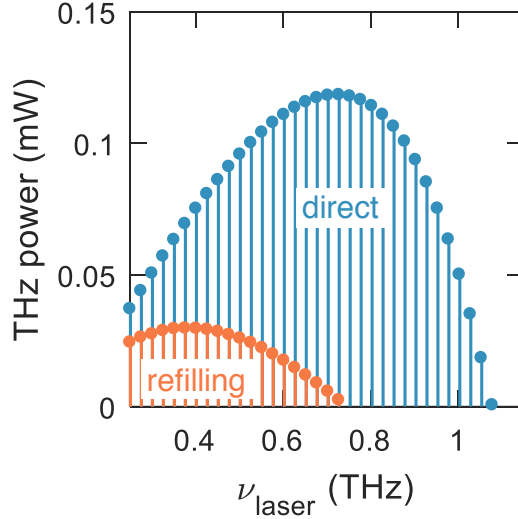


Figure 3-8: THz output power vs pressure with $J_L = 6$ to $J_L = 41$ for both direct and refilling lasing.

calibrated range.

Pump threshold power increases with pressure, as shown in Fig. 3-6, due to the linearly increasing thermal population that must be overcome as pressure increases. So a QPML lases more easily at lower pressures. But this doesn't imply higher powers at lower pressures, because only a limited fraction of the population can be pumped. The optimal pressure with the highest output power occurs in between, as shown in Fig. 3-9 for both direct and refilling transition with $J_L = 6$ (~ 175 GHz) to $J_L = 41$ (~ 1.05 THz). Lasing from direct inversion operates at higher pressures and with much more output power than refilling inversion because refilling lasing has to overcome much greater thermal population in the ground vibrational state.

Figure 3-10 shows the threshold power as a function of pressure for different J 's. $J_L = 30$ has the lowest threshold across all pressures. This agrees with the observation in Fig. 3-8 that $J_L = 28$ (close to 30) is predicted to produce the maximum power, even though the maximum population occurs at $J_L = 15$, because of the Manley-Rowe effect. A rotational level with a larger or smaller J_L has smaller population available to be pumped and therefore produces smaller output power with a higher threshold. For $J_L = 40$, the threshold power increases with decreasing pressure below 20 mTorr. This is also an effect of very limited population available to be pumped

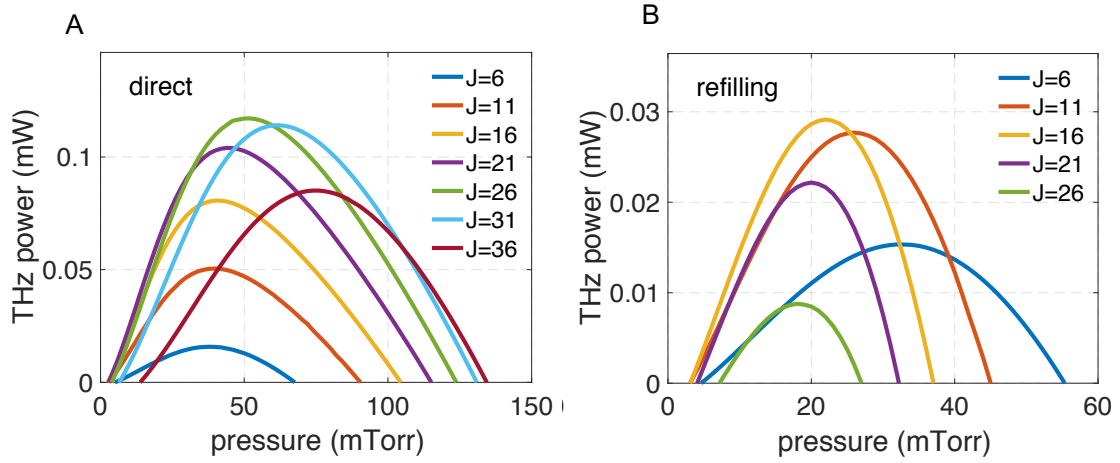


Figure 3-9: THz output power vs pressure with $J_L = 6$ to $J_L = 41$ for both direct and refilling lasing.

considering the population fraction is only $n_{J=40} = 0.54\%$.

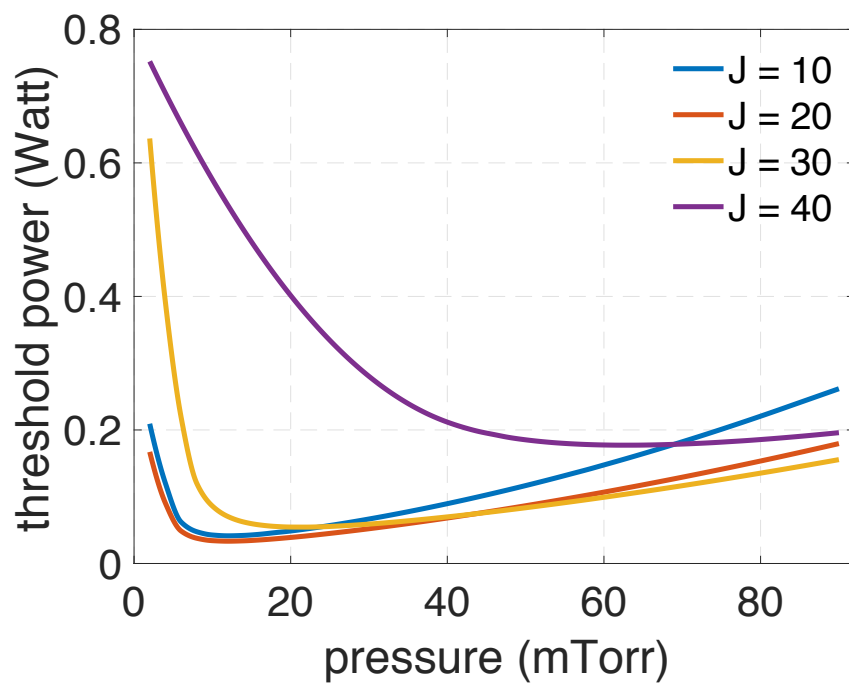


Figure 3-10: Pump threshold power as a function of pressure for $J = 10, 20, 30, 40$. The cavity loss is assumed to be 0.3m^{-1} for all cases.

3.4 Universal theory of QPML

As mentioned previously, a frequency-tunable QCL-pumped terahertz laser is achievable for many molecules. Besides N₂O, QPML has also been reported on three NH₃ transitions [41, 42], and virtually any rotational transition can be induced to lase in this manner.

Figure 3-11 illustrates the tuning range for several simple molecules (OCS, N₂O, CH₃F, HCN, CO). The spacing of the laser lines is twice the principal rotational constant B , which is inversely proportional to the principal moment of inertia of the molecule for the vibrational level excited by the QCL [43, 44]. Thus a low moment of inertia molecule like CO has sparser spacing, a broader tuning range, and a peak emission intensity at a high frequency, while a higher moment of inertia molecule like OCS has a denser spacing, a narrower tuning range, and a peak at a lower frequency. The number of available transitions increases as the molecular symmetry decreases and molecular mass increases. If a laser is needed at a specific frequency, the appropriate molecular gas may be identified by consulting a catalog of such transitions [45–47].

For a given QCL pump power, the terahertz power achievable by this room temperature laser depends on several factors. To ascertain the potential of a given molecular gas as a QPML, we consider the very low-pressure regime for which molecular collisions with the chamber walls occur more frequently than any inter-molecular collisions. When the QCL linewidth is much less than the ~ 50 – 150 MHz Doppler width of the IR molecular transition, a simple expression (derived in the next section) gives the QPML laser power

$$P_{\text{THz}} = \frac{T}{4} \left(\frac{\nu_{\text{THz}}}{\nu_{\text{IR}}} \right) \left(\frac{\alpha_{\text{IR}}}{\alpha_{\text{cell}}} \right) [P_{\text{QCL}} - P_{\text{th}}] = \eta [P_{\text{QCL}} - P_{\text{th}}] \quad (3.4)$$

at frequency ν_{THz} and identifies the essential parameters on which the laser power depends. Here, α_{IR} is the IR absorption coefficient of the gas molecule at the frequency ν_{IR} to which the QCL is tuned, α_{cell} captures the losses of the cavity, P_{QCL} is the QCL pumping power and T is the front window transmission coefficient for the THz output. For $\nu_{\text{THz}} > c/2r_0$, $T \approx (r_0/R_{\text{cell}})^2$, where R_{cell} is the cavity radius and r_0 is the radius

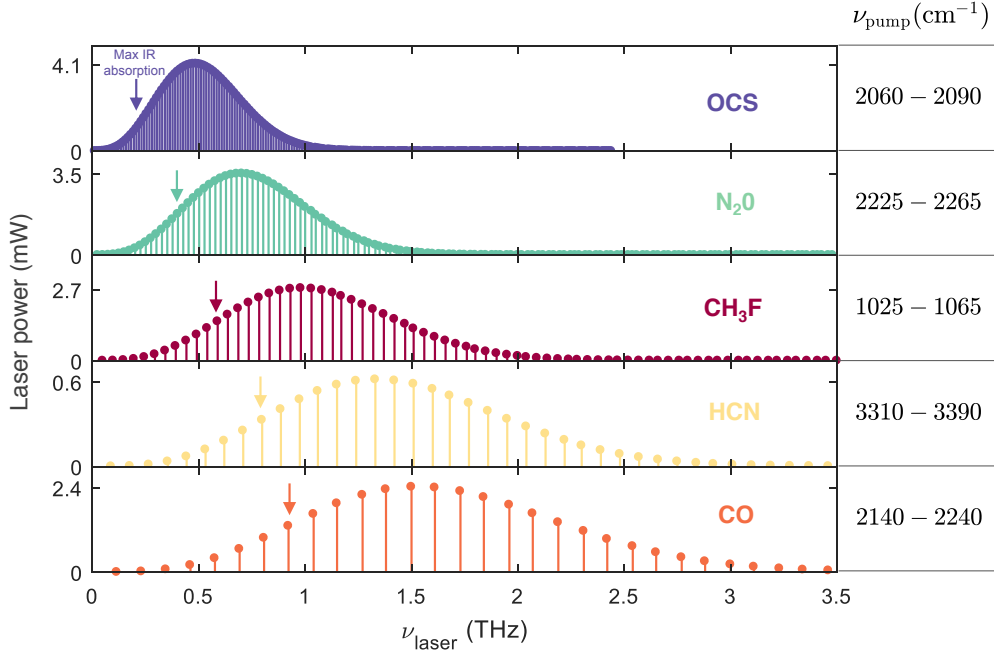


Figure 3-11: Plot showing the QPML tuning range and estimated power from direct transitions for 10 mTorr of various molecular gases in a compact cylindrical cavity pumped by a 250 mW QCL: Carbonyl sulfide (OCS), Nitrous oxide (N₂O), Methyl fluoride (CH₃F), Hydrogen cyanide (HCN), and Carbon monoxide (CO). The arrows indicate the J_L for which the rotational population is largest, illustrating how the Manley–Rowe effect skews the peak power to higher frequency. Also listed is the QCL tuning range required to pump the associated R-branch transitions.

of the output coupler. But if the lasing frequency is low, T depends sensitively on the pinhole thickness. Combined, the factors before the square bracket in (3.4) constitute the power efficiency η of the QPML. The lasing threshold

$$P_{\text{th}} = \frac{h^2 \nu_{\text{IR}}}{4\pi \alpha_{\text{IR}}} \alpha_{\text{cell}} R_{\text{cell}} \frac{u^2}{|\langle J_U - 1 | \mu | J_U \rangle|^2} \quad (3.5)$$

depends on many of the same parameters, as well as the absolute molecular velocity u and the transition dipole matrix element of the rotational transition $\langle J_U - 1 | \mu | J_U \rangle$. As expected, the threshold increases with increasing cavity loss, but the dependence of P_{th} on cell radius is more subtle because of the strong increase of α_{cell} with decreasing R_{cell} due to Ohmic loss [35]. The threshold decreases for increasing dipole moment and

Molecule	J_L (peak)	ν_{THz} (THz)	P_{THz} (mW)	P_{th} (mW)	η (mW/W)	μ (D)	ν_{IR} (cm^{-1})	α_{IR} (m^{-1})
CH ₃ F	11	0.605	1.49	0.10	5.97	1.85	1067.400	1.9
OCS	22	0.280	2.13	0.12	8.52	0.72	2070.859	11.3
NH ₃	3	1.073	6.16	0.15	24.66	1.46	967.346	4.0
HCN	8	0.797	0.33	0.29	1.32	2.98	1438.666	0.4
H ₂ CO	9	0.777	0.35	0.37	1.40	2.33	1768.470	0.6
N ₂ O	15	0.400	1.78	5.19	7.26	0.17	2236.223	7.3
CH ₃ ³⁵ Cl	15	0.416	0.01	5.63	0.05	1.90	1459.545	0.03
CO	7	0.922	1.31	41.3	6.27	0.12	2172.759	2.7

Table 3.1: Predicted QPML power and QCL threshold pump power for the strongest IR ro-vibrational transition of eight candidate laser molecules. Assumes a 0.25W QCL pumping through a 1 mm diameter pinhole output coupler into a 5 mm diameter cylindrical laser cavity (loss = 0.06 m^{-1}) containing 10 mTorr of the molecular gas.

decreasing ν_{IR} , indicating that terahertz lasing is favored for strongly polar molecules with low frequency vibrational modes.

Importantly, Eq. 3.4 shows that the maximum power achievable by the QPML, often known as the Manley–Rowe limit[48], is determined by the ratio of the terahertz laser and IR pump frequencies $\nu_{\text{THz}}/\nu_{\text{IR}}$. Any vibrational band may be pumped by the QCL, but this Manley–Rowe limit[48] also recommends low frequency vibrational modes and long-wavelength QCLs. Currently, more powerful QCLs are available at higher frequencies, so the selection of which vibrational mode to excite must be determined by its absorption strength, the Manley–Rowe factor, and the available QCL power.

Moreover, the Manley–Rowe factor indicates that the maximum power of the QPML grows with increasing laser frequency for a given QCL and vibrational band, in tremendous contrast with electronic sources. This Manley–Rowe effect is tempered by the pressure-dependent population n_{J_L} , manifested in the IR absorption term α_{IR} , available for the QCL to excite. One may simply look at the IR spectrum of a molecule to estimate how the power of the corresponding terahertz laser will depend on J_L . Fig. 3-11 plots the predicted power from Eq. 3.4, which is proportional to the product of α_{IR} and $\nu_{\text{THz}}/\nu_{\text{IR}}$ and confirms that the peak power occurs not for the J_L where n_{J_L} is maximum but at a higher J_L because of the Manley–Rowe effect.

The simple model in Eqs. 3.4-3.5 captures the molecular and cavity parameters essential for ascertaining how a given molecular gas will perform as a QCL-pumped terahertz laser. Table 3.1 summarizes these behaviors for eight candidate polar molecules, sorted by threshold pump power. The oblate symmetric top NH_3 has recently been reported as a low threshold QCL-pumped laser[41, 42], but the simple model reveals that CH_3F and OCS have even lower thresholds. The high ν_{THz} of NH_3 coupled with its low ν_{IR} and the high α_{IR} , combine to produce the highest power efficiency and largest output power; however, the linear (OCS , HCN , N_2O , CO) and prolate (CH_3F , H_2CO , $\text{CH}_3^{35}\text{Cl}$) molecules offer much greater tunability, in both range and spacing, throughout the terahertz spectral region.

Because the model in Eqs. 3.4-3.5 is only valid at very low pressures, there is no collisional quenching of the laser inversion, and P_{THz} is predicted to increase linearly with increasing pressure (through α_{IR}). Of course, this best-case approximation fails at higher pressures when inter-molecular dipole–dipole, rotational-state randomizing, and velocity-randomizing collisions dominate the laser performance and quench the inversion in a manner that depends on collision cross sections that may not be known. To thoroughly study the lasing behaviors, our comprehensive numerical model can be used to predict the performance of QPMLs as a function of P_{QCL} and pressure.

In summary, we demonstrated the universal concept of broadly tunable molecular lasers as a promising compact terahertz source, as more powerful single-mode[49, 50], frequency stabilized QCLs are being developed, especially at longer wavelengths. To improve portability, vacuum systems may be eliminated by placing within a confocal cavity a sealed waveguide containing a given laser gas at its optimal pressure. In addition to “coarse” line-by-line tuning of the QPML, “fine” tuning for a given line may be accomplished through Stark tuning techniques[51], which may also be useful for frequency modulating the QPML as a local oscillator for spectroscopy, radar, or astronomical sensing. Finally, a tailored metasurface[52] could replace the pinhole output coupler to optimize the competing requirements for low loss IR pumping and high terahertz reflectivity (98%) for optimal laser power while generating the desired spatial mode and minimizing mode competition.

3.5 Analytical derivation of QPML theory

In a simplified three-level model as shown in Fig. 3-12, ground level 1 is pumped with rate R_{pump} into level 2, followed by dipole-dipole collisions between level 2 and level 3, as well as molecule-wall collisions. THz lasing occurs between level 2 and 3. Similar three-level models can be found in previous works [53], but they typically did not include wall collisions. In this section, analytical derivations of the population inversion, gain coefficient, pump threshold, and the THz output power in the low-pressure limit are presented.

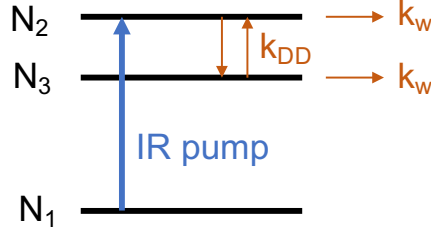


Figure 3-12: Schematics of a simplified three-level model for analytical derivations.

3.5.1 Pump threshold

Assuming molecular relaxation is dominated by molecule-wall collisions with rate k_w and intermolecular dipole-dipole collisions with rate k_{DD} , the rate equations for N_2 and N_3 are

$$\begin{aligned}\frac{dN_2}{dt} &= R_{\text{pump}} - N_2(k_{\text{DD}} + k_w) + N_3k_{\text{DD}}, \\ \frac{dN_3}{dt} &= N_2k_{\text{DD}} - N_3(k_{\text{DD}} + k_w)\end{aligned}$$

At steady state, $dN_2/dt = dN_3/dt = 0$, and the population inversion is obtained as

$$\Delta N = N_2 - N_3 = \frac{R_{\text{pump}}}{2k_{\text{DD}} + k_w}. \quad (3.6)$$

The pump rate can be approximated as

$$R_{\text{pump}} = \frac{P_{\text{QCL}}(\alpha_{\text{IR}}L)}{h\nu_{\text{IR}}} \frac{1}{\pi R_{\text{cell}}^2 L} = \frac{\alpha_{\text{IR}}P_{\text{QCL}}}{\pi R_{\text{cell}}^2 h\nu_{\text{IR}}} \quad (3.7)$$

in which α_{IR} is the infrared absorption coefficient of the gain medium, and R_{cell} and L are the cavity radius and length, respectively. The pump power absorbed by the gain medium is approximated as $P_{\text{QCL}}(\alpha_{\text{IR}}L)$.

The unsaturated gain coefficient is [31]

$$\gamma_0 = \sigma_l \Delta N = \left[\frac{\lambda^2}{8\pi^2 \Delta\nu t_{\text{sp}}} \right] \Delta N$$

where σ_l is the cross section for the lasing transition, the spontaneous emission lifetime is $t_{\text{sp}} = 3h\epsilon_0\lambda^3/16\pi^3\mu_{ij}^2$ where $\mu_{ij}^2 = |\langle i|\mu|j\rangle|^2$ is the dipole matrix element, and $\Delta\nu$ is the half width of the gain profile approximated as the Doppler broadening half width $\Delta\nu \approx \Delta\nu_D \approx u/\lambda$ where u is the average relative speed between molecules. Then we obtain

$$\gamma_0 = \left(\frac{2}{3h^2\epsilon_0} \right) \left(\frac{\mu_{ij}^2}{uR_{\text{cell}}^2} \right) \left(\frac{\alpha_{\text{IR}}P_{\text{QCL}}}{\nu_{\text{IR}}} \right) \frac{1}{2k_{\text{DD}} + k_w}. \quad (3.8)$$

Threshold occurs when the unsaturated gain coefficient is equal to the cell loss, $\gamma_0 = \alpha_{\text{cell}}$, and the threshold power can be derived as [31]

$$P_{\text{th}} = \left(\frac{3h^2\epsilon_0\nu_{\text{IR}}}{2} \right) \left(\frac{uR_{\text{cell}}^2}{\mu_{ij}^2} \right) \left(\frac{\alpha_{\text{cell}}}{\alpha_{\text{IR}}} \right) (2k_{\text{DD}} + k_w) \quad (3.9)$$

At low pressures where molecule–wall collisions dominate, $k_w \gg k_{\text{DD}}$, $k_w \approx 2u/3R$, and the pump threshold simplifies to

$$P_{\text{th}} = (h^2\epsilon_0\nu_{\text{IR}}) \left(\frac{u^2R_{\text{cell}}}{\mu_{ij}^2} \right) \left(\frac{\alpha_{\text{cell}}}{\alpha_{\text{IR}}} \right) \quad (3.10)$$

3.5.2 THz output power

Output power is obtained by matching the saturated gain with the cavity loss,

$$\gamma = \frac{\gamma_0}{1 + \Phi/\Phi_s} = \alpha_{\text{cell}} \quad (3.11)$$

in which Φ is the photon flux density that is proportional to THz output power P_{THz} :

$$\begin{aligned} P_{\text{THz}} &= \frac{1}{2} h \nu_{\text{THz}} T(\pi R_{\text{cell}}^2) \Phi \\ &= \frac{1}{2} h \nu_{\text{THz}} T(\pi R_{\text{cell}}^2) \left(\frac{\gamma_0}{\alpha_{\text{cell}}} - 1 \right) \Phi_s \end{aligned} \quad (3.12)$$

where R_{cell} is the cavity radius, Φ_s is the saturated photon flux density with $\Phi_s = k_s \Delta N / \gamma_0$, and T is the power transmission coefficient of the front coupler. For wavelength smaller than the pinhole radius $\lambda_{\text{THz}} < 2r_0$, T can be approximated as $T \approx (r_0 / R_{\text{cell}})^2$. In the simple 3-level model, k_s can be derived as $k_s = (2k_{\text{DD}} + k_w) / 2$ following Ref. [31], and we obtain

$$\begin{aligned} P_{\text{THz}} &= \frac{1}{2} h \nu_{\text{THz}} (\pi r_0^2) \left(\frac{1}{\alpha_{\text{cell}}} - \frac{1}{\gamma_0} \right) \frac{\alpha_{\text{IR}} P_{\text{QCL}}}{2\pi R_{\text{cell}}^2 h \nu_{\text{IR}}} \\ &= \frac{1}{4} \frac{\nu_{\text{THz}}}{\nu_{\text{IR}}} \frac{r_0^2}{R_{\text{cell}}^2} \frac{\alpha_{\text{IR}}}{\alpha_{\text{cell}}} \left(1 - \frac{\alpha_{\text{cell}}}{\gamma_0} \right) P_{\text{QCL}} \\ &= \frac{1}{4} \frac{\nu_{\text{THz}}}{\nu_{\text{IR}}} \frac{r_0^2}{R_{\text{cell}}^2} \frac{\alpha_{\text{IR}}}{\alpha_{\text{cell}}} (P_{\text{QCL}} - P_{\text{th}}). \end{aligned} \quad (3.13)$$

Relationship $P_{\text{th}} / \alpha_{\text{cell}} = P_{\text{QCL}} / \gamma_0$ is used in the above derivation. The power efficiency equals the derivative of P_{THz} with respect to the pump power:

$$\eta = \frac{1}{4} \frac{\nu_{\text{THz}}}{\nu_{\text{IR}}} \frac{r_0^2}{R_{\text{cell}}^2} \frac{\alpha_{\text{IR}}}{\alpha_{\text{cell}}}. \quad (3.14)$$

Here are a few direct observations. The output power and power efficiency are proportional to the IR absorption coefficient α_{IR} . Since α_{IR} is proportional to the molecular pressure p and the population fraction of rotational level J_L , we have $P_{\text{THz}}, \eta \propto \alpha_{\text{IR}} \propto p n_{J_L}$. The output power and power efficiency are also proportional to the THz frequency, i.e., $P_{\text{THz}}, \eta \propto \nu_{\text{THz}} / \nu_{\text{IR}}$, which is the Manley–Rowe effect.

In this derivation, it was assumed that the linewidth of the QCL was much narrower than the Doppler width of the pumped infrared transition, and indeed this is satisfied in our case. Our experimental QCL is expected to have a linewidth in the range of 1-10MHz [40] compared to the 50-150MHz linewidth of typical molecular

infrared transitions. Our analysis with a QCL linewidth of 2 MHz finds excellent agreement with the experimental results. If the QCL linewidth were larger, the simple model derived here could reflect this fact by using an averaged α_{IR} , obtained by a convolution of the QCL and Doppler lineshapes, rather than using the above approximation of α_{IR} at its center frequency. Regarding the linewidth of the QPML laser transition, these lasers are perhaps more appropriately called “masers” [54] because their cavity linewidths ($\approx 10\text{-}100$ MHz) are larger than the molecular gain profile (≈ 1 MHz).

Chapter 4

Capillary Instability with Thermal Gradients¹

4.1 Introduction

Capillary instability of liquid jets has been widely studied since Plateau [55] first showed that whenever a cylindrical jet's length exceeded its circumference, it was always unstable due to capillary forces or surface tension. Plateau's conclusion was drawn based on a geometric argument. Lord Rayleigh introduced a linear instability analysis to quantitatively solve the break-up mode for an inviscid fluid jet [56, 57] and precisely obtain the most unstable mode. Later on, Tomotika [58] generalized Rayleigh's analysis to study the growth rate when a cylindrical viscous liquid was surrounded by another viscous fluid.

In recent years, in-fiber capillary instability has been exploited in a new way to fabricate micro particles: the fiber-drawing process, as shown in Fig. 4-1. A macro-scale preform of a multimaterial fibre is heated to a viscous state and then thermally drawn into an extended concentric fiber with much smaller diameter. For example, a fiber preform with Si core and glass cladding can be drawn into a long fiber with submicron diameter. Capillary instability is then induced by thermal treatment

¹The work in this chapter was done in collaboration with Amy Guyomard (MIT), Xiangdong Liang (MIT), J.C. Nave (McGill University), and Steven G. Johnson (MIT).

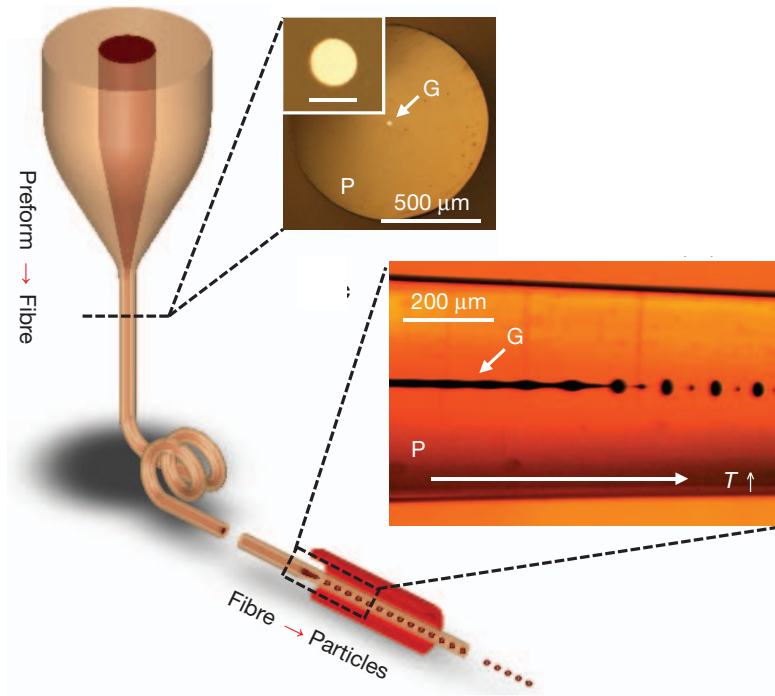


Figure 4-1: Experimental setup of the fiber-drawing process [59]: A macroscopic preform is thermally drawn into a fibre. Subsequent thermal processing of the fibre induces the capillary instability, resulting in the fiber core breakup and spherical particles.

of the extended fiber and breaks up the core into spherical Si particles, which can be widely used in a broad range of applications such as photonic devices, optical communications, and bio-engineering. This novel approach of particle fabrication easily produces uniform-size spherical particles over a wide range of diameters, has great scalability to fabricate millions of microspheres with just one drawing process, and is easy to produce structured spheres such as multi-layered particles [59, 60]. Theoretically, the fiber-drawing process can be described by modelling the fiber core as a viscous fluid thread surrounded by another viscous fluid, and making use of the classical Tomotika formula to calculate the growth rate for potential instability modes. Moreover, Liang extended the Rayleigh-Plateau and Tomotika instability analysis to multi-fluid geometries which accurately described the experimental observations [60].

More recently, researchers have developed an adapted way to produce controllable-size spheres by an axial thermal gradient and a controlled feed speed [61]. In the

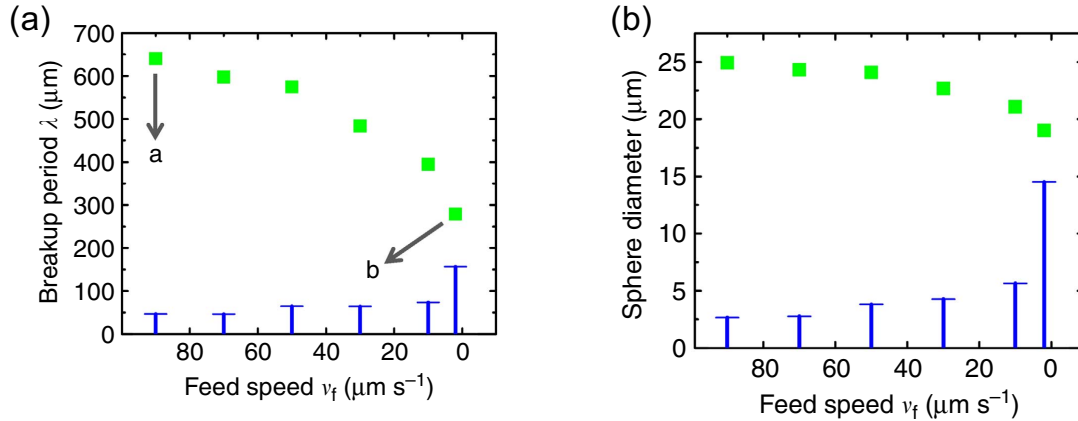


Figure 4-2: (a) Break-up periods and (b) corresponding sphere diameters (squares) as a function of the feed speed for a 4 mm Si-core fibre shown together with the magnified graphs of standard deviation values (bars) as they appear within each one of the samples. The s.d. values in (a) are shown 10-fold magnified and 1,000-fold magnified in (b). Figures are from [61].

process, the fibre is fed into a spatially localized flame at a controlled rate. By continuously feeding the fibre from low-temperature region into the high-temperature flame, particles emerge one by one. The size of the sphere is highly controllable by the feed speed. And surprisingly, the sphere size can be well below that of an isothermal process and approaches the fundamental diameter limit. This chapter focuses on developing a numerical tool and an analytical model to understand the capillary instability with thermal gradient.

In the following sections, we will first develop a large-scale parallel Stokes-equation solver to numerically calculate the time evolution of the capillary breakup process and extract the pinch-off period in the fiber. A few examples with different temperature profiles and different layers of materials will be shown. In addition, accurate numerical simulations enable us to develop a semi-analytical model with quantitative validation. Our 1d model fits the simulation results over a wide range of the width of the temperature gradient.

4.2 Numerical modeling of capillary breakup with thermal gradient

Here, we consider an axisymmetric two-layer fluid system in the low Reynolds number regime. Assume the surface tension at the interface is γ . Inner layer and outer cladding are both highly viscous fluids with viscosities $\mu_i(z)$ and $\mu_o(z)$, respectively. Due to thermal gradient, both μ_i and μ_o vary with axial (z -) direction. In the silicon-silica fiber, viscosities of the inner silicon core and silica cladding can be estimated from the spatially varying temperature $T(z)$ by

$$\mu_i(z) = 10^{\frac{819.0}{T(z)+273} - 3.727} \text{Pa} \cdot \text{s} \quad (4.1)$$

$$\mu_o(z) = 10^{\frac{26909.0}{T+273} - 7.2348} \text{Pa} \cdot \text{s}. \quad (4.2)$$

The fluid dynamics in the system is described by the Stokes equation:

$$-\nabla p + \nabla \cdot [\mu(\mathbf{r}) (\nabla \mathbf{v} + \nabla \mathbf{v}^T)] = \gamma \delta(\phi(\mathbf{r})) \kappa(\phi(\mathbf{r})) \frac{\nabla \phi(\mathbf{r})}{|\nabla \phi(\mathbf{r})|} \quad (4.3)$$

where p and \mathbf{v} are the pressure and velocity fields, $\phi(\mathbf{r})$ is the level-set function which defines the interface \mathbf{r}_i with $\phi(\mathbf{r}_i) = 0$ (described with more details below), $\delta(\phi)$ is the delta function, and $\kappa(\phi)$ is the curvature of the interface. A more general form for N -layers concentric fluid system with $N - 1$ interfaces can be written as

$$-\nabla p + \nabla \cdot [\mu (\nabla \mathbf{v} + \nabla \mathbf{v}^T)] = \sum_{n=1}^{N-1} \gamma^{(n)} \delta(\phi^{(n)}) \kappa(\phi^{(n)}) \frac{\nabla \phi^{(n)}}{|\nabla \phi^{(n)}|} \quad (4.4)$$

Additionally, we assume the fluids are incompressible with continuity equation

$$\nabla \cdot \mathbf{v} = 0. \quad (4.5)$$

In order to describe the movement of the fluid interface, we use the level-set method. Level-set methods were firstly proposed by James A. Sethian and Stanley Osher in 1988 to deal with evolving boundaries or interfaces problems [62]. In the

level-set method, a level-set function $\phi(\mathbf{r})$ is defined for all spatial points \mathbf{r} , not just the ones on the boundaries. The interface is implicitly represented by the zero level set $\phi(\mathbf{r}) = 0$. An example of a signed distance function $\phi(\mathbf{r})$ discretized on a Cartesian grid is shown in Fig. 4-3. It has the property that $|\nabla\phi| = 1$ with different signs at the two sides of the interface. Also, $|\phi(\mathbf{r})|$ gives the distance from \mathbf{r} to the boundary $\phi = 0$. The level-set method itself doesn't require $\phi(\mathbf{r})$ to be a distance function, but the numerical approximation is inaccurate if ϕ has large variations in the gradient. So we want to keep ϕ close to a signed distance function by frequent re-initialization processes [63] as shown below.

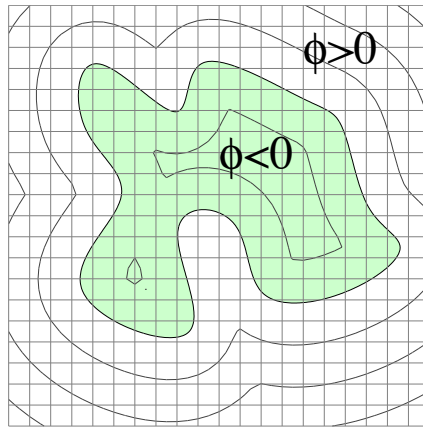


Figure 4-3: An example of level-set function: a signed distance function discretized on a Cartesian grid. Figure from Ref. [63].

The movement of the interface is governed by the following convection equation that updates the level-set function,

$$\frac{\partial\phi}{\partial t} + \mathbf{v} \cdot \nabla\phi = 0 \quad (4.6)$$

where \mathbf{v} is the velocity fields obtained from the Stokes equation. Re-initialization steps need to be taken frequently to ensure that the gradient of level-set function at the interface is around 1. The re-initialization is performed by evolving discretized timesteps of the equation:

$$\frac{\partial\phi}{\partial t} + \text{sign}(\phi)(|\nabla\phi| - 1) = 0. \quad (4.7)$$

In our implementation, one re-initialization timestep is taken typically at every 10 steps of interface evolution of (4.6).

Numerically, (4.3) and (4.5) are discretized by a second-order finite-difference scheme, and solved by a parallel MUMPS direct solver [39] using the PETSc library. For equations (4.6), and (4.7), we use a third order TVD (total variation diminishing) Runge-Kutta method for time evolution and the HJ WENO method for the spatial differentiation [62]. More details on the numerical schemes are presented in Appendix H.

In the following sections, we will present a few examples of numerical modeling of capillary breakup with thermal gradient. Exact temperature profile and the viscosity distribution in experiments are difficult to measure. But our numerical model gives a rough estimate of the temperature profile that quantitatively matches the measured breakup period. In addition, a semi-analytical 1d model is proposed to explain the breakup mechanism which fits fairly well with the simulations.

4.3 Results and discussion

4.3.1 Example 1

We first present a numerical example of a three-layer fluid fiber with uniform viscosity in each layer along the z direction. From the linear analysis in Ref. [60], different instability time-scales of the two interfaces create competing modes: which mode is the most unstable depends on the radius, viscosity, and surface tension values of the two interfaces. Fig. 4-4 shows two numerical simulations of a three-layer system with different surface tensions for the outer interface. The radii of the inner and outer interfaces are $R^{(1)} = 1.0$ and $R^{(2)} = 5.0$, respectively. All three layers have viscosities equal to $\mu^{(1)} = 0.91$, $\mu^{(2)} = 1.0$, and $\mu^{(3)} = 0.91$. The surface tension $\gamma^{(1)}$ of the inner interface for both cases is 1.5, while the surface tension of the outer interface $\gamma^{(2)}$ is 1.5 for Fig. 4-4(a) and 25.0 for Fig. 4-4(b). In Fig. 4-4(a), the two interfaces have similar surface tensions, but the radius of the outer interface is 5 times bigger than the inner interface, indicating the inner interface is about 5 times more unstable and certainly breaks up faster. While in Fig. 4-4(b) with a much bigger $\gamma^{(2)}$, the outer interface breaks up first with $\sim 5\times$ larger mode wavelength, which also arises from the bigger radius if we assume ka is a constant.

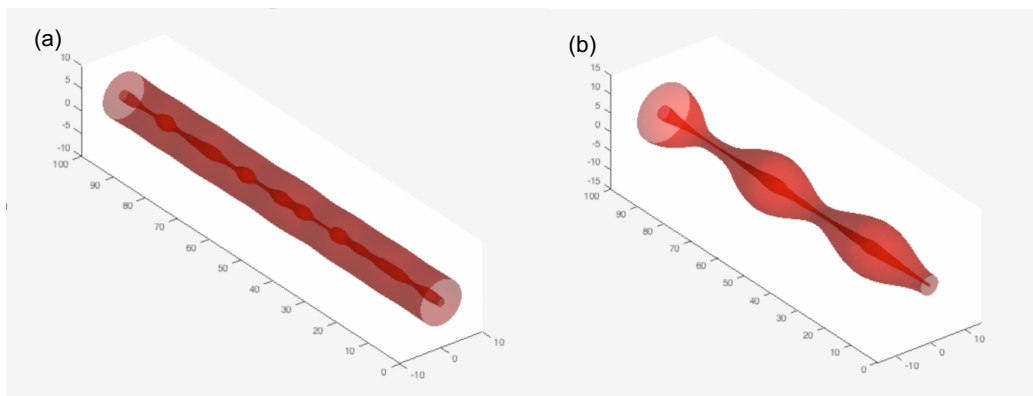


Figure 4-4: Numerical Stokes-flow simulations for a three-layer system with different surface tension values for the outer interface. Radius of inner and outer interfaces are 1.0 and 5.0, respectively. All three layers have viscosity equal to 0.91, 1.0, and 0.91. Surface tension of inner interface for both cases is 1.5, while the surface tension of the outer interface is 1.5 in (a) and 25.0 in (b).

4.3.2 Example 2

Next, we present both numerical modeling and experimental validation of a Si-in-SiO₂ fiber fed into a laser spot. As mentioned in Ref. [61], the interfacial tension between Si and SiO₂ was 1.5 J/m². This value was obtained using a first-principle approach at absolute zero temperature, i.e., 0 Kelvin, which could be very different at the operating temperature as high as 2000 K. It is not easy to determine the correct interfacial tension of Si/SiO₂ in experiment at such high temperatures. One potential method is to run simulations with varying interfacial tensions and match experimental observations.

Fig. 4-5 shows numerical simulations with two different interfacial tensions 1.5 J/m² and 5.0 J/m². In the simulation, we assume the temperature profile by the laser heating linearly increases from 1400 °C to 1700 °C with a very narrow transition width around 3 micrometers. The comparison with experimental observation in both spatial and temporal scale indicates 5.0 J/m² agrees better with experiments quantitatively. In order to determine the exact value of surface tension in the future, we'll collaborate with experimental group to obtain the interface snapshots with a known temperature profile, and then run simulations with varying interfacial tensions to find the best match.

4.3.3 Capillary breakup with a thermal gradient

Lastly, we return to the case where controllable size Si spheres can be fabricated by feeding a Si-in-SiO₂ fiber into a hydrogen torch with axial thermal gradient and with controlled feed speed v_f . Note that the melting point of Si is 1414°C. The temperature of the flame is approximated to linearly change from 1400°C to 1850°C with a transition width w .

$$T(z) = \begin{cases} 1400 + 450z/w, & \text{for } z \leq w \\ 1850, & \text{for } z > w. \end{cases} \quad (4.8)$$

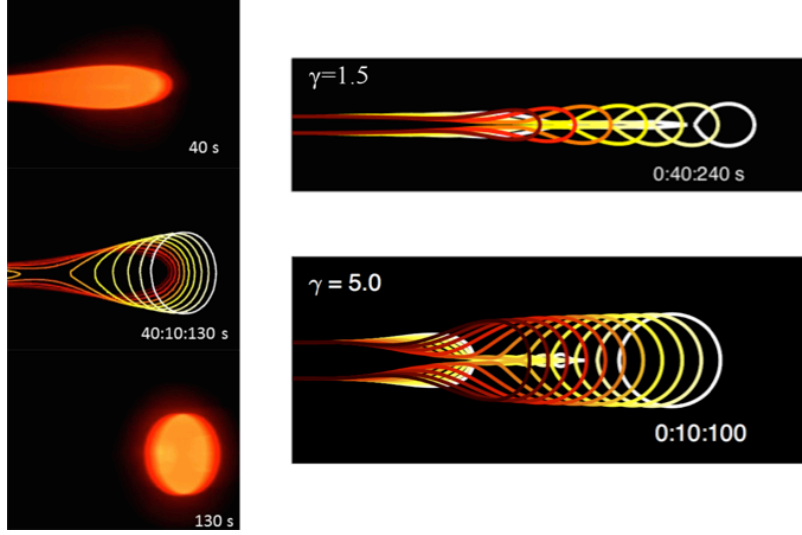


Figure 4-5: Snapshots of Si/SiO₂ fiber interface in experiment (left) and numerical simulations (right) with two different values of interfacial tension. 5.0 J/m² gives results that match better with experimental observation quantitatively. (The experimental figure is provided by Prof. Fink group at MIT)

Viscosities of Si and SiO₂ are shown in (4.1) and (4.2). The interfacial tension between the two fluids is set as 10 J/m² in our simulations. This value is larger than 1.5 J/m² used in Ref. [61] which underestimates the surface tension as demonstrated in previous section. The core radius is 2 μm . In the simulation, the total radial size is typically 30 μm with grid spacing equal to 0.2 μm , and the total length in the z direction is around 2 mm. The discretized matrix size of the Stokes equation is around $10^6 \times 10^6$. The solution is obtained using the MUMPS direct solver with PETSc library, which is a widely used library for scientific computing especially for solving partial differential equations. It typically takes about 10 seconds with 32 CPU cores for one timestep of the Stokes equation to obtain pressure p and velocities u and w . But as the simulation gets closer to the pinch-off point, velocities get bigger and the time step gets smaller, so that the time evolution gets much slower. A full simulation with a few pinch-offs typically takes about 4–5 days, or about 3,000 CPU hours. Here, we first fit the transition width w to match the experimental observations, following which a simple 1d model capturing the key breakup mechanism is proposed to fit the numerical results.

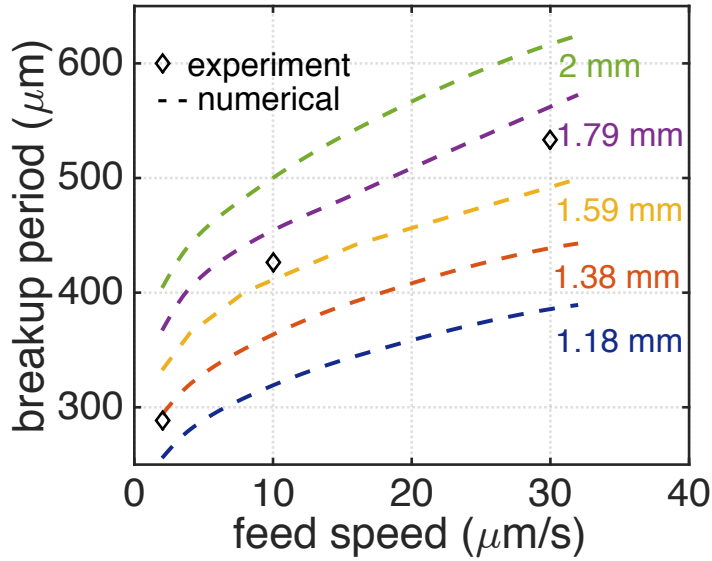


Figure 4-6: Breakup period predicted by both numerical simulation (dashed) and experimental measurements (diamond) as a function of feed speed. Temperature profiles of the flame varies linearly between 1400 °C to 1850 °C, with different transition width from 1.18mm to 2.0mm.

Figure 4-6 shows the breakup period of numerical modeling with different values of flame width w from 1.2mm to 2.0mm. The breakup period increases with the feed speed, mainly because more Si is sent to higher temperature region within pinch-off time. However, the pinch-off point also shifts to higher temperature region, resulting in a faster pinch-off time. It overall gives the nonlinear shape of breakup period as a function of feed speed as in Fig. 4-6. The numerical results agree quite well with experimental measurements with temperature transition width around 1.6mm, which is within the reasonable range for a hydrogen torch.

Based on the numerical results without any unknown parameters, we also develop a 1d semi-analytical model. Experimental results are not adopted for model validation because there are many unknown parameters in experiments. In the semi-analytical model, the total breakup time consists of a “feed” time and a capillary instability time. We propose that the pinch-off point x_p as shown in Fig. 4-7 minimizes the total

breakup time:

$$\begin{aligned}
\min_x g(x) &= \min_x \left(\frac{x}{v_f} + \tau \right) \\
&= \min_x \left(\frac{x}{v_f} + \alpha \frac{2r_0 \langle \mu_o(x) \rangle}{\gamma} \right) \\
&= \min_x \left[\frac{x}{v_f} + \alpha \frac{2r_0}{\gamma} \left(\int_{x-v_f\tau}^x \frac{1}{\mu_o(x')} dx' \right)^{-1} \right]
\end{aligned} \tag{4.9}$$

where x/v_f is the feed time and τ is the capillary pinch-off time averaged over region $x_p - v_f\tau$ and x_p . τ is approximated by Tomotika's linear stability analysis, and α is a fitting parameter accounting for the real nonlinear pinch-off time. Note that Tomotika's growth rate is approximated as

$$\sigma \approx \frac{\gamma}{2r_0\mu_o} \tag{4.10}$$

in the limit of $\mu_i/\mu_o \rightarrow 0$ which is valid in our case. Comparison of breakup period

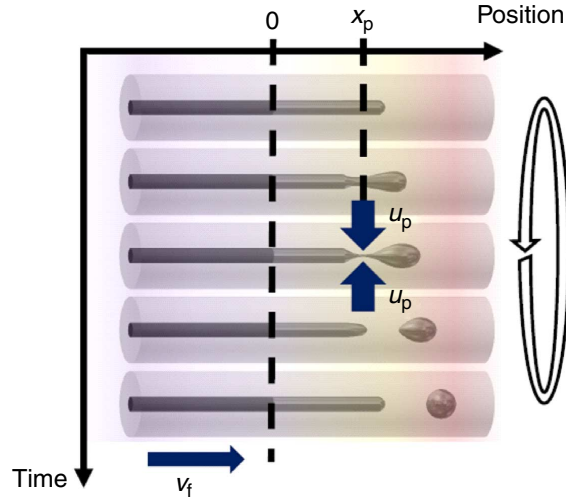


Figure 4-7: Schematics of the capillary breakup process with feed speed v_f . Figure is from Ref. [61].

between the numerical simulations and the 1d model is shown in Fig. 4-8. In the 1d model, fitting parameter α equals 0.45 for all curves. The fitting model agrees very well with the numerical simulation for all the temperature profiles with different

transition width, in particular when the feed speed is below $20 \mu\text{m/s}$. The 1d model slightly overestimates the breakup period at higher feed speed, due to the nonlinearity behavior near the pinch-off time.

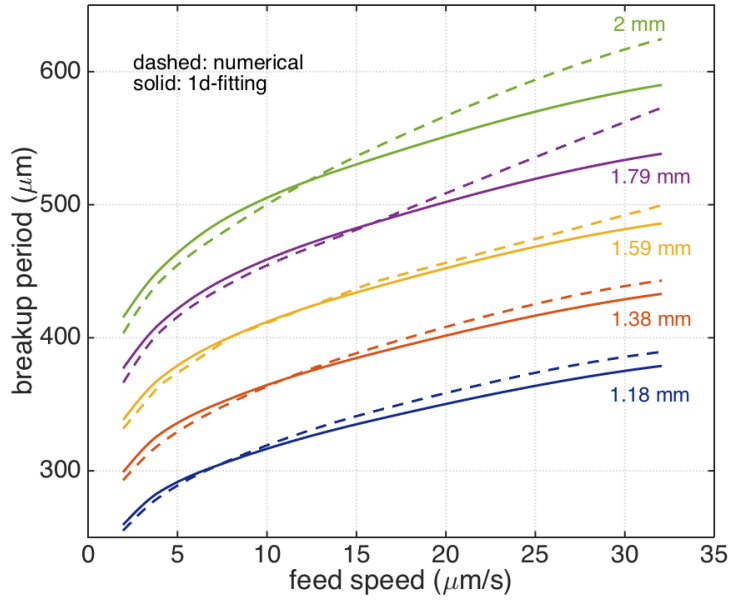


Figure 4-8: Breakup period predicted by both numerical simulation (dashed) and 1d analytical approximation (solid) as a function of feed speed. Temperature profiles of the flame varies linearly between $1400 \text{ }^\circ\text{C}$ to $1850 \text{ }^\circ\text{C}$, with different transition width from 1.18mm to 2.0mm . Fitting parameter α is 0.45 for the fitting.

4.4 Summary

In this chapter, we have developed a large scale parallel numerical solver for Stokes-equation to simulate and study the capillary breakup phenomena between concentric multi-fluid systems with thermal gradient. Our efficient parallel solver is able to scale up the simulation regime to experimental scale. With the numerical tool, we compute the breakup period as a function of feed speed which matches the experimental measurements. Spheres with controllable size can be obtained by controlling the feed speed.

Additionally, a one dimensional semi-analytical model is proposed based on minimization of the total breakup time consisting of feed time and capillary instability time. However, the model includes a fitting parameter accounting for the nonlinear pinch-off time which only allows the model to make qualitative predictions. To be able to quantitatively predict the capillary breakup dynamics with any thermal gradient, other theoretical methods such as marginal stability analysis [64] deserve exploration in the future.

Chapter 5

Concluding Remarks

In this thesis, we have demonstrated how to build and model a compact, high-efficiency, and widely frequency-tunable gas-phase terahertz lasers, after which we also presented how to model the capillary instability of multi-fluid fibers with thermal gradient.

We first developed an innovative model for the OPFIR laser that correctly captures the full physics of the pump and lasing processes. The numerical model accurately predicts the lasing behavior across all pressures. Validated against experiments quantitatively, our model shows that nearly all previous OPFIR lasers were operating in the wrong regime and that $10\times$ greater efficiency is possible by redesigning the terahertz cavity. These results reintroduce the use of OPFIR lasers as a powerful and compact source of terahertz radiation.

Furthermore, a revolutionary concept of QCL-pumped molecular laser is proposed as a widely frequency-tunable compact terahertz source. Using laughing gas N_2O , we demonstrated broad tunability over 31 rotational transition lines with 25.1 GHz frequency spacing, spanning 0.25–0.80 THz. Our theoretical model is able to constrain the key molecular parameters, match quantitatively with experimental measurements, and predict the optimal performance of the laser. Additionally, a universal analytical theory is developed for QPML to identify the key factors for improving the laser performance. We believe that these developments will revive interest in optically pumped molecular laser as a powerful, widely tunable, and compact source of tera-

hertz radiation.

Molecular gas laser in a hollow-core fiber system is inspired by combining the narrow bandwidths and frequency flexibility of gas lasers with the interaction lengths and high powers enabled by long fibers. And it's important to understand and be able to control the fiber drawing process. In the fiber drawing process, capillary instability and thermal gradient is important for micro particle fabrication. In order to fully understand the nonlinear drawing process, we developed a large-scale parallel Stokes-equation numerical solver to study the capillary breakup phenomenon in a multi-fluid system due to surface tension. The numerical results match the experimental observation with fitted temperature profile which is unknown in experiments. A pinch-off criteria which minimizes the total breakup time is also proposed. This 1d semi analytical model with the criteria well-matches the simulations.

There are a few directions worth exploring in the future. Our modeling describes continuous wave OPFIR lasers. While pulsed lasers with high pulse intensities are also very important in many applications such as terahertz spectroscopy, ultrafast imaging, tele-communication, and remote sensing. Instead of solving the rate equations directly for steady state as presented in this thesis, time evolution is needed for modeling a pulsed laser. However, the rate equations are quite stiff ODEs with divergent characteristic time scales especially at high pressures and with high pump powers. As a consequence, explicit numerical methods fails and we need to exploit efficient implicit numerical methods for the problem. As for modeling the capillary instability, the semi analytical model including a fitting parameter for the nonlinear pinch-off time only makes *qualitative* predictions. To be able to *quantitatively* describe the capillary breakup dynamics with thermal gradient, other theoretical methods such as marginal stability analysis deserve explorations in the future.

Appendix A

Parameters of Methyl Fluoride

Dipole moments, rotational constants, vibrational energies, and collisional cross sections of two methyl fluoride isotopes are listed in the following table.

Table A.1: Parameters of Methyl Fluoride

	$^{12}\text{CH}_3\text{F}$	$^{13}\text{CH}_3\text{F}$
Mass (AMU)	34	35
Dipole moment μ_0 (Debye)	1.86	1.86
$d\mu_3/dQ_3$ (Debye)	0.2756	
A_0 (MHz)	155352.7	
B_0 (MHz)	25536.1499	24862.6427
D_{J_0} (MHz)	0.060233	0.057683
D_{JK_0} (MHz)	0.4395743	0.42441
B_3 (MHz)	25197.5092	24542.1324
D_{J_3} (MHz)	0.0568788	0.055156
D_{JK_3} (MHz)	0.05180831	0.47788
E_3 (cm^{-1})	1048.61	1027.49
E_6 (cm^{-1})	1182.35	1175
E_2 (cm^{-1})	1459.40	1453.64
E_5 (cm^{-1})	1467.82	1465.58
E_1 (cm^{-1})	2966.25	
E_4 (cm^{-1})	3005.81	
σ_{DD} (\AA^2)	320.0	
σ_{GKC} (\AA^2)	44.0	
σ_{SPT} (\AA^2)	137.0	
σ_{VSwap} (\AA^2)	21.0	
σ_{36} (\AA^2)	1.61	

Appendix B

Average velocity of the population flux into the wall

The boundary condition for the vibrational levels, discussed in Section 2.3.3, depends on the average molecular speed \bar{v} in the direction perpendicular to the wall (say, $+x$). In this section, we briefly review the computation of \bar{v} by standard methods. In particular, the molecular velocity follows the Maxwell–Boltzmann distribution

$$f_{\text{MB}}(v_x) = \sqrt{\frac{m}{2\pi k_B T}} e^{-\frac{mv_x^2}{2k_B T}}.$$

The average velocity is obtained by

$$\begin{aligned}\bar{v} &= \frac{\int_0^\infty v_x f_{\text{MB}}(v_x) dv_x}{\int_0^\infty f_{\text{MB}}(v_x) dv_x} = 2 \int_0^\infty v_x f_{\text{MB}}(v_x) dv_x \\ &= \sqrt{\frac{m}{2\pi k_B T}} \int_0^\infty e^{-\frac{mv_x^2}{2k_B T}} d(v_x^2) \\ &= \sqrt{\frac{2k_B T}{\pi m}}.\end{aligned}$$

On the other hand, the average absolute velocity is

$$\begin{aligned}\langle v_{\text{abs}} \rangle &= \left(\frac{m}{2\pi k_B T} \right)^{3/2} \int |\mathbf{v}| \exp \left(-\frac{mv^2}{2k_B T} \right) d\mathbf{v} \\ &= \sqrt{\frac{8k_B T}{\pi m}}.\end{aligned}$$

Therefore $\bar{v} = \langle v_{\text{abs}} \rangle / 2$.

Appendix C

Transmission through the output pinhole

THz radiation transmitted through the output pinhole affects the calculation of total loss, lasing threshold, and the output power. Instead of using the ratio of pinhole area and the cavity cross section [31], which is only correct for a uniform intensity (e.g. a plane wave), the transmission coefficient T is computed by integrating the waveguide mode's Poynting flux over the output pinhole. (This is also an approximation, which is valid because the 1mm diameter pinhole is not small compared to 1.2mm wavelength. The radiation through a very subwavelength hole would require an entirely different approach [65].) For a circular waveguide's TE_{nm} mode [35],

$$P_{\text{rad}} = \int_S \frac{1}{2} \Re(\mathbf{E} \times \mathbf{H}^*)_z d\mathbf{r} = \frac{Z_{nm}^{\text{TE}}}{2} \int_S (|H_r|^2 + |H_\phi|^2) d\mathbf{r} \quad (\text{C.1})$$

in which $Z_{nm}^{\text{TE}} = (k_0/\beta_{nm})Z_0$ is the modal wave impedance. k_0 is the free space wave number, $\beta_{nm} = \sqrt{k_0^2 - (p'_{nm}/R)^2}$ is the propagation constant, and Z_0 is the vacuum impedance. Here we consider the TE_{01} mode in a circular waveguide, since it has the lowest Ohmic loss. It is straightforward to do a similar analysis for other cavity modes.

The radiated power through an area S for the TE₀₁ mode is

$$P_{\text{rad}} = \frac{Z_{01}^{\text{TE}}}{2} \left(\frac{\beta_{01} p'_{01}}{R k_{c,01}^2} \right)^2 \int_S J_1^2 \left(\frac{p'_{01} r}{R} \right) d\mathbf{r} \quad (\text{C.2})$$

where $p'_{01} = 3.83$ is the first zero of the Bessel function derivative $J'_0(x)$ and $k_{c,01} = p'_{01}/R$ is the wavenumber corresponding to the TE₀₁ mode. The total radiation over the whole waveguide cross section is

$$P_{\text{tot}} = \frac{Z_{01}^{\text{TE}}}{2} \left(\frac{\beta_{01}}{k_{c,01}^2} \right)^2 2\pi \int_0^{p'_{01}} J_1^2(x) x dx = \frac{\pi Z_{01}^{\text{TE}} \beta_{01}^2}{2k_{c,01}^4} p_{01}^2 J_0^2(p'_{01}). \quad (\text{C.3})$$

In the experiment, the pinhole is centered at $r = 0$ with radius equal to $R/5$, so the radiation through the pinhole is

$$P_{\text{pinhole}} = \frac{\pi Z_{01}^{\text{TE}} \beta_{01}^2}{k_{c,01}^4} \int_0^{p'_{01}/5} J_1^2(x) x dx. \quad (\text{C.4})$$

The effective transmission coefficient is

$$T_{\text{exp}} = \frac{P_{\text{pinhole}}}{P_{\text{tot}}} = \frac{\int_0^{p'_{01}/5} J_1^2(x) x dx}{\int_0^{p'_{01}} J_1^2(x) x dx} \approx 0.016.$$

T_{exp} is smaller than the area ratio 0.04, due to the fact that the Poynting flux of TE₀₁ mode is higher around $r = 0.48R$, instead of $r = 0$. This indicates that an off-centered pinhole would give larger transmission, which would increase the lasing efficiency (and the threshold power) by increasing the THz radiation rate compared to the Ohmic loss rate. Here, we compute the optimized transmission coefficient for a pinhole centered at $r = 0.48R$ with the same radius $R/5$:

$$T_{\text{opt}} = \frac{\int_0^{2\pi} \int_0^{R_{\text{pinhole}}} J_1^2(p'_{01} x(r, \theta)/R) r dr d\theta}{2\pi \int_0^R J_1^2(p'_{01} r/R) r dr} \approx 0.075,$$

where $x(r, \theta) = \sqrt{r_0^2 + r^2 - 2rr_0 \cos \theta}$ with $r_0 = 0.48R$ is the pinhole center. This enhanced transmission coefficient for an off-center pinhole increases both the output power and the efficiency by decreasing the fraction of power lost to Ohmic absorption.

Appendix D

Spontaneous emission time

In Chapter 2, the spontaneous emission lifetime t_{sp} is taken to be 10 seconds to compute the gain coefficient and the output power for $^{13}\text{CH}_3\text{F}$ OPFIR lasers. In fact, the precise value of t_{sp} has little effect on the peak output power far above threshold. In this section, we first demonstrate the effect of t_{sp} by explicit numerical calculations (re-running our model with different values of t_{sp} , shown in Fig. D-1), and then we present a simple analytical explanation for the lack of influence of t_{sp} .

Fig. D-1 shows the numerical output power of both direct (solid lines) and refilling (dashed lines) lasing as a function of pressure with the input pump power equal to 10W, and with three different spontaneous emission lifetimes t_{sp} : 1 sec (blue), 10 sec (red), and 100 sec (green). The output power curves are very close, especially in the high-power regions far above the threshold, for both direct and refilling inversions. The biggest effect of t_{sp} is on the high-pressure cutoff for the direct transition, but in this (uninteresting, low-efficiency) high-pressure regime our model's z -averaging assumption is inaccurate as discussed in Chapter 2.

It is straightforward to show analytically that the effect of t_{sp} approximately cancels in the high-power regime. In that regime, far above threshold, $\Phi \gg \Phi_s$, and (2.37) from the main text becomes

$$\alpha_{\text{THz}} \approx \frac{1}{V} \int \int \frac{\Delta N(\nu)\sigma(\nu)}{\Phi\tau_s\sigma(\nu)} d\nu d\mathbf{r} = \frac{\langle \Delta N \rangle}{\Phi\tau_s} \quad (\text{D.1})$$

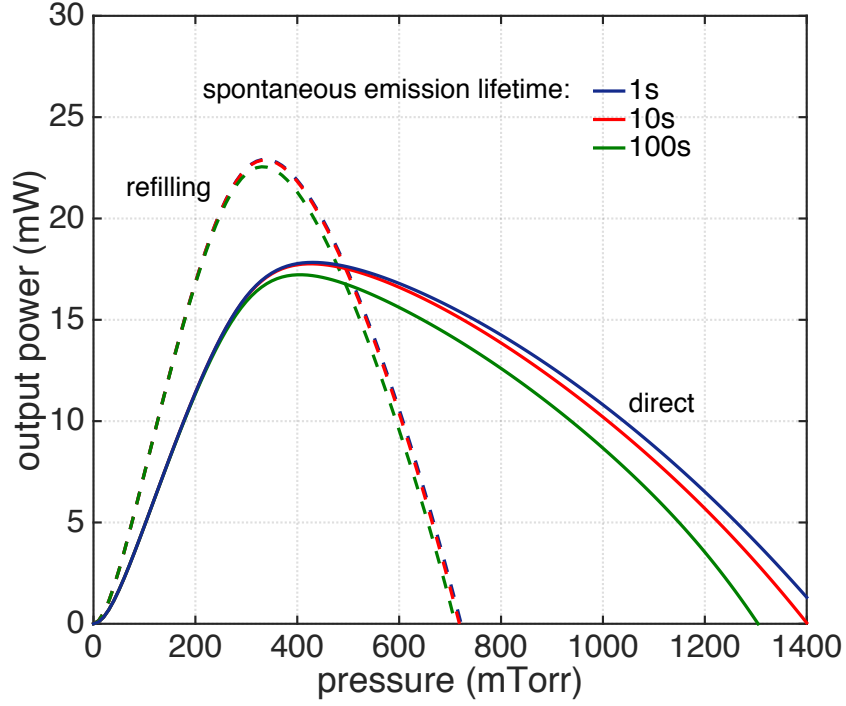


Figure D-1: Numerical output power of both direct (solid lines) and refilling (dashed lines) lasing versus pressure with the input pump power equal to 10W, and with three different spontaneous emission lifetimes t_{sp} : 1sec, 10sec, and 100sec. t_{sp} has little effect on the peak output power far above threshold for both lasing transitions.

where $\langle \Delta N \rangle$ is the spatially averaged population inversion and $\sigma(\nu)$ is the transition cross section (which depends on t_{sp}). This equation yields an approximate flux density

$$\Phi \approx \frac{\langle \Delta N \rangle}{\tau_s \alpha_{THz}}, \quad (\text{D.2})$$

in which σ has been cancelled and therefore the dependence on t_{sp} has vanished.

Appendix E

Conservation of population

Here, we will show how we can derive

$$N^{\text{net}}(r) \equiv N_0(r) + N_3(r) + N_\Sigma(r) = 0 \quad (\text{E.1})$$

for all positions r . By adding the rate equations of vibrational levels with the same A/E symmetry, we obtain

$$\dot{N}_S^{\text{net}}(r, t) = D\nabla^2 N_S^{\text{net}}(r, t). \quad (\text{E.2})$$

Note that VS process doesn't add populations, and SPT processes also doesn't add net population because the non-thermal rotational populations in V_0 and V_3 are equal and the SPT transition rates are the same. The boundary condition for N^{net} is $-D\frac{\partial N_S^{\text{net}}}{\partial r} = \bar{v}N_S^{\text{net}}/2 - \sum_p q_p N_S^{\text{net}}/2 = 0$ or simply

$$\frac{\partial N_S^{\text{net}}}{\partial r} = 0. \quad (\text{E.3})$$

(E.2) and (E.2) simply describe a diffusion equation with Neumann boundary conditions, which is well known to conserve the “mass”. Hence the integral of the total population N is conserved over time, with the steady-state being a constant, set to

zero by the initial conditions, i.e.,

$$N_S^{\text{net}}(r) = 0. \tag{E.4}$$

Appendix F

V-swap

We consider the most common form of V-swap process occurring between v_0 and v_3 molecules: the swap of A or E types. Here, we show that to the first order, V-swap effectively moves nonthermal rotational population to A and E thermal pools equal rates. Collisions between thermal v_3 and thermal v_0 are neglected since they don't induce any change of population.

For the non-thermal populations in v_3 state, we consider the following two processes:



The net effect is to move $2x$ population from v_3A^{nonth} to v_3 thermal pools, half amount to the A type and the other half to the E type, and to move x amount of population from v_0E to v_0A . x is determined by the V-swap collisional cross section. Note that we only consider collisions between nonthermal population and the v_0 pool which has largest amount of population. We also assume A and E types have the same population which is true to the first order.

Similarly, for the non-thermal population in v_0 state, we consider:

$$v_0 A^{\text{nonth}} + v_0 A \leftrightarrow v_0 A + v_0 A \quad (\text{F.3})$$

$$v_0 A^{\text{nonth}} + v_0 E \leftrightarrow v_0 E + v_0 A \quad (\text{F.4})$$

The net effect is to move $2y$ amount of population from non-thermal $v_0 A$ to thermal $v_0 A$ state. So the total net effect is to decrease $2x$ population from $v_3 A^{\text{nonth}}$, $2y$ population from $v_0 A^{\text{nonth}}$ and x population from $v_0 E$, and increase x population in $v_3 A$, x population in $v_3 E$, and $2y + x$ population in $v_0 A$.

There is an important observation: $x + y = 0$. This is true because the pump increasing one population in $v_3 A^{\text{nonth}}$ would create a “hole” in $v_0 A^{\text{nonth}}$, and the transition rates (such as the dipole–dipole collision, SPT process, etc.) are the same for both $v_3 A^{\text{nonth}}$ and $v_0 A^{\text{nonth}}$. Therefore, the total net effect is the movement of $2x$ population from $v_3 A^{\text{nonth}}$, half to $v_3 A$ and half to $v_3 E$, and the movement of $2y$ population from $v_0 A^{\text{nonth}}$, half to $v_0 A$ and half to $v_0 E$. x and y are determined by the V-swap collisional cross section.

Appendix G

Dipole matrix element

The dipole matrix element, defined as $|\langle i|\mu|f\rangle|^2$, determines the transition probability for transition $i \rightarrow f$. For a pure rotational transition that doesn't change vibrational state, the dipole matrix element is given by

$$|\langle J+1, K, V|\mu|J, K, V\rangle|^2 = \mu_0^2 \frac{(J+1)^2 - K^2}{(J+1)(2J+1)}, \quad (\text{G.1})$$

$$|\langle J, K, V|\mu|J, K, V\rangle|^2 = \mu_0^2 \frac{K^2}{J(J+1)}, \quad (\text{G.2})$$

$$|\langle J-1, K, V|\mu|J, K, V\rangle|^2 = \mu_0^2 \frac{J^2 - K^2}{J(2J+1)}. \quad (\text{G.3})$$

μ_0 is the dipole moment. As for the IR absorption line, vibrational state changes, with dipole matrix element for the R-, Q-, and P-branch given by

$$|\langle J+1, K, V+1|\mu|J, K, V\rangle|^2 = \left[\left(\frac{d\mu}{dQ_k} \right)^2 \frac{\hbar}{2\omega_k} (V+1) \right] \frac{(J+1)^2 - K^2}{(J+1)(2J+1)}, \quad (\text{G.4})$$

$$|\langle J, K, V+1|\mu|J, K, V\rangle|^2 = \left[\left(\frac{d\mu}{dQ_k} \right)^2 \frac{\hbar}{2\omega_k} (V+1) \right] \frac{K^2}{J(J+1)}, \quad (\text{G.5})$$

$$|\langle J-1, K, V+1|\mu|J, K, V\rangle|^2 = \left[\left(\frac{d\mu}{dQ_k} \right)^2 \frac{\hbar}{2\omega_k} (V+1) \right] \frac{J^2 - K^2}{J(2J+1)}. \quad (\text{G.6})$$

Here, $\left(\frac{d\mu}{dQ_k} \right)^2 \frac{\hbar}{2\omega_k} (V+1)$ is the square of the dipole derivative for $V \rightarrow V+1$ of the k th vibrational mode. For the ν_3 band of CH_3F , it is measured to be 0.2756 Debye.

Appendix H

More on the numerical details of the Stokes equation

As discussed in the main text, the governing equations for the capillary breakup in a concentric two-phase fluid system are:

$$-\nabla p + \nabla \cdot [\mu(\mathbf{r}) (\nabla \mathbf{v} + \nabla \mathbf{v}^T)] = \gamma \delta(\phi(\mathbf{r})) \kappa(\phi(\mathbf{r})) \frac{\nabla \phi(\mathbf{r})}{|\nabla \phi(\mathbf{r})|} \quad (\text{H.1})$$

$$\nabla \cdot \mathbf{v} = 0 \quad (\text{H.2})$$

$$\frac{\partial \phi}{\partial t} + \mathbf{v} \cdot \nabla \phi = 0 \quad (\text{H.3})$$

with frequent re-normalization process:

$$\frac{\partial \phi}{\partial t} + \text{sign}(\phi)(|\nabla \phi| - 1) = 0. \quad (\text{H.4})$$

Since there is an azimuthal symmetry in the capillary breakup problem, we can derive terms in cylindrical coordinate (r, z) . In particular, explicit form of the lefthand side of (H.1) assuming $\mathbf{v} = u\hat{e}_r + w\hat{e}_z$ is

$$\begin{aligned} -\nabla p + \nabla \cdot [\mu (\nabla \mathbf{v} + \nabla \mathbf{v}^T)] &= \left\{ -\frac{\partial p}{\partial r} + \frac{2}{r} \frac{\partial}{\partial r} \left(\mu r \frac{\partial u}{\partial r} \right) - 2\mu \frac{u}{r^2} + \frac{\partial}{\partial z} \left[\mu \left(\frac{\partial w}{\partial r} + \frac{\partial u}{\partial z} \right) \right] \right\} \hat{e}_r \\ &+ \left\{ -\frac{\partial p}{\partial z} + \frac{1}{r} \frac{\partial}{\partial r} \left[\mu r \left(\frac{\partial u}{\partial z} + \frac{\partial w}{\partial r} \right) \right] + \frac{\partial}{\partial z} \left(2\mu \frac{\partial w}{\partial z} \right) \right\} \hat{e}_z. \end{aligned}$$

The continuity equation (H.2) is

$$\nabla \cdot \mathbf{v} = \frac{1}{r} \frac{\partial}{\partial r}(ru) + \frac{\partial w}{\partial z} = 0. \quad (\text{H.5})$$

The unit normal vector equals

$$\mathbf{n} = \frac{\nabla \phi}{|\nabla \phi|} = \frac{\phi_r}{\sqrt{\phi_r^2 + \phi_z^2}} \hat{e}_r + \frac{\phi_z}{\sqrt{\phi_r^2 + \phi_z^2}} \hat{e}_z, \quad (\text{H.6})$$

where $\phi_r = \partial\phi/\partial r$ and $\phi_z = \partial\phi/\partial z$. And the curvature is in the form of

$$\kappa(\phi) = \nabla \cdot \mathbf{n} = \left(\hat{e}_r \frac{\partial}{\partial r} + \hat{e}_\theta \frac{1}{r} \frac{\partial}{\partial \theta} + \hat{e}_z \frac{\partial}{\partial z} \right) \cdot \left(\frac{\phi_r}{\sqrt{\phi_r^2 + \phi_z^2}} \hat{e}_r + \frac{\phi_z}{\sqrt{\phi_r^2 + \phi_z^2}} \hat{e}_z \right) \quad (\text{H.7})$$

$$= \frac{\phi_{rr}\phi_z^2 - 2\phi_r\phi_z\phi_{rz} + \phi_{zz}\phi_r^2}{(\phi_r^2 + \phi_z^2)^{3/2}} + \frac{1}{r} \frac{\phi_r}{\sqrt{\phi_r^2 + \phi_z^2}}. \quad (\text{H.8})$$

For the Dirac delta function, it's approximated for the sake of numerical representation by

$$\delta(\phi) = \lim_{\epsilon \rightarrow 0^+} g(\epsilon, \phi) \quad (\text{H.9})$$

where

$$g(\epsilon, \phi) = \begin{cases} 0, & \text{for } \phi \leq -\epsilon, \\ [1 + \cos(\frac{\pi\phi}{\epsilon})] / 2\epsilon & \text{for } -\epsilon < \phi < \epsilon, \\ 0, & \text{for } \phi \geq \epsilon, \end{cases} \quad (\text{H.10})$$

In our implementation, $\epsilon = 3\Delta r$ where Δr is the grid spacing in the r direction.

The spacial discretization is performed on a staggered grid where the pressure p is in the cell corner, the r -direction velocity u placed on the horizontal cell interfaces, and the z -direction w placed on the vertical cell interfaces as shown in Fig. H-1.

Using finite difference scheme, the discretization form for different terms in the

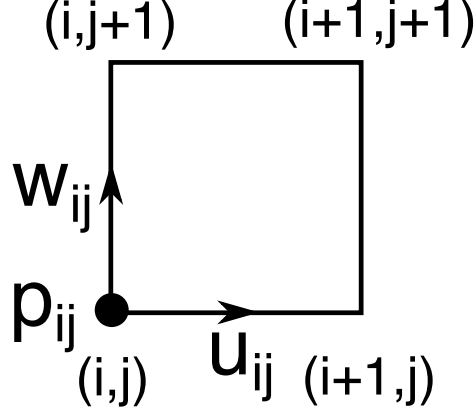


Figure H-1: Discretization grid of pressure p , velocities in r direction u , and in z direction w .

Stokes equation at grid site $(i + 1/2, j)$ with \hat{e}_r components is

$$\begin{aligned}
-\frac{\partial p}{\partial r} &:= -\frac{p_{i+1,j} - p_{i,j}}{\Delta r} \\
\frac{2}{r} \frac{\partial}{\partial r} \left(\mu r \frac{\partial u}{\partial r} \right) &:= \frac{1}{(i + 1/2)\Delta r} \frac{1}{\Delta r} \left[2(i + 1)\mu_{i+1,j}\Delta r \frac{u_{i+1,j} - u_{i,j}}{\Delta r} - 2i\mu_{i,j}\Delta r \frac{u_{i,j} - u_{i-1,j}}{\Delta r} \right], \\
-2\mu \frac{u}{r^2} &:= -2\mu_{i+1/2,j} \frac{u_{i,j}}{\left[(i + \frac{1}{2}) \Delta r \right]^2}, \\
\frac{\partial}{\partial z} \left(\mu \frac{\partial w}{\partial r} \right) &:= \frac{1}{\Delta z} \left(\bar{\mu}_{i,j} \frac{w_{i+1,j} - w_{i,j}}{\Delta r} - \bar{\mu}_{i,j-1} \frac{w_{i+1,j-1} - w_{i,j-1}}{\Delta r} \right), \\
\frac{\partial}{\partial z} \left(\mu \frac{\partial u}{\partial z} \right) &:= \frac{1}{\Delta z} \left(\bar{\mu}_{i,j} \frac{u_{i,j+1} - u_{i,j}}{\Delta z} - \bar{\mu}_{i,j-1} \frac{u_{i,j} - u_{i,j-1}}{\Delta z} \right)
\end{aligned}$$

where $\mu_{i+1/2,j} = (\mu_{i+1,j} + \mu_{i,j})/2$ and $\bar{\mu}_{i,j} = \mu_{i+1/2,j+1/2} = (\mu_{i,j} + \mu_{i,j+1} + \mu_{i+1,j} + \mu_{i+1,j+1})/4$.

Similarly, discretization forms for \hat{e}_z components are expressed at site $(i, j + 1/2)$,

$$\begin{aligned}
-\frac{\partial p}{\partial z} &:= -\frac{p_{i,j+1} - p_{i,j}}{\Delta z}, \\
\frac{1}{r} \frac{\partial}{\partial r} \left(\mu r \frac{\partial u}{\partial z} \right) &:= \frac{1}{i\Delta r} \frac{1}{\Delta r} \left[\bar{\mu}_{i,j} \left(i + \frac{1}{2} \right) \Delta r \frac{u_{i,j+1} - u_{i,j}}{\Delta z} - \bar{\mu}_{i-1,j} \left(i - \frac{1}{2} \right) \Delta r \frac{u_{i-1,j+1} - u_{i-1,j}}{\Delta z} \right], \\
\frac{1}{r} \frac{\partial}{\partial r} \left(\mu r \frac{\partial w}{\partial r} \right) &:= \frac{1}{i\Delta r} \frac{1}{\Delta r} \left[\bar{\mu}_{i,j} \left(i + \frac{1}{2} \right) \Delta r \frac{w_{i+1,j} - w_{i,j}}{\Delta r} - \bar{\mu}_{i-1,j} \left(i - \frac{1}{2} \right) \Delta r \frac{w_{i,j} - w_{i-1,j}}{\Delta r} \right] \\
\frac{\partial}{\partial z} \left(2\mu \frac{\partial w}{\partial z} \right) &:= \frac{1}{\Delta z} \left(2\mu_{i,j+1} \frac{w_{i,j+1} - w_{i,j}}{\Delta z} - 2\mu_{i,j} \frac{w_{i,j} - w_{i,j-1}}{\Delta z} \right)
\end{aligned}$$

The continuity equation is discretized at site (i, j) :

$$\begin{aligned}\frac{\partial w}{\partial z} &:= \frac{w_{i,j} - w_{i,j-1}}{\Delta z}, \\ \frac{1}{r} \frac{\partial}{\partial r}(ru) &:= \frac{1}{i\Delta r} \frac{1}{\Delta r} \left[\left(i + \frac{1}{2}\right) \Delta r u_{i,j} - \left(i - \frac{1}{2}\right) \Delta r u_{i-1,j} \right].\end{aligned}$$

Notice that in \hat{e}_z component and the continuity equation, terms of $1/i\Delta r$ might diverge when $i = 0$ at $r = 0$. We need special treatment for $r \rightarrow 0$. Say

$$q(r, z) = \mu \frac{\partial u}{\partial z}.$$

There is no extra source at $r = 0$, so $u(0, z) = 0$, and $q(0, z) = 0$. Then we can express $q(r, z)$ by Taylor expansion

$$q(r, z) = r \frac{\partial q(r, z)}{\partial r} + r^2 \frac{\partial^2 q(r, z)}{\partial r^2} + O(r^3) \quad (\text{H.11})$$

so that

$$\frac{1}{r} \frac{\partial}{\partial r} \left(\mu r \frac{\partial u}{\partial r} \right) \Big|_{r \rightarrow 0} = \frac{1}{r} \frac{\partial}{\partial r} (rq(r, z)) \Big|_{r \rightarrow 0} = 2 \frac{\partial}{\partial r} \left(\mu \frac{\partial u}{\partial z} \right)$$

Similarly, we can get

$$\frac{1}{r} \frac{\partial}{\partial r} \left(\mu r \frac{\partial w}{\partial r} \right) \Big|_{r \rightarrow 0} = 2 \frac{\partial}{\partial r} \left(\mu \frac{\partial w}{\partial r} \right)$$

since $\partial w / \partial r|_{r \rightarrow 0} \rightarrow 0$. And

$$\frac{1}{r} \frac{\partial}{\partial r} (ru) \Big|_{r \rightarrow 0} = 2 \frac{\partial u}{\partial r}$$

For the time evolution in (H.3) and (H.4), we use a third order TVD Runge-Kutta method and the HJ WENO method for spatial discretization, following the standard method in Ref. [62].

Mirror boundary condition is implemented at $r = 0$. For the other 3 boundaries, we also adopt mirror boundary condition without affecting the capillary instability. As long as the computational boundary in the r direction is far away from the interface

between the two fluids, the boundary condition doesn't affect the capillary instability. In the z direction, there is a large thermal gradient as well as large viscosity gradient in the z direction, so the mirror boundary condition works fine in the low temperature end since the interface movement is very slow. At the high-temperature boundary, the fluid column has usually broken into several spheres already, so the mirror boundary condition also doesn't affect the breakup process that is typically far away from the cell end.

Bibliography

- [1] Tadao Nagatsuma, Guillaume Ducournau, and Cyril C Renaud. Advances in terahertz communications accelerated by photonics. *Nature Photonics*, 10(6):371, 2016.
- [2] Roger A Lewis. A review of terahertz sources. *Journal of Physics D: Applied Physics*, 47(37):374001, 2014.
- [3] Alain Maestrini, John S Ward, John J Gill, Choonsup Lee, Bertrand Thomas, Robert H Lin, Goutam Chattopadhyay, and Imran Mehdi. A frequency-multiplied source with more than 1 mw of power across the 840–900-ghz band. *IEEE Transactions on Microwave Theory and Techniques*, 58(7):1925–1932, 2010.
- [4] John H Booske, Richard J Dobbs, Colin D Joye, Carol L Kory, George R Neil, Gun-Sik Park, Jaehun Park, and Richard J Temkin. Vacuum electronic high power terahertz sources. *IEEE Transactions on Terahertz Science and Technology*, 1(1):54–75, 2011.
- [5] YC Shen, PC Upadhyaya, EH Linfield, HE Beere, and AG Davies. Ultrabroadband terahertz radiation from low-temperature-grown gaas photoconductive emitters. *Applied Physics Letters*, 83(15):3117–3119, 2003.
- [6] KA McIntosh, ER Brown, KB Nichols, OB McMahon, WF DiNatale, and TM Lyszczarz. Terahertz photomixing with diode lasers in low-temperature-grown gaas. *Applied Physics Letters*, 67(26):3844–3846, 1995.
- [7] Ian B. Burgess, Yinan Zhang, Murray W. McCutcheon, Alejandro W. Rodriguez, Jorge Bravo-Abad, Steven G. Johnson, and Marko Lončar. Design of an efficient terahertz source using triply resonant nonlinear photonic crystal cavities. *Optics Express*, 17:20099–20108, 2009.
- [8] Carter M. Armstrong. <https://spectrum.ieee.org/aerospace/military/the-truth-about-terahertz>, 2012.
- [9] T. Y. Chang and T. J. Bridges. Laser action at 452, 496, and 541 μm in optically pumped CH_3F . *Optics Communications*, 1(9):423–426, 1970.

- [10] D. T. Hodges, J. R. Tucker, and T. S. Hartwick. Basic physical mechanisms determining performance of the CH₃F laser. *Infrared Physics*, 16(1-2):175–182, 1976.
- [11] Song-Liang Chua, Christine A. Caccamise, Dane J. Phillips, John D. Joannopoulos, Marin Soljačić, Henry O. Everitt, and Jorge Bravo-Abad. Spatio-temporal theory of lasing action in optically-pumped rotationally excited molecular gases. *Optics Express*, 19(8):7513–7529, 2011.
- [12] J. Henningsen and H. Jensen. The optically pumped far-infrared laser: Rate equations and diagnostic experiments. *IEEE Journal of Quantum Electronics*, 11(6):248–252, 1975.
- [13] D. Dangoisse, P. Glorieux, and J. Wascot. Diffusion and vibrational bottleneck in optically pumped submillimetre lasers. *International Journal of Infrared and Millimeter Waves*, 2(2):215–229, 1981.
- [14] W. Matteson and F. De Lucia. Millimeter wave spectroscopic studies of collision-induced energy transfer processes in the ¹³CH₃F laser. *IEEE Journal of Quantum Electronics*, 19(8):1284–1293, 1983.
- [15] Mary S. Tobin. A review of optically pumped NMMW lasers. *Proc. IEEE*, 73(1):61–85, 1985.
- [16] Henry O. Everitt, David D. Skatrud, and Frank C. De Lucia. Dynamics and tunability of a small optically pumped cw far-infrared laser. *Applied Physics Letters*, 49(16):995–997, 1986.
- [17] Rodney I McCormick, Frank C. De Lucia, and David D. Skatrud. A time-resolved study of rotational and vibrational excitation and relaxation in the ¹³CH₃F optically pumped far-infrared laser. *IEEE Journal of Quantum Electronics*, 23(12):2060–2068, 1987.
- [18] Rodney I. McCormick, Henry O. Everitt, Frank C. De Lucia, and David D. Skatrud. Collisional energy transfer in optically pumped far-infrared lasers. *IEEE Journal of Quantum Electronics*, 23(12):2069–2077, 1987.
- [19] Henry O. Everitt and Frank C. De Lucia. A time-resolved study of rotational energy transfer into A and E symmetry species of ¹³CH₃F. *Journal of Chemical Physics*, 90(7):3520–3527, 1989.
- [20] Nigel G. Douglas. *Millimetre and Submillimetre Wavelength Lasers: A Handbook of CW Measurements*, volume 61. Springer, 1989.
- [21] Henry O. Everitt and Frank C. De Lucia. Rotational energy transfer in CH₃F: The $\Delta J = n$, $\Delta K = 0$ processes. *The Journal of Chemical Physics*, 92(11):6480–6491, 1990.

- [22] A. Johnson and D. Auston. Microwave switching by picosecond photoconductivity. *IEEE Journal of Quantum Electronics*, 11(6):283–287, 1975.
- [23] Martin Van Exter and D. Grischkowsky. Optical and electronic properties of doped silicon from 0.1 to 2 THz. *Applied Physics Letters*, 56(17):1694–1696, 1990.
- [24] A. A. Andronov, V. A. Flyagin, A. V. Gaponov, A. L. Gol'denberg, M. I. Petelin, V. G. Usov, and V. K. Yulpatov. The gyrotron: High-power source of millimetre and submillimetre waves. *Infrared Physics*, 18(5-6):385–393, 1978.
- [25] Jerome Faist, Federico Capasso, Deborah L. Sivco, Carlo Sirtori, Albert L. Hutchinson, and Alfred Y. Cho. Quantum cascade laser. *Science*, 264(5158):553–555, 1994.
- [26] Jerome Faist, Federico Capasso, Carlo Sirtori, Deborah L Sivco, James N Bailargeon, Albert L Hutchinson, Sung-Nee G Chu, and Alfred Y Cho. High power mid-infrared (λ 5 μm) quantum cascade lasers operating above room temperature. *Applied Physics Letters*, 68(26):3680–3682, 1996.
- [27] Yu Yao, Anthony J Hoffman, and Claire F Gmachl. Mid-infrared quantum cascade lasers. *Nature Photonics*, 6(7):432, 2012.
- [28] Henry Olin Everitt III. *Collisional Energy Transfer in Methyl Halides*. PhD thesis, Duke University, 1990.
- [29] Henry O. Everitt and Frank C. De Lucia. Rotational energy transfer in small polyatomic molecules. *Advances in Atomic, Molecular, and Optical Physics*, 35:331, 1995.
- [30] Fan Wang, Jeongwon Lee, Dane J. Phillips, Samuel G. Holliday, Song-Liang Chua, Jorge Bravo-Abad, John D. Joannopoulos, Marin Soljačić, Steven G. Johnson, and Henry O. Everitt. A high-efficiency regime for gas-phase terahertz lasers. *Proceedings of the National Academy of Sciences, USA*, 115(26):6614–6619, 2018.
- [31] Bahaa E. A. Saleh and Malvin Carl Teich. *Fundamentals of Photonics*, volume 22. Wiley, 1991.
- [32] R. Panock and R. Temkin. Interaction of two laser fields with a three-level molecular system. *IEEE Journal of Quantum Electronics*, 13(6):425–434, 1977.
- [33] H. Scott Fogler. *Elements of Chemical Reaction Engineering*. Prentice-Hall International London, 1999.
- [34] Homer F. Walker and Peng Ni. Anderson acceleration for fixed-point iterations. *SIAM Journal on Numerical Analysis*, 49:1715–1735, 2011.
- [35] Rajeev Bansal. *Fundamentals of Engineering Electromagnetics*. CRC press, 2006.

- [36] Edinburgh Instruments Ltd. <https://www.edinst.com/products/>, 2018.
- [37] Richard M Williams, James F Kelly, John S Hartman, Steven W Sharpe, Matthew S Taubman, John L Hall, Federico Capasso, Claire Gmachl, Deborah L Sivco, James N Baillargeon, et al. Kiloherz linewidth from frequency-stabilized mid-infrared quantum cascade lasers. *Optics Letters*, 24(24):1844–1846, 1999.
- [38] Richard L. Crownover, Henry O. Everitt, Frank C. De Lucia, and David D. Skatrud. Frequency stability and reproducibility of optically pumped far-infrared lasers. *Applied Physics Letters*, 57(27):2882–2884, 1990.
- [39] Patrick R Amestoy, Iain S Duff, and J-Y L’exceller. Multifrontal parallel distributed symmetric and unsymmetric solvers. *Computer methods in applied mechanics and engineering*, 184(2-4):501–520, 2000.
- [40] Kevin Knabe, Paul A Williams, Fabrizio R Giorgetta, Chris M Armacost, Sam Crivello, Michael B Radunsky, and Nathan R Newbury. Frequency characterization of a swept-and fixed-wavelength external-cavity quantum cascade laser by use of a frequency comb. *Optics express*, 20(11):12432–12442, 2012.
- [41] A Pagies, G Ducournau, and J-F Lampin. Low-threshold terahertz molecular laser optically pumped by a quantum cascade laser. *APL Photonics*, 1(3):031302, 2016.
- [42] Antoine Pagies, Guillaume Ducournau, and Jean-François Lampin. Progress in continuous wave thz molecular laser optically pumped by a quantum cascade laser. In *2017 42nd International Conference on Infrared, Millimeter, and Terahertz Waves (IRMMW-THz)*, pages 1–2. IEEE, 2017.
- [43] C.H. Townes and A. L. Schawlow. *Microwave Spectroscopy*. Dover Publications, Inc., 1995.
- [44] W. Gordy and R. L. Cook. *Microwave Molecular Spectroscopy*. Wiley-Interscience, New York, 1984.
- [45] I.E. Gordon, L.S. Rothman, C. Hill, R.V. Kochanov, Y. Tan, P.F. Bernath, M. Birk, V. Boudon, A. Campargue, K.V. Chance, B.J. Drouin, J.-M. Flaud, R.R. Gamache, J.T. Hodges, D. Jacquemart, V.I. Perevalov, A. Perrin, K.P. Shine, M.-A.H. Smith, J. Tennyson, G.C. Toon, H. Tran, V.G. Tyuterev, A. Barbe, A.G. Császár, V.M. Devi, T. Furtenbacher, J.J. Harrison, J.-M. Hartmann, A. Jolly, T.J. Johnson, T. Karman, I. Kleiner, A.A. Kyuberis, J. Loos, O.M. Lyulin, S.T. Massie, S.N. Mikhailenko, N. Moazzen-Ahmadi, H.S.P. Müller, O.V. Naumenko, A.V. Nikitin, O.L. Polyansky, M. Rey, M. Rotger, S.W. Sharpe, K. Sung, E. Starikova, S.A. Tashkun, J. Vander Auwera, G. Wagner, J. Wilzewski, P. Wcisło, S. Yu, and E.J. Zak. The HITRAN2016 molecular spectroscopic database. *Journal of Quantitative Spectroscopy and Radiative Transfer*, 203:3 – 69, 2017. HITRAN2016 Special Issue.

- [46] *JPL Molecular Spectroscopy Database*, 2017.
- [47] *Splatalogue Database for Astronomical Spectroscopy*, 2007.
- [48] JM Manley and HE Rowe. Some general properties of nonlinear elements-part i. general energy relations. *Proceedings of the IRE*, 44(7):904–913, 1956.
- [49] QY Lu, Y Bai, N Bandyopadhyay, S Slivken, and M Razeghi. 2.4 w room temperature continuous wave operation of distributed feedback quantum cascade lasers. *Applied Physics Letters*, 98(18):181106, 2011.
- [50] Paul Chevalier, Marco Piccardo, Sajant Anand, Enrique A Mejia, Yongrui Wang, Tobias S Mansuripur, Feng Xie, Kevin Lascola, Alexey Belyanin, and Federico Capasso. Watt-level widely tunable single-mode emission by injection-locking of a multimode fabry-perot quantum cascade laser. *Applied Physics Letters*, 112(6):061109, 2018.
- [51] Richard G Brewer, MJ Kelly, and A Javan. Precision infrared stark spectra of n 14 h 2 d using lamb dip. *Physical Review Letters*, 23(11):559, 1969.
- [52] Nanfang Yu and Federico Capasso. Flat optics with designer metasurfaces. *Nature Materials*, 13(2):139, 2014.
- [53] Donald A. McQuarrie and John D. Simon. *Physical chemistry : a molecular approach*. University Science Books, Sausalito, Calif., 1997.
- [54] Arthur L Schawlow and Charles H Townes. Infrared and optical masers. *Physical Review*, 112(6):1940, 1958.
- [55] Joseph Plateau. *Statique expérimentale et théorique des liquides soumis aux seules forces moléculaires*, volume 2. Gauthier-Villars, 1873.
- [56] Lord Rayleigh. On the capillary phenomena of jets. *Proc. R. Soc. London*, 29(196-199):71–97, 1879.
- [57] Lord Rayleigh. Xvi. on the instability of a cylinder of viscous liquid under capillary force. *The London, Edinburgh, and Dublin Philosophical Magazine and Journal of Science*, 34(207):145–154, 1892.
- [58] S Tomotika. On the instability of a cylindrical thread of a viscous liquid surrounded by another viscous fluid. *Proceedings of the Royal Society of London. Series A-Mathematical and Physical Sciences*, 150(870):322–337, 1935.
- [59] Joshua J. Kaufman, Guangming Tao, Soroush Shabahang, Esmaeil-Hooman Banaei, Daosheng S. Deng, Xiangdong Liang, Steven G. Johnson, Yoel Fink, and Ayman F. Abouraddy. Structured spheres generated by an in-fibre fluid instability. *Nature*, 487:463–467, July 2012.

- [60] Xiangdong Liang, DS Deng, J-C Nave, and Steven G Johnson. Linear stability analysis of capillary instabilities for concentric cylindrical shells. *Journal of Fluid Mechanics*, 683:235–262, 2011.
- [61] Alexander Gumennik, Lei Wei, Guillaume Lestoquoy, Alexander M Stolyarov, Xiaoting Jia, Paul H Rekemeyer, Matthew J Smith, Xiangdong Liang, Benjamin J-B Grena, Steven G Johnson, et al. Silicon-in-silica spheres via axial thermal gradient in-fibre capillary instabilities. *Nature communications*, 4:2216, 2013.
- [62] Mark Sussman, Peter Smereka, and Stanley Osher. A level set approach for computing solutions to incompressible two-phase flow. *Journal of Computational physics*, 114(1):146–159, 1994.
- [63] Per-Olof Persson. The level set method lecture notes, mit 16.920 j/2.097 j/6.339 j numerical methods for partial differential equations. 2005.
- [64] Thomas R Powers and Raymond E Goldstein. Pearling and pinching: propagation of rayleigh instabilities. *Physical review letters*, 78(13):2555, 1997.
- [65] H. A. Bethe. Theory of diffraction by small holes. *Physical Review*, 66(7-8):163, 1944.